Studies on development of MgB_2 superconductor with improved in-field critical current density

Thesis submitted to
Cochin University of Science and Technology (CUSAT)
in partial fulfillment of the requirements for the award of the degree
of
Doctor of Philosophy
in **Physics** under the **Faculty of Science**

by

VINOD. K

under the supervision of

Dr. U. Syamaprasad

National Institute for Interdisciplinary Science and Technology
(Council of Scientific and Industrial Research)
Thiruvananthapuram-695019

January 2010

Studies on development of MgB_2 superconductor with improved in-field critical current density

Dedicated to

my father, mother and brother

DECLARATION

I, Vinod. K., hereby declare that, this thesis entitled "**Studies on development of MgB_2 superconductor with improved in-field critical current density**" is a bonafide record of the research work done by me under the supervision and guidance of Dr. U. Syamaprasad, Scientist, National Institute for Interdisciplinary Science and Technology (CSIR), Thiruvananthapuram and that no part of this thesis has been presented earlier for any degree, diploma, associateship, or any other title or recognition of any other University.

Vinod. K

Thiruvananthapuram
January 17, 2010

NATIONAL INSTITUTE FOR INTERDISCIPLINARY SCIENCE & TECHNOLOGY

An ISO 9001 Certified Laboratory

(Formerly – Regional Research Laboratory)

Concil of Scientic & Industrial Research

Industrial Estate P.O., Trivandrum –695 019, INDIA

Tel :91–471–2515 373/2515 233; Fax : +91–471–2491 712

Email : syam@csrrltrd.re.nic.in; syamcsir@gmail.com.

Website: www.niist.res.in

Dr. U. SYAMAPRASAD

SCIENTIST G, SENIOR DEPUTY DIRECTOR AND HEAD

APPLIED SUPERCONDUCTIVITY & CERAMICS SECTION

January 17, 2010

CERTIFICATE

This is to certify that the thesis entitled "**Studies on development of MgB_2 superconductor with improved in-field critical current density**" is an authentic record on the research work carried out by Mr. Vinod. K., under my supervision in partial fulfillment of the requirement for the degree of **Doctor of Philosophy** of the Cochin University of Science and Technology and further that no part of this thesis has been presented for any other degree.

U. Syamaprasad

Acknowledgments

During my last 5 years of research work at NIIST, for the Ph.D. degree, many people contributed to my research and life. I wish to express my sincere gratitude and appreciation to all those, whose contribution I value.

I am truly grateful to my supervisor, **Dr. U. Syamaprasad** for the guidance and encouragement. I sincerely thank him, for the support and opportunities he provided to me.

I sincerely appreciate the help and friendship of the entire Superconducting materials research group during my studies. In particular, I thank: **Mr. P Guruswamy**, for the technical support and encouragement; my colleagues, **S. Rahul, Neson Varghese, K. M. Devadas, Syju Thomas, P. M. Sarun, S. Vinu, R. Shabna, P. M. Aswathy, J. B. Anooja, K. T. Jakson, A. Sivaprakash, S. Santhosh Kumar and G. R. Anuraghi** for the help, friendship and fruitful scientific discussions. I specially thank **Dr. R. P. Aloysius** for the useful scientific discussions, support and help. I thank **Dr. A. Biju, R. G. Abhilash kumar and S. Thennavarajan** for the support and help. I also thank **B. Premlal** for sending me the journal articles I requested. I thank **M. Suresh, T. Antony Prabhu, A. Nazeer, A. Vasudevan, S. S. Soorya, C. Navya Paul, V. G. Prabitha and Rosamma Sebastian** for their help and friendship. Special thanks are due to **Mr. M. R. Chandran, Dr. Prabhakar Rao, Mr. Robert Philip, Mr. Narendran** and **Dr. V. S. Prasad** of *NIIST*, Trivandrum for performing the SEM, TEM and EDS of the samples.

I sincerely thank **Dr. A. Sundaresan**, *Jawaharlal Nehru Centre for Advanced Scientific Research (JNCASR), Bangalore*, **Dr. S. B. Roy**, *Raja Ramanna Centre for Advanced Technology (RRCAT), Indore* and **Dr. S. Pradhan**, *Institute for Plasma Research (IPR), Gandhinagar*, for experimental support, fruitful scientific discussions and collaboration.

I also thank **Prof. Ashok Rao**, *Department of Physics, Manipal Institute of Technology, Manipal*, and **Prof. Y. K. Kuo**, *Department of Physics, National Dong Hwa University, Hualien, Taiwan*, for experimental support.

I thank **Dr. Suresh Das**, *Director, NIIST*, **Dr. B. C. Pai** and **Prof. T. K. Chandrasekhar**, *former Directors of NIIST*, for providing all the facilities

to carry out this work and for their encouragement during this work. I thank **Dr. K. G. K. Warrier**, *Head, Materials Division, NIIST* for the support and encouragement. I also thank **Prof. K. P. Vijayakumar**, *Department of Physics, Cochin University of Science and Technology, Kochi* for useful discussions at various stages of the work.

I sincerely acknowledge the *Council of Scientific and Industrial Research (CSIR)* for providing the research fellowship and thus an opportunity to do the present work.

Vinod. K

PREFACE

In the superconducting state, a superconductor has zero electrical resistance and hence can transport large electrical currents without any resistive loss. The unique property of dissipation free current transport has strong prospective on practical applications. Today superconducting materials have extensive uses in energy production, storage and distribution, in electronics, and most importantly in high field magnets. Superconducting magnets have major use in MRI instruments in medical field, for high field R & D instruments like NMR, for energy storage in SMES, for confinement of plasma in fusion reactors and for the magnetic levitation systems in transportation. The wide spread use of superconductors is mainly limited by cost associated with maintaining very low temperatures.

The most commonly used superconducting materials are two low temperature superconductors (LTS), NbTi having a T_C of 9 K and Nb_3Sn having a T_C of 18 K. NbTi has an H_{C2} of 10-11 T at 4.2 K and is relatively easy to fabricate in wires or tapes and occupies most of the low field magnets in MRI instruments. Nb_3Sn has H_{C2} value of more than 20 T at 4.2 K and is used in high field magnets. Both NbTi and Nb_3Sn based magnets use liquid helium (LHe) as the coolant, which is expensive. The discovery of high temperature superconductors (HTS), superconducting above 77 K and having H_{C2} more than 100 T, made excitement with the possibility of operating superconducting devices at a reduced cost. These can be cooled to the superconducting state using liquid nitrogen (LN_2), which is much cheaper than liquid helium. But the HTS conductors faced many technical problems in making wires and coils. These materials are granular and highly anisotropic and the critical current density falls sharply in applied fields.

The discovery of superconductivity in MgB_2, a binary intermetallic, in 2001 by Jun Akimitsu's group in Japan generated a boom in applied superconductivity research. MgB_2 has a higher T_C of 39 K as compared to the conventional LTS and is free from most of the limitations of HTS. MgB_2 conductors with large transport current densities of around 10^5 A/cm^2 at 4.2-20 K have been demonstrated in a few labs. MgB_2 based systems can be operated in the 20-30 K temperature range with cryocoolers (eliminates the need for expensive LHe), where conventional LTS cannot be used. Compared to the HTS, preparation of MgB_2 into multifilamentary conductors is relatively easy and the raw materials are inexpensive.

Currently the major challenges involved in the development of MgB_2 conductors for practical applications are the preparation of good quality MgB_2 in bulk, wire/tape and coil, and improvement of field performance. The oxidation and vapor loss of Mg are the main hurdles for the preparation of good quality MgB_2. The wide difference in the melting point between Mg (650 °C) and B (2080 °C) limits the solid - solid and liquid - liquid reaction, and the MgB_2 formed by liquid - solid reaction is highly porous. The sinterability of MgB_2 grains is poor also. Mg reacts with most of the common sheath metals and the mechanical workability of chemically compatible metals is low. MgB_2 has high critical current density at self-field, but the critical current density falls sharply in applied fields. For technological applications the in-field critical current density must be improved considerably.

The present thesis focuses on the preparation of good quality MgB_2 in bulk, wire/tape forms and on the improvement of in-field critical current density. The results can be used for the development of MgB_2 based superconductors for practical applications.

The thesis is organized into 6 chapters. First chapter gives a brief introduction to the phenomenon of superconductivity, superconducting materials, applications and the features of MgB_2 superconductor. A review of the present international status on the development of MgB_2 is also given in the chapter. The second chapter discusses the various material characterization techniques used for the study. Third, fourth and fifth chapters describes the experimental results, main findings and discussion of the research carried out. Third chapter deals with the preparation and characterization of bulk MgB_2 superconductor. Fourth chapter deals with the preparation and characterization MgB_2 superconductor in mono and multifilamentary wire/tape form. Fifth chapter deals with the chemical addition studies carried out to improve the in-field critical current density of MgB_2 superconductor. Chapter 6 summarizes the work with main conclusions and the scope for future work.

A simple Powder-In-Sealed-Tube (PIST) method is identified for preparing good quality MgB_2 bulk superconductor. In this method, Mg and B powders were filled in seamless stainless steel tubes and heat treated in atmospheric condition after sealing the ends. The method is simple and cost effective, as the need for vacuum or inert atmosphere is eliminated for the

preparation. For the preparation of wires and tapes a systematic study on the chemical reactivity of various sheath materials such as Ag, Cu, Fe, Ni, Stainless Steel (SS) and Ta with Mg/B was conducted. Among these Fe is found to be the most suitable material for the sheath. Fe sheathed MgB_2 wires and tapes were prepared by *in situ* Powder-In-Tube (PIT) technique in mono and multi filamentary geometries. Further, a novel electrical self-heating method was introduced for the preparation of Fe sheathed MgB_2 wires and tapes. The prepared superconductor in bulk, wire and tape forms were characterized for phase purity, structural and superconducting properties, and these are at par with the best quality samples reported worldwide.

Additives of different types were introduced into the MgB_2 for improving the in-field critical current density. Burned rice husk (BRH), an inexpensive natural material is found to be one of the best additive for enhancing the in-field critical current density of MgB_2. By selecting suitable combinations of additives a significant enhancement of the critical current density by 1-2 orders of magnitude were achieved for fields > 5 T, at 5 and 15 K.

Details of patents and publications

List of patents granted/filed

Title: A process for continuous production of Magnesium Diboride based superconductors
U. Syamaprasad, R. G. Abhilash Kumar, **K. Vinod**, R. P. Aloysius, P. M. Sarun, S. Thennavarajan, P. Guruswamy

1. US patent (granted): Patent no US 7456134 B2
2. UK patent (filed): 0185NF2005/GB, filing date: 23-04-2008
3. German patent (filed): 0185NF2005/DE, filing date: 21-05-2008
4. Japan patent (filed): 0185NF2005/JP, filing date: 26-05-2008
5. Indian patent (filed): 0185NF2005/IN, filing Date: 25-11-2005

List of papers published in SCI journals

1. Highly enhanced in-field critical current density of MgB_2 superconductor by combined addition of burned rice husk and nano Ho_2O_3
K. Vinod, Neson Varghese, A. Sundaresan and U. Syamaprasad, accepted for publication in *Solid State. Sci.*
2. Effect of combined addition of nano SiC and nano Ho_2O_3 on the in-field critical current density of MgB_2 superconductor
Neson Varghese, **K. Vinod**, M. K. Chattopadhyay, S. B. Roy and U. Syamaprasad, *J. Appl. Phys.* 107 (2010) 013907(1-5)
3. Burned rice husk: An effective additive for enhancing the electromagnetic properties of MgB_2 superconductor
Neson Varghese, **K. Vinod**, Shipra, A. Sundaresan and U. Syamaprasad *J. Am. Ceram. Soc.* DOI: 10.1111/j.1551-2916.2009.03438.x
4. Significant enhancement of the in-field critical current density of the MgB_2 superconductor through codoping of nano-TiC with nano-SiC
K. Vinod, Neson Varghese, S. B. Roy and U. Syamaprasad, *Supercond. Sci. Technol.* 22 (2009) 055009(1-9)
5. Preparation of *in situ* MgB_2/Fe superconducting tapes with highly densified core by hot pressing of electrically self-heated PIT wires
K. Vinod, Neson Varghese, S. Rahul and U. Syamaprasad, *Materials Science and Engineering B* 164 (2009) 131-134
6. Doping effect of nano-SiC on structural and superconducting properties of MgB_2 bulks prepared by PIST method in air
Neson Varghese, **K. Vinod**, U. Syamaprasad and S.B. Roy, *J. Alloys and Compounds.* 484 (2009) 734-738
7. Enhanced superconducting properties of bulk MgB_2 prepared by *in situ* Powder-In-Sealed-Tube method
Neson Varghese, **K. Vinod**, Ashok Rao, Y.K. Kuo and U. Syamaprasad *J. Alloys and Compounds.* 470 (2009) 63-66
8. Superconductivity of MgB_2 in the BCS framework with emphasis on extrinsic effects on critical temperature
K. Vinod, Neson Varghese and U. Syamaprasad *Supercond. Sci. Technol.* 20 (2007) R31-R45. [**TOPICAL REVIEW**]

9. Prospects of MgB_2 superconductors for magnet application
K. Vinod, R. G. Abhilash Kumar and U. Syamaprasad, *Supercond. Sci. Technol.* 20 (2007) R1-R13. [**TOPICAL REVIEW**]
10. Structural and superconducting properties of bulk MgB_2 with added nano Tb_4O_7
K. Vinod, Neson Varghese, U. Syamaprasad, Shipra and A. Sundaresan *Supercond. Sci. Technol.* 21 (2008) 025003 (1-5).
11. Influence of Mg particle size on the reactivity and superconducting properties of *in situ* MgB_2
K. Vinod, Neson Varghese, R.G. Abhilash Kumar, U. Syamaprasad and S.B. Roy *J. Alloys and Compounds.* 464 (2008) 33-37
12. Reactivity of sheath materials with Mg/B in MgB_2 conductor fabrication
R. G. Abhilash Kumar, **K. Vinod**, Neson Varghese and U. Syamaprasad *Supercond. Sci. Technol.* 20 (2007) 222-227.
13. Influence of reactivity of sheath materials with Mg/B on superconducting properties of MgB_2
Neson Varghese, **K. Vinod**, R. G. Abhilash Kumar, U. Syamaprasad and A. Sundaresan, *J. Appl. Phys.* 102 (2007) 043914 (1-4).
14. Preparation of MgB_2/Fe superconductor wire by electrical self-heating
R. G. Abhilash Kumar, **K. Vinod** and U. Syamaprasad, *Appl. Phys. A: Materials Science and Processing* 88 (2007) 243-247.
15. A simple and inexpensive method for rapid synthesis of MgB_2 superconductor
R. G. Abhilash Kumar, **K. Vinod**, R. P. Aloysius and U. Syamaprasad, *Materials Letters* 60 (2006) 3328-3331
16. Highly enhanced flux pinning in Pb and rare earth codoped Bi-2212
A. Biju, **K. Vinod**, P. M. Sarun and U. Syamaprasad, *Appl. Phys. Lett.* 90 (2007) 072505 (1-3).
17. Flux pinning properties of magnesium diboride added (Bi,Pb)-2212 superconductors
K. Vinod, R. G. Abhilash Kumar, A. Biju, P. M. Sarun and U. Syamaprasad *J. Alloys and Compounds.* 439 (2007) L1-L4.
18. Improved superconducting properties by La addition in (Bi,Pb)-2212 bulk superconductor
A. Biju, **K. Vinod**, R. P. Aloysius and U. Syamaprasad *J. Alloys and Compounds.* 431 (2007) 49-55.
19. Effect of site selective doping of Sm on the superconducting and flux pinning properties of (Bi,Pb)-2212
A. Biju, **K. Vinod** and U. Syamaprasad, *Supercond. Sci. Technol.* 19 (2006) 1083-1088
20. Electrical self heating : A simple and energy efficient heat treatment method.
K. Vinod, Neson Varghese, S. Rahul and U. Syamaprasad communicated to *J. Natural. Sciences.* [**Invited paper**]

List of papers presented/published in seminars/conferences

1. Studies on development of MgB_2 superconductor with improved in-field critical current density. [**Invited paper**]
K. Vinod and U. Syamaprasad, Presented at the DST-JSPS Asia Science Seminar held at Yokohama, Japan on December 8-15, 2009.

2. Combined effect of burned rice husk and nano Ho_2O_3 on the in-field critical current density of MgB_2 superconductor.
   S. Rahul, G. R. Anuraghi, K. T. Jakson, Neson Varghese, **K. Vinod** and U. Syamaprasad, Presented at the International Conference on Advanced Functional Materials (ICAFM 2009), held at NIIST, Trivandrum on December 09-10, 2009.

3. Eeffect of combined addition of nano SiC and TiC on the structural and superconducting properties of MgB_2.
   Neson Varghese, J. B. Anooja, P. M. Aswathy, **K. Vinod**, S. B. Roy and U. Syamaprasad, Presented at the International Conference on Advanced Functional Materials (ICAFM 2009), held at NIIST, Trivandrum on December 09-10, 2009.

4. Hot pressing of electrically self-heated MgB_2/Fe PIT wires.
   K. Vinod, Neson Varghese, S. Rahul and U. Syamaprasad, Presented at the 53rd DAE Solid State Physics Symposium (DAE SSPS 2008), held at BARC on December 16-20, 2008. (Also published in the proceedings: vol 53 page 919-920)

5. Enhancement of high field critical current density in nano SiC doped MgB_2 prepared by powder-in-sealed-tube method.
   Neson Varghese, **K. Vinod**, S. B. Roy and U. Syamaprasad, Presented at the 53rd DAE Solid State Physics Symposium (DAE SSPS 2008), held at BARC on December 16-20, 2008. (Also published in the proceedings: vol 53 page 897-898)

6. Synthesis of MgB_2 superconductor by an electrical self-heating method
   K. Vinod , R. G. Abhilash Kumar , R. P. Aloysius and U. Syamaprasad, Presented at the 18th AGM, Materials Research Society of India (MRSI), held at NPL NewDelhi on February 12-14, 2007

7. Influence of heat treatment temperature and duration on the crystalline and microstructural properties of *in situ* MgB_2 superconductor
   K. Vinod, Neson Varghese, R. G. Abhilash Kumar and U. Syamaprasad, Presented at the International Conference on Advanced Materials and Composites (ICAMC), held at NIIST Thiruvananthapuram on October 24-26, 2007. (Also published in the proceedings: page 784-788)

8. Chemical compatibility of sheath materials for *in situ* MgB_2 superconductor wire/tape fabrication
   Neson Varghese, **K. Vinod**, R. G. Abhilash Kumar and U. Syamaprasad, Presented at the International Conference on Advanced Materials and Composites (ICAMC), held at NIIST Thiruvananthapuram on October 24-26, 2007. (Also published in the proceedings: page 773-778)

9. Effect of sintering temperature on the microstructure and superconducting properties of *in situ* polycrystalline MgB_2
   K.Vinod, Neson Varghese and U.Syamaprasad, Presented at the 52nd DAE Solid State Physics Symposium (DAE SSPS 2007), held at Mysore on December 27-31, 2007. (Also published in the proceedings: vol 52 page 791-792)

10. Structural and superconducting properties of MgB_2 added (Bi,Pb)-2212 superconductor
    R. G. Abhilash Kumar, **K. Vinod**, A. Biju and U. Syamaprasad, Presented at the XXVIII National Conference on Electrom Microscopy Society of India, April 19-21, 2006

Contents

List of Figures

List of Tables

List of Abbreviations

at.%	Atomic percentage
wt.%	Weight percentage
Vol.%	Volume percentage
LTS	Low Temperature Superconductor
HTS	High Temperature Superconductor
BCS	Bardeen Cooper and Schrieffer
ZFC	Zero Field Cooling
FC	Field Cooling
MRI	Magnetic Resonance Imaging
NMR	Nuclear Magnetic Resonance
FCL	Fault Current Limitter
SMES	Superconducting Magnetic Energy Storage
XRD	X-Ray Diffraction
SEM	Scanning Electron Microscopy
SEI	Secondary Electron Imaging
TEM	Transmission Electron Microscopy
EDS	Energy Dispersive X-Ray Spectrum
FWHM	Full Width at Half Maximum
RRR	Residual Resistivity Ratio
SQUID	Superconducting QUantum Interference Device
VSM	Vibrating Sample Magnetometer
PPMS	Physical Property Measurement System
PIT	Powder In Tube
PIST	Powder In Sealed Tube
RE	Rare Earth
REO	Rare Earth Oxide
BRH	Burned Rice Husk
CNT	Carbon Nano Tube
LN_2	Liquid Nitrogen
LHe	Liquid Helium
HIP	Hot Isostatic Pressing
HPS	High Pressure Sintering
DOS	Density of States
DFT	Density Functional Theory
ICDD	International Center for Diffraction Data
PDF	Powder Diffraction File
DC	Direct Current
AC	Alternating Current
PC	Personal Computer
GPIB	General Purpose Interface Board

SS	Stainless Steel
OD	Outside Diameter
ID	Inside Diameter
NIIST	National Institute for Interdisciplinary Science and Technology
SW	Mono (Single) filamentary wire
ST	Mono (Single) filamentary tape
MW	Multifilamentary wire
MT	Multifilamentary tape
JNCASR	Jawaharlal Nehru Centre for Advanced Scientific Research
RRCAT	Raja Ramanna Centre for Advanced Technology
IPR	Institute for Plasma Research

List of Symbols

a, b, c	Sample dimensions
a, *c*	Lattice parameters
d	Inter atomic spacing
h, *k*, *l*	Miller indices of crystal planes
Å	Angstrom unit
T	Temperature
I	Current
V	Voltage
M	Magnetization
H	Magnetic field
R	Resistatnce
ρ	Resistivity
χ	Magnetic Susceptibility
T_{C}	Critical temperature (Transition temperature)
T_{Conset}	Temperature corresponding to Onset of transition
T_{Coffset}	Temperature corresponding to Offset of transition
ΔT_{C}	Width of Transition (Difference between and T_{Conset} and T_{Coffset})
I_{C}	Critical Current
J_{C}	Critical Current density
J_{E}	Engineering Critical Current density
$J_{\mathrm{C}}(H)$	In-field Critical Current density
H_{C}	Critical Field
H_{C1}	Lower Critical Field
H_{C2}	Upper Critical Field
H_{irr}	Irreversibility Field
F_{P}	Flux pinning force density
F_{Pmax}	Maximum flux pinning force density
H_{peak}	Field corresponding to maximum flux pinning force density
ξ	Coherence length
λ	Penetration depth
σ	σ Bonding
π	π Bonding
$\Delta(0)$	BCS energy gap at 0 K
Δ_σ	σ band energy gap
Δ_π	π band energy gap
μ^*	Chemical potential

Chapter 1

Introduction to MgB_2 superconductor

1.1 Superconductivity

In 1908 Heike Kamerlingh Onnes, professor of experimental physics at the university of Leiden (Holland) liquified helium for the first time. He soon set about measuring the electrical resistivity of metals at low temperatures. In 1911, while measuring the electrical resistivity of mercury, he observed a sudden and massive drop in resistivity below 4.2 K. As the mercury wires were slowly cooled below 4.2 K, in just a few hundredths of a degree, the resistance dropped to immeasurably low value. i.e. practically into zero [1]. Onnes termed the electrical state mercury had entered as **superconducting** state. Thus the phenomenon of vanishing of electrical resistivity of materials below a particular low temperature has been called **superconductivity** and the materials which exhibit this property are called **superconductors**. The temperature at which the transition from normal state to superconducting state occurs is called the superconducting transition temperature or **critical temperature** T_C.

In 1933 Meissner and his student Robert Oschenfield made an important discovery about the behavior of superconductors in external magnetic fields. While investigating the superconducting transition of materials in applied magnetic fields, they found that the magnetic flux was expelled from the interior of the superconductor (for field upto a critical field H_C),

irrespective of the path used to apply the field [2]. This characteristic property of a superconductor is called the **Meissner effect**. The complete expulsion of magnetic flux shows that the superconductor is perfectly diamagnetic in the superconducting state.

The normal and superconducting state of a material is determined by the temperature, external magnetic field and the current density flowing through the material. Thus for the occurrence of superconductivity in a material the temperature must be below the **critical temperature (T_C)**, the external magnetic field must be below the **critical field (H_C)** and the current density flowing through the material must be below the **critical current density (J_C)**. The three parameters T_C (H,J), H_C (T,J) and J_C (H,T) define a critical surface as illustrated in figure 1.1, beneath the surface the material is in superconducting state and above the surface the material is in normal state.

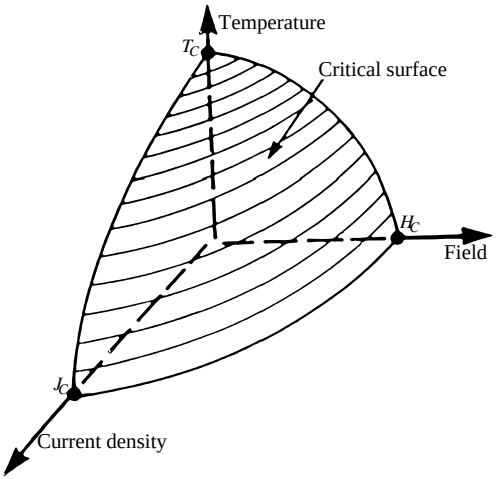

Figure 1.1: Illustration of superconducting critical surface.

The usefulness of a superconductor for technological applications depends on its ability to carry sufficient high current density without resistive losses at the working field (H) and temperature (T). There are two limits to the J_C in practical superconductors: the intrinsic J_C is limited by H_{C2}, H_{irr}

and flux pinning, and the extrinsic J_C limited by factors like grain connectivity, grain orientation (anisotropy). One of the aims of the present work is to improve the J_C of MgB_2 superconductor at higher fields by selective chemical addition.

1.2 Electromagnetic properties of superconductors

Superconductors have peculiar electromagnetic properties that differ very much from that of normal conducting materials. In the superconducting state a superconductor has zero electrical resistance and can carry DC transport currents without any dissipation or energy loss, upto the critical current (I_C). The behavior of a superconductor in an AC field or AC transport current is more complex and is not included in the discussion as it is outside the scope of the present work. In the case of AC transport currents, the flow is superconducting at lower frequencies, the current experiences an inductive reactance at higher frequencies. At optical frequencies ($> 10^{14}$ Hz), the AC current flow is mostly normal.

A superconductor behaves differently from that of a normal conductor in an external magnetic field. Based on their behavior in an external field, superconductors are classified into two categories – Type I and Type II superconductors.

In the superconducting state a superconductor shows Meissner effect and expels an external magnetic field from its interior, upto a **thermodynamic critical field H_C**. The expulsion of field is independent of the experimental history ie. whether the field is applied after cooling below T_C (Zero Filed Cooling – ZFC) or the superconductor is cooled below the T_C in the presence of a field (Field Cooling – FC). While the description of the field being excluded from the volume is reasonable, in reality the external field penetrates to a small depth, to the so called London penetration length $\lambda = \frac{m_e}{\sqrt{\mu_0 n_s e^2}}$, where e and m_e are the charge and mass of electron and n_s is the density of superconducting electrons. Inside the superconductor, the density of superconducting electrons cannot change abruptly and changes gradually only over a distance called the coherence length ξ. That is there is no sharp boundary between a normal conducting and superconducting regions and the transition from a superconducting to normal conducting

region takes place over a length of ξ. The coherence length has a constant value at the core of a superconducting region and decreases gradually to zero at the interface of normal region. The ratio of penentration depth to the coherence length of a material is known as the Ginsburg-Landau constant K (K $= \frac{\lambda}{\xi}$). A material is a type I superconductor for the Ginsburg-Landau constant K $= \frac{\lambda}{\xi} < \frac{1}{\sqrt{2}}$ and a type II superconductor for K $= \frac{\lambda}{\xi} > \frac{1}{\sqrt{2}}$ [3, 4, also page 19-20 of ref:12].

1.2.1 Type I superconductors

Type I superconductors expel an external magnetic field from their interior, upto a thermodynamic **critical field H_C**. For external fields above H_C the superconductor turns into normal material and allows the external fields to penetrate to the interior of the superconductor. For fields < H_C (Meissner state) Type I superconductor acts as a perfect diamagnet so that χ = -1 and M = -H and for fields > H_C (normal state) χ = 0 and M = 0. Figure 1.2 (a) shows the variations of internal field with external field for a type I superconductor.

1.2.2 Type II superconductors

Below a **lower critical field H_{C1}**, a type II superconductor behaves as that of a type I superconductor and expels any magnetic field from its interior. For fields above the H_{C1} the external magnetic field starts to penetrate into the interior of the type II superconductor in the form of quantized flux vortices. These quantized flux vortices are known as fluxons and each fluxon is a tube of radius of the London penetration depth $\lambda(T)$ in which superconducting screening currents circulate around a small non superconducting core of radius $\xi(T)$. The flux carried by a single fluxon is $\Phi_0 = \frac{h}{2e} = 2 \times 10^{-15}$ Wb [3, 4]. As the external field increases, more and more flux vortices are created at the surface of the superconductor and are penetrated into the interior, and they arrange themselves in a regular lattice. This state, called the mixed state or **vortex state** is important for the practical applications. As the fields increases further, the flux vortices fill the superconducting matrix and thus reduce the superconducting area. At a particular high field, called the **upper critical field H_{C2}**, the entire superconducting area is filled by vortices and the superconductor turns into a normal material. For fields < H_{C1} (Meissner state) type II superconductor acts as a perfect diamagnet so that χ = -1 and M = -H, for fields > H_{C1} and < H_{C2} (mixed or vortex state) magnetic field penetrates in the form of

quantized vortices so that 0 > χ > -1 and 0 > M > -H and for fields > H_{C2} (normal state) χ = 0 and M = 0. Figure 1.2 (b) shows the variations of internal field with external field for a type II superconductor. Figure 1.2 (c) and (d) show schematic H−T phase diagrams for type I and type II superconductors respectively. The H_{C1} is of order of 10−100 mT for most of the type II superconductors, while they have very high H_{C2} values of several tesla.

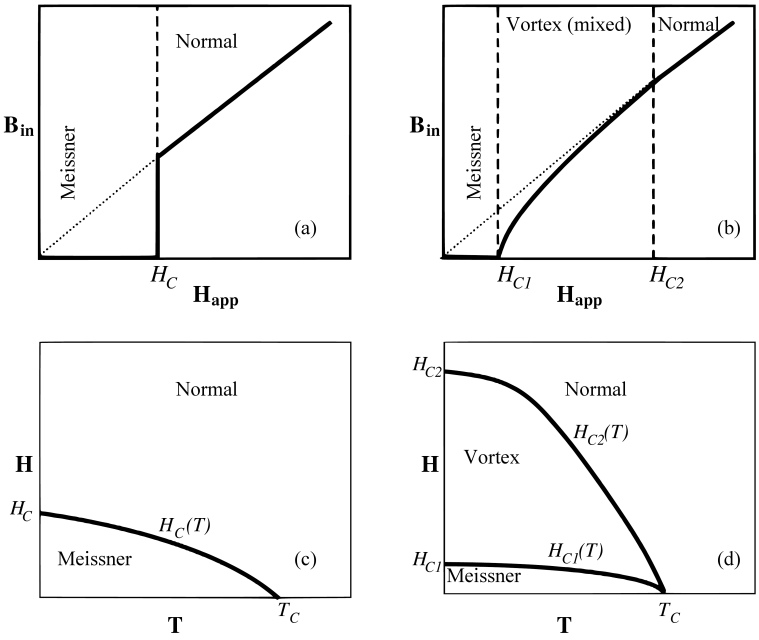

Figure 1.2: Variation of internal field with external field for (a) type I and (b) type II superconductor. (c) and (d) shows the H-T phase diagram of type I and type II superconductor.

1.2.3 Vortex (mixed) state of Type II superconductors: Flux pinning and critical current density

For a type II superconductor, in the vortex state the superconductor is filled with fluxons. These fluxons have a normal core of quantized magnetic field lines. The number of quantized vortices increases with external field and in

a perfect superconducting crystal the competition between the inter-vortex repulsion and the magnetic pressure from the outside field causes the vortices to arrange themselves in a regular lattice. But in real superconductors there are defects, which pin the vortices, and stop from moving, disrupting the Flux Line Lattice (FLL) [4, 5]. But with increasing temperature (T) and field (H) the flux lines attain enough energy to depin from the pinning sites and start to migrate to form FLL. Figure 1.3 shows a schematic diagram of vortex state of a type-II superconductor.

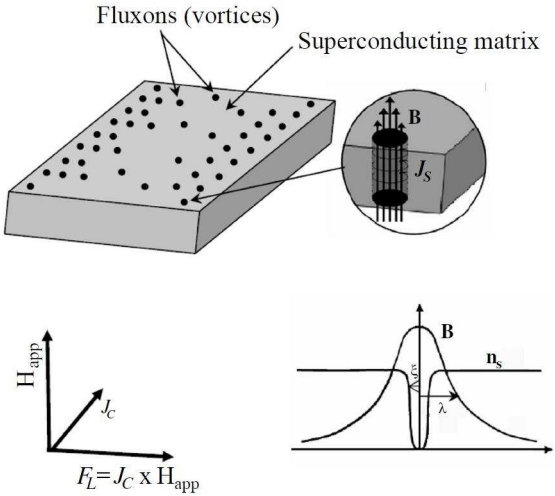

Figure 1.3: Type II superconductor in the vortex state, showing flux vortices and the variation of superconducting electron density (n_S), and the field (B) in a vortex core. J_S is the superconducting circulating screening currents associated with the vortices.

During a macroscopic transport current flow through the superconductor, the fluxons experience a Lorentz force $F_L = J_C \times B$, in a direction perpendicular to both the current density and field. This Lorentz force tends to move the flux lines. The lattice defects or imperfections can pin the flux lines to some extend and once the Lorentz force exceeds this pinning force, the flux lines start to move. The flux lines experience some viscous resistance in their movement and cause energy dissipation in the superconductor. The flux flow induces an electric field $E = n_f \Phi_0 \nu_f$ (where n_f is the number of fluxons, Φ_0 is the quantum of flux and ν_f is the veloc-

ity of flux flow) and the transport current becomes dissipative. The flux flow and dissipation are higher for increased temperature or applied field. This limits the non dissipative $J_C(T, H)$ to a value, defined by the balance of the pinning and Lorentz forces [page 94-102 of ref:12 and chapter 9, page 303 of ref: 6]. Due to the flux flow, for an applied field above a limit, called the **irreversibility field H_{irr}**, (much below the upper critical field H_{C2}) energy dissipation starts and hence dissipation free transport current flow stops. In order to sustain the non dissipative current flow at high fields and temperatures the flux lines must be pinned.

The physics and engineering of vortex dynamics and flux pinning are highly interesting and are active research fields in applied superconductivity. The atomic or crystal defects such as grain boundaries, voids, strains, twin planes, inhomogeneities and secondary phases present in real superconductors are effective pinning sites.[1] The flux pinning can be improved to maximize J_C in practical conductors by *tailoring the microstructure* of the superconductor and in the optimized case the J_C can enhanced by one or two orders of magnitude in practical superconductors in technically useful magnetic fields.

In a practical superconductor, there will be a large number of flux lines interacting with each other and interacting with different pinning centers. The bulk flux pinning depends on the basic interactions between the individual flux lines (flux line-flux line) and between flux lines and individual pinning centers (flux line-pinning center). For a weak interaction between the flux lines (the magnetic interaction between flux lines is repulsive) the FLL acts as a two dimensional elastic crystalline solid. In this case there will be as many flux lines as possible are located on the pinning centers. If the number density of flux lines is less than or equal to the number of pinning centers (for instance in small applied fields) then each flux line is

[1] To nucleate a flux line within the superconductor, the system must provide enough energy (This energy per unit length of flux line, called the condensation energy, is given by the volumetric free energy due to the magnetic field within the flux line) to convert the core of the flux line to the normal state. If the flux line is centered on a flux pinning center such as a void or normal conducting inclusion of radius ξ, the condensation energy needed to produce the normal core of the flux line would be saved, and the flux line would see a lower free energy at the location of the void than it would be in the bulk. That is, a pinned vortex has a lower free energy than a free vortex in a superconductor. The result of this free energy change is that the flux line requires an increase in its energy per unit length equal to the condensation energy, to move away from the flux pinning center. Thus, the flux pinning center holds the flux lines from moving and hence reduces the dissipation [page-97-102 of ref: 7].

individually pinned and the bulk pinning force is large. On the other extreme in which the interaction between the flux lines is strong, the FLL acts as a two dimensional rigid crystalline solid. In this case, the bulk pinning force due to a collection of randomly distributed pinning centers will be small over the completely rigid FLL. However, for practical polycrystalline systems the correct description of pinning lies somewhere between these two extremes of direct summation and rigid FLL lattice [page-97-102 of ref: 7].

1.3 Superconducting materials

Mercury (Hg) is the first material observed to be superconducting in 1911 by Kamerlingh Onnes. Now, nearly after one century of the discovery of the phenomena, thousands of materials including metals, alloys, binary and multicomponent compounds of metals, ceramics, doped fullerenes and organic molecules are found to be superconducting with transition temperatures ranging from a milli kelvin to $\sim$ 150 K [8–10]. Many materials, non-superconducting under normal conditions, become superconducting under pressure, upon irradiation or charge doping, and some materials in thin film form [11].

Table 1.1 gives some of the superconducting materials of various classes. Among the simple elemental superconductors Li has the highest T_C of 20 K under high pressure while Nb has the highest T_C of 9.25 K under normal conditions. Highly conducting ordinary metallic materials like Cu, Ag and Au are non-superconductors even to the lowest temperature studied. Al is superconducting and has a T_C of 1.18 K in bulk and 3.6 K in thin film form. Intermetallic materials with the A15 crystal structure such as V_3Si, Nb_3Sn, Nb_3Ga and Nb_3Ge have higher transition temperatures than the elemental superconductors. Of these A15 superconductors, Nb_3Ge has a T_C of 23.2 K and this was the highest T_C for a superconductor for many decades, before the mid 80's [chapter 3 page 59 of ref: 6]. All these simple elemental, alloy and intermetallic superconductors that have T_C at or below the $\sim$ 23 K are known as the low temperature superconductors (LTS) and are well explained by the BCS theory of superconductivity.

The discovery of superconductivity in copper oxide systems was a breakthrough in superconductivity research. In 1986 Bednorz and Müller reported the existence of superconductivity in LaBaCuO, at a surprisingly

Table 1.1: Superconducting materials under various classifications. Data for the table are taken from [6, 10–17]

Type/class	Example	T_C (K)
Elements	Hg	4.2
	Nb	9.2
	Li (under pressure)	20
	B (under pressure)	11
	W (thin film)	5.5
	Pd (irradiated)	3.2
Amophous materials	$U_{85.7}Fe_{14.3}$	1.0
	$Th_{80}Co_{20}$	3.8
Alloys	NbTi	9.0
	MoTc	16.0
A15 type (A_3B)	Nb_3Sn	18.0
	Nb_3Ge	23.2
Laves phase (AB_2)	ZrV_2	9.6
	$LaOs_2$	8.9
Chevrel phase ($AB_xMo_6l_8$)	$PbMo_6S_8$	12.6
	$Sn_{1.2}Mo_6S_8$	14.2
Heavy electron systems	UPd_2Al_3	2.0
Organic materials	$(TMTSF)PF_6$[a]	0.9
	$(BEDT\text{-}TTF)_2Cu[N(CN)_2]Br$[b]	0.6
Magnetic material	$ErRh_4B_4$	10
Doped Fullerenes	Cs_3C_{60}	47.4
	$Rb_{2.7}Tl_{2.2}C_{60}$	45
Borides	**MgB_2**	**39**
	ZrB_{12}	5.82
	YRh_4B_4	11.3
Borocarbides	YPd_2B_2C	23
Oxides	$Ba_{0.6}K_{0.4}BiO_3$	30
	$LiTi_2O_4$	13.7
Cuprates	$YBa_2Cu_3O_7$	92
	$Bi_2Sr_2Ca_2Cu_3O_{10}$	110
	$Hg_2Sr_2Ca_2Cu_3O_{10}$	135
Oxypnictides	$SmO_{0.9}F_{0.1}FeAs$	55
	$NdO_{0.82}F_{0.18}FeAs$	51

[a] TMTSF = tetra-methyl-tetra-selenium-fulvalene
[b] BEDT-TTF = bis-ethylene-dithia-tetra-thiafulvalene

high T_C of $\sim$ 30 K, [18], initiating the era of high T_C superconductivity (HTS). The discovery of superconductivity in the mixed YBaCuO compound system with T_C above 90 K higher than the boiling temperature of

liquid nitrogen (77 K) was another milestone in the search for new HTS materials [19, 20]. For years, copper oxide systems dominated the condensed matter field research and now a lot of HTS materials have been discovered, with T_C above 100 K.

The discovery of superconductivity in MgB_2, a binary intermetallic with an unusually high T_C of 39 K by Jun Akimitsu's group [21] in Japan in 2001 surprised the condensed matter research field. Though the T_C of MgB_2 is much below the copper oxide based HTS, it generated a great deal of interest in both theoreticians and experimentalists worldwide. MgB_2 has the highest T_C among non-cuprate oxide bulk superconductors, under normal conditions. Recently Iron based layered compounds are found to be superconducting with T_C comparable and higher to that of MgB_2. T_C values of above 50 K and H_{C2} values of the order of 100 T were reported for the Iron based superconductors [16, 17, 22]. However they contain the toxic arsenic and the fabrication into wires/tapes with better properties is not standardised yet. MgB_2 is free from most of the limitations of HTS and has a higher T_C than the presently using LTS materials.

1.4 Applications of superconductors

The unusual physical properties of superconductors resulted in some remarkable applications in specific areas. Superconducting materials can replace the conventional materials in many applications and with better performance. The choice between conventional and superconductive materials is generally related to technical and economical aspects, and the latter is the main factor limiting the widespread use of superconductors in practical applications. However, in many fields the superconducting technology is often the only possibility for achieving the required performance. By using superconducting components, the size and weight of instruments and devices can be reduced compared to conventional techniques which is an important issue for fields like space applications. Today superconductors have a wide range of commercial and industrial applications in energy production, storage, and its distribution, in sensor materials, in microwave communication systems and most importantly in high field magnets. The special issue of *Supercond. Sci. Technol.* published on 15 February 2006 discusses the status and future of some major applications of superconductivity in different countries. The main application sectors of superconducting materials are tabulated in table 1.2.

Table 1.2: General applications of superconductors

Area/Field	Applications
Energy/Power: Generation & Storage	Generators, SMES, Superconducting bearings for flywheel storage
Energy/Power: Distribution	Cables, Transformers, Current leads, FCLs, Motors.
Magnets	NMR, MRI instruments, Magnetic confinement of plasma in Fusion reactors, Particle accelerators, High field magnets.
Electronics	In microwave filters, Digital logic circuits as RSFQ, Sensor applications
Biomedical	Detection of extremely small neuromagnetic fields, Magnetoencephalanography (MEG), Magnetocardiography (MCG)
Industrial	Magnets for shielding and separation, sensors
R & D	Superconducting RF cavities in particle accelerators, Synchrotrons and High field magnets.
Other applications	Magnetic levitation, Magnetohydrodynamics, Space applications

Superconducting magnets have exclusive uses in some commercially available instruments like MRI instruments in medical field, and for high field magnets for NMR and particle accelerators. NbTi is the mostly used superconducting material for MRI magnets. For high field magnets, Nb_3Sn is mostly used and some HTS based inserts are also developed for still higher fields. HTS based magnets inserted in high field LTS magnets are tested upto $\sim$ 25 T [23]. Superconducting solenoids are being used for bending and focusing of high energy particles in high-energy particle physics labs like BNL, CERN, DESY and the Fermi Laboratory. Besides solenoids, superconducting RF cavities are also find applications in particle accelerators. Large-scale application of superconducting cavities to electron and ion accelerators is established at many laboratories around the world [24]. With the development of cryocoolers, various kinds of cryogen free superconducting magnets with fields of the order of 20 T are now developed for practical applications [25, 26]. In fusion reactors, the plasma temperature needed for energy production is several million degrees, and high field superconducting magnets are required to confine the plasma. The International Thermonuclear Experimental Reactor (ITER) project is engaged in the development of fusion reactor and a large quantity of LTS superconductors is being manufactured for the project [27, 28].

Since the supercurrent in a superconductor persists for a very long time, superconductors have applications in energy storage also. Superconducting Magnetic Energy Storage (SMES) can store mega joules of energy, without resistive losses. SMES systems capable of storing mega joules of energy has been tested and installed in various places. They are receiving more importance with regard to future electrical power grids. Details of a 3MJ/750 kVA SMES system developed by the Korea Electrotechnology Research Institute (KERI) can be found in [29].

One of the peculiar properties of superconductivity is that they find applications in extremely weak and extremely high magnetic fields. Superconducting magnets provides high fields while superconducting thin films are used for the detection of extremely weak fields. The Superconducting Quantum Interference Device (SQUID) based on the Josephson effect is the most sensitive magnetometer. SQUID based technology is widely used for the non-invasive clinical measurements of weak biomagnetic fields: especially in the mapping of extremely weak magnetic signals from the human brain. In material science and physics research SQUID based magnetometers are being used for magnetic characterization of materials. The Magnetic Property Measurement System (MPMS) and Physical Property Measurement System (PPMS) are two well-known commercial instruments based on superconductor technology.

Superconducting cables can replace the conventional copper/aluminium based cables in electric power transmissions. Cost of the superconducting technology compared to the conventional is the main hurdle in the limited use of superconductors in this sector. Conductors made of BSCCO-2223 are being applied in variety of power transmission cables and distribution cables [30]. The world's first high temperature superconductor power transmission cable system in a commercial power grid system was energized recently in New York, USA.[1] Another major application of superconductors in electric power grid is for the control of fault currents in electrical transmission and distribution networks, as Superconducting Fault Current Limiters (SFCL). Fault Current Limiters (FCL) restrict the maximum current through a network and protect the devices from an accidental over current. Several groups are actively involved in developing SFCL for industrial applications. A 1.2 MVA 10.5 KV Bi2212 LN_2 cooled SFCL

[1]The 138 kV, $\sim$ 609 m cable system is the longest superconducting system in the world energized on 22 April 2008. Information is from www.amsc.com/pdf/HTSC_AN_0109_A4_FINAL.pdf

has been developed and commissioned for protecting a hydroelectric plant auxiliary transformer circuit [page 547 of ref: 7].

Superconducting thin films are finding more applications in electronic industry. Rapid Single Flux Quantum (RSFQ) is an emerging digital electronics technology that relies on quantum effects in superconducting materials to switch signals, instead of transistors. The quantum pulses are switched by Josephson junctions. Superconducting components such as resonators, filters and delay lines with performance far superior to conventional technology are being widely used in microwave electronics. HTS microwave technology is a promising one, especially at frequencies below 3Hz. Another important application of superconductors is magnetic levitation in transportation (eg: Maglev trains). For maglev systems YBCO is preferred, since it exhibits high magnetic irreversibility field at LN_2 temperatures and has the ability to grow into large grains. Due to the expulsion of magnetic field in the superconducting state, a superconductor can be used for magnetic shielding applications.

Among the various applications described above MgB_2 has the potential of replacing existing superconductors in many fields with improved performance and/or low cost. The possible applications of MgB_2 conductors include magnets for MRI, fusion reactors, high energy particle accelerators, and for future high field magnets. Other possible applications of MgB_2 includes superconducting transformers, motors, generators, SMES and particularly in SFCLs. Besides the conductor applications MgB_2 thin films/junctions can find a place in future electronics also.

1.5 Relevance of MgB_2

As discussed in the previous section superconductors have important practical applications in many fields. The present and future applications have two potential market for superconducting wires: high field magnet applications (such as NMR, MRI magnets, magnets for particle accelerators and plasma confinement in fusion reactors) and electrical power sector (applications such as transmission cables, SMES, transformers, FCLs, motors, generators).

Though thousands of materials are found to be superconducting, only a handful of them are useful for practical applications. Table 1.3 compares

Table 1.3: Properties of MgB_2 and other practical superconductors. Order of J_C values are at 4.2 K, in self-field. H_{C2} values are at 4.2 K. Data are taken from [16, 31–38]

Material	T_C (K)	Anisotropy	J_C (A/cm^2)	H_{C2} (T)	$\xi(0)$ (nm)	ρ(at T_C) $\mu\Omega$cm
NbTi	9	Negligible	10^6	11-12	4-5	60
Nb_3Sn	18	Negligible	10^6	25-29	3	5
Nb_3Al	20	Negligible	10^6	30-45	4-5	10-60
MgB_2	39	1.5-5	10^6	30-40	5-12	0.4
FeAs based	25-56	8-15	10^5	25-100	2-10	200-10^4
Bi2223	110	50-200	10^7	>100	1.5	40-60
YBCO	92	5-7	10^6	>100	1.5	150-800

some of these superconducting materials with MgB_2. The most widely used commercial superconductors are NbTi and Nb_3Sn, two LTS materials. NbTi, having a T_C of 9 K and H_{C2} (4.2 K) $\sim$ 10-12 T, has high strength and ductility and is easy to fabricate into long wires. NbTi occupies most of the low field magnets in commercial MRI instruments. The high energy physics (HEP) community and the MRI industry are the main consumers of NbTi over the years. The use of NbTi is limited to fields $<$ 10 T and the operation of NbTi needs liquid helium temperatures, which makes its use costly. Nb_3Sn has a T_C of $\sim$ 18 K and H_{C2} (4.2 K) of more than 20 T and is used in low temperature high field magnets. Though it offers much higher fields and operating temperature compared to NbTi, it is brittle, quite sensitive to strains and difficult to fabricate, and hence more costly than the NbTi. Both NbTi and Nb_3Sn had undergone many years of research and are commercially available. Another A15 material Nb_3Al with much higher field capacity and strain tolerance than the Nb_3Sn is considered for conductor development. Nb_3Al has a T_C of 20 K and H_{C2} of 40 T at 4.2 K. However the manufacturing of Nb_3Al conductor with good properties is extremely difficult and it will take few more years to enter into the commercial market. The nearly discovered FeAs based materials show superconductivity with T_C 26-55 K and H_{C2} values 20-100 T, however the preparation of quality wires/tapes based on these materials is extremely difficult.

Most of the HTS materials have T_C above 77 K and higher H_{C2} values than the LTS. But the HTS conductors faced many technical problems in making wires and coils. Their conductor fabrication is not so easy as compared to the LTS materials and needs costly Ag as sheath material and

the field performance at higher temperatures is not promising. The most important and commercially interesting HTS are BSCCO (Bi-2223 and Bi-2212) and YBCO (Y123). Bi-2223 has a T_C of 110 K, Bi-2212 has a T_C of $\sim$ 85 K, and the T_C of YBCO is $\sim$ 92 K. The H_{C2} of all the three HTS is more than 100 T at 4.2 K. BSCCO conductors are fabricated in tape geometry using the Powder-In-Tube (PIT) method. Ag sheathed BSCCO conductors known as the first generation HTS conductors are being commercially produced by a number of companies like American Superconductors, Sumitomo Electric Industries Ltd etc. Coated conductor technique is most suitable for YBCO. YBCO based coated conductor is considered as the second generation HTS conductors. HTS have high anisotropy and hence the current carrying capacity is low in untextured conductors. Due to their high anisotropy, for practical applications, for BSCCO uniaxial and for YBCO biaxial texturing is preferred. The HTS materials also have weakly connected grain boundaries so that the intergrain connectivity is also a big problem. For YBCO conductors grain orientation is also important.

MgB_2 has a higher T_C of 39 K as compared to the conventional LTS and is free from most of the limitations of HTS. Thus comparing with currently using LTS, NbTi and Nb_3Sn, MgB_2 has the advantage of higher T_C and H_{C2}. Compared to most of the HTS MgB_2 has a T_C two to three times lower. The main advantage of MgB_2 compared to HTS is that in the bulk polycrystalline form it exhibits a critical current density three orders of magnitude higher than polycrystalline HTS. MgB_2 has weak link free grain boundaries and the grain boundaries act as strong flux pinners. Doped MgB_2 wires have already reached H_{C2} values as high as 33 T, higher than that of Nb_3Sn and a record high value of 55 T in coated fibers [39]. Figure 1.4 shows a comparison of H-T phase diagram of typical MgB_2 with the NbTi and Nb_3Sn. Primitive Powder-In-Tube conductors of MgB_2could attain nearly 10^6 A/cm^2 critical current densities in self field at 4.2 K. Experiments on thin films suggest more than 10 times higher J_C values for wires or tapes with smaller grain size, full density, and perhaps with suitable additives. MgB_2 based magnets are already tested for low field applications and MgB_2 seems to be the most promising material for next generation high field magnets and a strong competitor for Nb_3Sn and NbTi.

Good quality MgB_2 conductors with high critical current density can be prepared with heat treatment of PIT *in situ* wires/tapes at 600-800 °C for 5-30 minutes. This is really an advantage from an industrial point of view since many of the HTS and LTS need much higher temperatures and/or

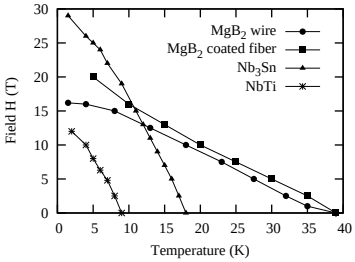

Figure 1.4: Comparison of H-T phase diagram of typical MgB_2 and the LTS.

durations for manufacturing. The density of MgB_2 is 2.6 g/cm^3, much lower than other superconductors and ordinary copper. This makes MgB_2 suitable for specific light-weight applications, such as space application. Both Mg and B, the reactants of MgB_2 and the sheath materials used are inexpensive. Thus MgB_2 is economical for practical applications and the cost/performance ratio for MgB_2 is much lower than other superconductors [40, 41].

MgB_2 is most suited for applications around 20-25 K were cryocoolers can be used for cooling. Several manufacturers have already fabricated stabilized MgB_2 conductors in kilometers of length both by *ex situ* and *in situ* method, for various applications (review articles [42–44]). Industrial scale production of MgB_2 conductors has started by manufactures Hyper Tech Research Inc., Columbus, Ohio and Columbus Superconductors, Genova, Italy. One of the major applications of MgB_2 in the near future is for MRI magnets. MRI instruments based on MgB_2 operating at 20-25 K using cryogen free cryocoolers will be more economical than the conventional NbTi based MRI instruments. Laboratory scale as well as demonstration level MgB_2 based MRI systems with high performance and low price are developed in many countries [45]. Based on the use of MgB_2 conductors supplied from Columbus superconductors, ASG superconductors together with Paramed Medical Systems recently constructed an open MRI system [46].

MgB_2 has also applications as current leads and fault current limiters in specific areas. The first application of MgB_2 conductors as current leads was realized on the Japanese satellite ‘Suzaku’ which was launched in July 10, 2005 in Japan. Ultra thin MgB_2 conductors with diameters down to

50 μm have been developed for the current lead and liquid hydrogen level sensor applications [47]. With operational advantages at intermediate temperature (20-30 K) and low cost, MgB_2 is very attractive as a cost effective FCL. Work has been reported on the current limiting properties of MgB_2 wires at 50 Hz in the 20-30 K range [48, 49]. MgB_2 based FCL can be a strong competitor for the inductive FCL coils using HTS conductors. MgB_2 based thin films and tunnel junctions are being fabricated with reasonably good properties for applications in electronics and allied areas. For RSFQ applications, a reliable MgB_2 technology could boost superconducting electronic applications. The two band gap nature of MgB_2 can also be exploited for novel applications [50].

In a nutshell MgB_2 is quicker (formation), cheaper (cost/performance) and better (for specific applications) compared to many of the practical superconductors.

1.6 Properties of MgB_2 superconductor

Magnesium diboride (MgB_2) is a binary intermetallic compound with a simple hexagonal crystal structure (AlB_2 type structure). It is a brownish-black material, known since early 1950's to the materials science community and is even commercially available. In 1953 Jones and Marsh [51] and Russell *et al* [52] reported the formation of MgB_2 phase with the interaction of Mg and amorphous B in hydrogen and/or argon atmospheres. For the Mg−B system, besides the MgB_2 phase, many observed/proposed formation of other magnesium boride phases such as MgB_4, MgB_6, MgB_7, MgB_{12}, MgB_{20} etc [52–57]. Now, formation of the four phases MgB_2, MgB_4, MgB_7 and MgB_{20} are well established [55–57].

1.6.1 Crystal structure of MgB_2

MgB_2 has hexagonal crystal structure (figure 1.5) with space group *p*6/*mmm* [12], which is common among diborides. The boron atoms form graphite like honeycomb network and the Mg atoms are located at the pores of these hexagons. In the unit cell the atomic positions are (0,0,0) for Mg (Weizkoff symbol 1a) and ($\frac{1}{3}$, $\frac{2}{3}$, $\frac{1}{2}$) and ($\frac{2}{3}$, $\frac{1}{3}$, $\frac{1}{2}$) for B (Weizkoff symbol 2d) atoms [58, 59]. The coordination polyhedra are ($B_{12}Mg_8$) for Mg and (Mg_6B_3) for B. The lattice parameters are a = 3.084 Å and c = 3.524 Å and the inter atomic distances are: B-B intralayer 1.780 Å, Mg-Mg intralayer 3.084 Å,

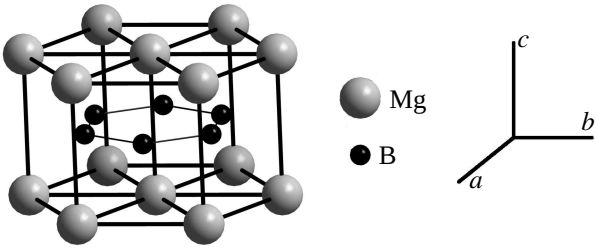

Figure 1.5: Crystal structure of MgB_2.

Mg-Mg interlayer 3.524 Å and Mg-B 2.5 Å [12, 59]. The in-plane B-B distance is almost half that of the inter-plane B-B distance.

1.6.2 Physical and superconducting properties of MgB_2

MgB_2 is a brittle material like the HTS materials. Typical polycrystalline MgB_2 has a grain size of 10 nm-10 μm [60–64]. The anisotropy of MgB_2 is 1.5-5 [32–34] and is low compared to the highly anisotropic HTS. This low anisotropy means there is no need of texturing as in the case of HTS for making wires with high J_Cs. The coherence length of MgB_2 is $\sim$ 5-12 nm and the penetration depth is 100-140 nm with a GL factor of K $\sim$ 26 [35] at absolute zero. Due to the large coherence length, higher than the inter atomic spacing, the weak link problem is not severe in MgB_2. MgB_2 has two superconducting gaps in the superconducting state, $\Delta_1 \sim$ 5-7 meV and $\Delta_2 \sim$1.5-2.0 meV [65, 66].

MgB_2 has a very sharp T_C around 39 K [12, 66] and has a very narrow transition width of less than 1 K. The T_C of MgB_2 is nearly double that of Nb_3Sn and nearly four times that of NbTi but still much lower than the liquid nitrogen temperature. The isotopic B^{10} substitution slightly increases the T_C to 40.25 K [67]. The research for enhancing the T_C by substitutions of aliovalent and isovalent atoms with different radii hasn't given satisfactory results as expected. Most of the substitutions resulted in a decrease of T_C. The substitution of Al to the Mg site and C to the B site reduced the T_C and the superconductivity is lost for higher doping [68–70]. The substitution of Al caused a structural transition at higher levels [68]. The normal state of MgB_2 is metallic and the normal state resistivity is much lower than that of other superconductors. For clean MgB_2 samples a very low

normal state resistivity $\rho(T_C)$ of 0.4 $\mu\Omega$cm and a high Residual Resistivity Ratio (RRR) of $\sim$ 20 are observed [71].

MgB_2 is a type II superconductor and is well within the clean limit of superconductivity. The depairing current density is $\sim 10^7$ A/cm^2 [72], one order of magnitude lower than that of the HTS materials. The observed transport critical current densities are of the order of 10^6 A/cm^2 at 4.2 K in self field, $\sim$3.8 $\times$ 10^4 A/cm^2 in 6 T and 10^4 A/cm^2 in 8 T [73]. The transport J_C is of the order of 10^4 A/cm^2 at 30 K in 1 T field [74]. For Cu stabilized multifilamentary conductors a transport J_C of 1.75 $\times$ 10^5 A/cm^2 was measured at 5 T, 4.2 K [75]. The intergranular J_C of MgB_2 is also high compared to HTS materials. Pure MgB_2 has low lower critical field $H_{C1}(0)$ of less than 50 mT [76, 77], upper critical field H_{C2} of 15-20 T and irreversibility field 6-12 T [35, 71, 76, 78] at 4.2 K. Doped conductors have high H_{C2} and the maximum H_{C2} observed for SiC added MgB_2 wires is 33 T, much higher than that of the Nb_3Sn [79].

1.6.3 Advantages of two gap superconductivity

MgB_2 is the first superconductor which showed two distinct energy gaps in the superconducting state. The two energy bands arise from the σ (formed from the sp^2 hybrids of boron $2s$ and $p_{x,y}$ orbitals) and π (originated from the boron p_z orbital) bands. For a detailed description of the origin of superconductivity and the energy bands please see the review article [80]. From an application point of view the two gap nature is significant and a detailed discussion on this is presented in [81]. For the single band LTS increase in $H_{C2}(0)$ is expected by the introduction of charge-carrier scattering impurities into the lattice structure. The charge scattering causes decrease in coherence length and increase in the H_{C2} values. This rule is used for the design and manufacturing of LTS materials over the years. Being a two band superconductor, MgB_2 has three scattering channels with different scattering rates: the intra-band scattering within the σ and π bands and the inter-band scattering between the σ and π bands. Tuning of these inter and intra band scattering rates make it possible to achieve high H_{C2} values in MgB_2, much beyond to the reach of NbTi and Nb_3Sn. Some best MgB_2 polycrystals have shown H_{C2} of 40-50 T and highest H_{C2} of $\sim$ 74 T was reported for a thin film [82].

1.7 Critical Issues (major challenges) of MgB_2

For commercial applications of MgB_2 multifilamentary conductors with large number of fine filaments having high H_{C2} and $J_C(T, H)$ values must be produced in long lengths at a low cost. The fabrication of long length MgB_2 wires is relatively easy and more economical. However there are many critical issues, which are to be addressed seriously. These include the fabrication of good quality long length conductors or cables at a reduced cost and the improvement in the performance of the conductors.

1.7.1 Issues regarding fabrication

Phase purity and homogeneity of the superconductor are important factors, which need some attention in the fabrication of long length conductors. Since Mg is highly volatile and has strong affinity to oxygen in the *in situ* fabrication, Mg loss and MgO formation are the main causes for the inhomogeneities and impurities. Mg loss can cause non-stoichiometry and the formation of higher borides (like MgB_4 or MgB_7) as impurites. Formation of MgO and other impurities limits the active current carrying area and weaken the grain connectivity and hence reduces the critical current density [12, 83, 84]. Many prefer synthesis in excess Mg environment and inert/vacuum atmosphere to compensate the Mg loss and oxidation.

The wide difference in melting points of Mg (650 °C) and B (2080 °C) doesn't favor solid-solid or liquid-liquid reactions. The sinterability of MgB_2 grains are poor also. The *in situ* samples formed by the liquid-solid reaction of Mg and B are highly porous and have low density compared to the theoretical density of MgB_2. This is mainly due to the voids remaining from the prior Mg particles during the MgB_2 formation ($V_{Mg} + V_{2B} > V_{MgB_2}$) [84]. The high porosity also limits the grain connectivity and hence the intergrain current transport [84]. More research and new techniques are needed to decrease the porosity and to increase the density of the samples.

Another problem with the fabrication is the reactivity of Mg with most of the commonly used sheath materials. The reacted secondary phases at the sheath core interface act as barrier for the current transfer from the outer sheath to the superconducting core and also restricts the local heat developed to flow out to the sheath, during a possible quenching. Barrier materials such as Nb or Ta can reduce the reaction between the core and sheath, but both Nb and Ta are expensive. Another major obstacle for

practical MgB_2 conductors is the insufficient thermal stabilization, leading to quenching of the conductor in high currents. Conductive Cu gives better thermal stabilization for LTS materials and Ag for Bi based conductors. For MgB_2 also Cu sheath with Nb or Ta barrier and SS or Fe reinforcement can have good thermal stabilization and mechanical strength.

1.7.2 Issues regarding property improvement

Though MgB_2 has high self field J_C comparable to NbTi and Nb_3Sn at low temperatures, the J_C falls rapidly with field and temperature, due to poor vortex pinning, and low irreversibility field. Since MgB_2 has a rigid lattice with two simple elements in the structure, the density of defects produced during synthesis is too low to provide sufficient flux pinning at higher fields. Only grain boundaries are effective pinning centers in pure MgB_2, thus MgB_2 samples with fine grains are needed for better properties. The irreversibility field of MgB_2 is only half of its upper critical field ($H_{irr} \sim 0.5 \times H_{C2}$), whereas for NbTi and Nb_3Sn the irreversibility field is close to their respective upper critical fields ($H_{irr} \sim 0.8 \times H_{C2}$). The low irreversibility field and poor flux pinning cause rapid decrease in J_C at high fields. This limits the temperature and field range where MgB_2 could be superior to Nb_3Sn to above 10 K and 2-3 T. In order to compete with the Nb_3Sn for liquid helium temperature applications, the $J_C(H)$ of MgB_2 must be improved. This can be achieved by improving the flux pinning at high fields, increasing the H_{irr} and decreasing the electromagnetic anisotropy etc [84–86].

1.8 Synthesis of MgB_2 superconductor

During the last 8-9 years, various fabrication/preparation methods are used to synthesis MgB_2 based superconductors in bulk, powder, thin film, wire, tape as well as single crystal forms. Since the present work focuses on bulk and wires/tapes the details of which only are discussed. MgB_2 based superconductors are prepared either by sintering of commercially available MgB_2 powder or from elemental Mg and B powders. Preparation of MgB_2 based superconductors using commercial/as-prepared $MgB_2$is known as *ex situ* while from Mg and B powders/sources is known as *in situ* method. Both *ex situ* and *in situ* have their merits and demerits.

In the *ex situ* method the commercial MgB_2 powder is pelletized and heat treated at elevated temperatures of 800-1200 °C for 1-5 hours in vacuum or inert atmosphere. The final properties of *ex situ* samples depends on the quality of commercially available powder. The *ex situ* MgB_2 has better homogeneity and higher density than the *in situ* one. However for better superconducting properties the *ex situ* samples need much higher sintering temperatures and the doping of other elements is restricted compared to the *in situ* samples. The *in situ* method produces MgB_2 with low density, but has the advantage of easy tailoring by chemical addition/doping for better superconducting properties.

1.8.1 Bulk samples

Several synthesis procedures are reported for the preparation of *in situ* MgB_2 bulks with relatively low temperature and short durations of heat treatments [87–94]. The starting materials are Mg in powder/flakes/chips and amorphous/crystalline B in powder forms. Some groups use MgH_2 powder as Mg source [87, 88]. For the *in situ* preparation the starting materials (either pellet or powder mixture) are enclosed in Nb/Ta/Fe/SS/Quartz tubes/foils/ampoules and heat treated at 650-1000°C for 30 min-5 hours in vacuum or hydrogen/argon atmospheres. Considering the oxidation and vapor loss of Mg many prefer excess Mg environments also. Suitable sintering aids or mechanical alloying/ high energy milling are found to enhance the formation of MgB_2 phase at relatively lower temperatures with improved superconducting properties [89–92].

High energy ball milling allows reduction of particle size and more homogeneous mixing of the ingredients. Many groups now use this technique for the preparation of doped and undoped MgB_2 bulk samples, with fine grains and hence better superconducting properties. Contamination from the bowl, ball and milling media and particle agglomeration are two main hurdles of this method, and the performance of mechanically alloyed or high energy ball milled samples depends on various factors like nature and size of the ball and bowl, ball to powder ratio, speed and milling duration and the milling medium [91, 92].

Most of the *in situ* samples prepared by these methods have high porosity and very low density (only 50% of theoretical density in many cases). Methods like high pressure sintering (HPS) [76, 95, 96], hot isostatic pressing (HIP) [97, 98] and double step sintering (2-stage sintering) [99, 100]

are used to get highly dense MgB_2 bulk samples. Both high pressure sintering and hot isostatic pressing use high pressure for the densification and reduction of porosity. In these methods the precursor is subjected to high pressures of 0.5-5 GPa during the high temperature heat treatment at 700-1000 °C. The reported properties after HPS or HIP synthesis show some scatter with respect to the pressing system. The main advantage of this technique is the possibility of producing extremely high dense MgB_2 samples: even density close to 100% were prepared for an *ex situ* sample by this method. The main disadvantage is the sophisticated and costly instruments, which also limit the sample dimensions used for the method. Though the method is most suitable for bulk samples, some groups used it for small length wire/tapes with limited success. The reactive liquid Mg infiltration technique introduced by EDISON SpA (Italy) can produce bulk MgB_2 samples of different shape with higher densities. The method involves the reaction of liquid Mg with the B powders in a closed metallic container [101].

1.8.2 Wire and Tape samples

Over 50 years of conductor fabrication in LTS and 20 years of experience in HTS, helped researchers, to fabricate MgB_2 conductors of long length soon after the announcement of superconductivity in the material. Some of the fabrication techniques used for LTS and HTS can be applied to MgB_2 also. Diffusion of Mg into B fibers or wires, coating technique and Powder-In-Tube (PIT) method are employed for the fabrication of MgB_2 based conductors. Of these, PIT is the most popular and industrially preferred method.

Diffusion method

Mg diffusion into B wires is a relatively easy method by which commercially available B fibers or wires can be converted into superconducting MgB_2 wires. The first superconducting MgB_2 wires were prepared by this method [71]. Cunningham *et al* [102] also prepared MgB_2 wires by diffusing Mg into tungsten cored B fibers. By infiltrating a preform of B fibers with liquid Mg and subsequent reaction at elevated temperatures DeFouw *et al* [103] fabricated composite MgB_2 wires of several hundred continuous fibers within an Mg matrix. The phase homogeneity of the conductors produced by diffusion is poor and the method is suitable for short samples and the feasibility of making long length conductors needs to be studied.

Coating techniques

Coated conductor technique is a well known process, widely used for the fabrication of commercially available YBCO conductors. For MgB_2 high H_{C2} and J_C values in applied fields are observed in thin films [12, 104] and so coated conductor technique is being tried in some labs. K. Komori *et al* [105] used sputtering technique to make MgB_2 coated conductor in hastelloy substrate with Yitria Stabilized Zirconia (YSZ) as buffer layer. The carbon alloyed MgB_2 coated conductor fabricated by Hybrid-Physical-Chemical Vapour Deposition (HPCVD) on SiC fibers with tungsten core by Ferrando *et al* showed a high H_{C2} of 55 T and high irreversibility field of 40 T at 1.5 K [39]. Using a new processing technique called the Molten Salts Electro Plating (MSEP) MgB_2 can be coated to stainless steel (SS) [106] substrate which gives higher chemical stability, higher plasticity and higher heat conductance than the widely used ceramic substrates. Even though the superconducting properties of coated conductors are normally superior to conductors fabricated by other techniques, the scaling up of this technique is not straight forward compared to the widely used PIT process.

Powder-in-tube (PIT) method

Powder-in-tube method is the most popular method for achieving good quality wires of HTS Bi-2212 and Bi-2223. In PIT the precursor powder is filled in various metal tubes or sheaths [43, 44, 47, 60, 107–113]. The filling can be in air [107] or in an inert atmosphere [108]. These tubes are then mechanically rolled/extruded/drawn into desired size and shape followed by heat treatment. Heat treatment is usually done in vacuum or oxygen protective atmosphere. Intermediate annealing relives the stress developed during drawing or rolling. In the case of MgB_2 the metallic sheath chosen must be chemically compatible with the MgB_2 and should not degrade the superconductivity.

PIT techniques can be used for fabricating multifilamentary conductors, which withstand larger uniaxial and bend strains than single filaments and exhibit a higher thermal stability. Hyper Tech Research developed a modified PIT process for low cost continuous production of MgB_2 wires [42, 43]. In the method, known as continuous tube forming/filling (CTFF) process, the precursor powder is dispersed on to a strip of metal as it is being continuously formed into a tube. The filled overlap closed tube is then inserted into hard metallic tubes as in PIT and drawn into the desired dimensions, followed by appropriate heat treatments.

PIT method is the most preferred for manufacturing long length multifilamentary MgB_2 conductors. Long length conductors in wire geometries (circular, square or rectangular cross sections), with filaments upto 61 have been fabricated. Some solenoid and racetrack coils are also demonstrated using PIT MgB_2 conductors. Hyper Tech Research Inc. and Columbus Superconductors are producing multifilamentary stabilized MgB_2 conductors with different geometries and sheath combinations. The critical current density for good quality wires/tapes is 10^6 A/cm^2 at self-field and 10^4 A/cm^2 at 10 T, both at 4.2 K. At 20 K and self field the typical samples have a J_C of 10^5 A/cm^2 [42–44].

1.9 Improvement of Flux pinning and in-field critical current density in MgB_2

In the mixed state (vortex state) a superconductor is filled with quantized vortices (fluxons). In isotropic superconductors such as NbTi and Nb_3Sn the vortex lines are continuous and no decoupling occurs. But in HTS compounds at high temperatures and fields the 3D vortex lines melts into 2D pancake vortices [114] which are weakly coupled, whose circulating screening currents are mostly confined within the superconducting CuO_2 planes. In the case of MgB_2 the vortices are line like similar to that of LTS and there is no such decoupling of the vortex lines. As discussed earlier, in applied fields the fluxons tend to move during transport current flow through the superconductor. The movement of fluxons causes a drastic decrease in the J_C in applied fields. In order to sustain high J_C values in applied fields, the movement of fluxons must be stopped. ie. the flux lines must be pinned.

Pinning centers in conventional methods of fabrication of low T_C superconductors are developed by modifying the thermomechanical processing. Finely dispersed nanosized nonsuperconducting α-Ti phase precipitated during heat treatment is strong flux pinners in NbTi [115, 116]. For effective pinning the typical thickness of the α-Ti phase must be 1-4 nm with a separation of 5-20 nm. In the case of Nb_3Sn, grain boundaries are the dominant pinning centers [117]. The J_C of Nb_3Sn is observed to be inversely proportional to the grain size [117] at low fields. Synthesis of Nb_3Sn at low temperatures helps the formation of Nb_3Sn phase with fine grain sizes, increases number of grain boundaries and J_C at high fields. In HTS materials grain boundaries, growth dislocations, crystal structural non uniformities,

impurity phases, precipitates, oxygen vacancies and other microstructural defects can act as effective pinning centers [118–120]. The introduction of secondary phases or normal impurities to the superconducting matrix improves the flux pinning property of HTS materials [121].

Grain boundary pinning, like in Nb_3Sn is the dominating pinning mechanism in MgB_2 [61, 122–124] and the pinning improves with reduced grain size [125]. In MgB_2, since lattice structure is rather rigid and the number of elements in the structure is only two, the density of defects introduced by preparation procedures is too low to provide effective flux pinning. Pinning in pure MgB_2 is mainly provided by grain boundaries. It is found that in MgB_2 the aperiodic semicrystalline defects traped in the crystalline phase act as intense vortex pinning centers and significantly enhance the high field performance of MgB_2 [126]. Inclusions and doping can improve the flux pinning of MgB_2 strongly.

Irradiation of high energy radiation introduces artificial defects (point or extended) in a crystal. In the case of MgB_2 superconductor this type of intentionally introduced defects can act as strong flux pinners and also scattering centers: both improve the in-field J_C as well as the H_{C2}. Bugoslavisky *et al* [127] improved the high field J_C of MgB_2 by producing atomic scale defects by proton irradiation. Similar results of highly enhanced J_C and H_{C2} were observed for neutron irradiated samples [128, 129]. Though the J_C and H_{C2} increases, the irradiation technique is not easily scalable for large scale production of long length conductors. So far chemical addition/doping is most suited and preferred method for the introduction of pinning centers in practical superconductors.

Chemical addition/doping for improving $J_C(H)$ and H_{C2}

Chemical addition/doping, like in other practical superconductors is an effective and easy method for modifying the properties of MgB_2. Doping may change the reaction kinetics, grain growth and hence the microstructure. Doping can cause crystalline and microstructural changes, create lattice defects/disorders and cause formation of non superconducting precipitates or inclusions in the superconductor matrix. All these defects can act as flux pinning centers and can increase the H_{C2} and H_{irr} values and hence enhance the in-field J_C of MgB_2. A large number of additives/dopants have been introduced into MgB_2 aimed for the improvement of its superconducting properties. Some of them have negative effects, while most

have positive effect and a few significantly improved the superconducting properties in MgB_2. Though it is not possible to describe all of them, an overview and summary of the effects of chemical addition/doping in MgB_2 is given here.

Various nano/submicron sized particles and materials having quite different physical and chemical properties where introduced into MgB_2. These dopants include metallic elements, carbon (in various forms like nanopowders, nonotubes, graphite and diamond), carbides, silicides, borides, oxides and some hydrocarbons have been introduced into MgB_2 (see the extensive reviews [84, 85, 130–134] and references therein). These dopants improved the flux pinning and $J_C(H)$ of MgB_2 to different extents. The final properties of doped MgB_2 depend on the chemical nature of the dopant and its distribution in the superconductor matrix. Generally carbon based dopants like nano C, SiC, B_4C and some hydrocarbons etc give better J_C and H_{C2} in MgB_2 and nano SiC gives the best perforamnce among the dopants [84, 85, 130–134]. Table 1.4 shows some of the types of dopants introduced on MgB_2.

Table 1.4: Different types of additives/dopants added to MgB_2. Data are taken from [84, 85, 130–133]

Metalic	Metal	Hydrides	Carbon based		
elements	oxides	Nitrides Borides Silicides	C (in different forms)	Carbides	Organic materials
Ti	MgO	Si_3N_4	nano C	SiC	Sugar
Zr	SiO_2	WB	diamond	TiC	Paraffin
Ag	TiO_2	ZrB_2	graphite	WC	Malic acid
Al	Al_2O_3	NbB_2	C nanotubes	B_4C	Maleic anhydride
Fe	Fe_2O_3	TiB_2	Silicon oil	NbC	Toluene
Cu	Co_3O_4	CaB_6	Ca_2CO_3	Mo_2C	Ethanol
Mo	Y_2O_3	WSi_2	Na_2CO_3		Acetone
Co	Ho_2O_3	$ZrSi_2$			Tartaric acid
Ni	Dy_2O_3	Mg_2Si			Ethyltoluene
La	Pr_6O_{11}	ZrH_2			

Of the several metallic and non-metallic elements added into MgB_2 only C and Al entered into the lattice site: C substitutes at the B site and Al substitutes at the Mg sites. C substitution at B site altered the σ and π scat-

tering channels and strongly enhanced the H_{C2} and $J_C(H)$ of MgB_2. The metals Ti and Zr are reported to have some positive effect on the $J_C(H)$ of MgB_2 [135, 136]. Ti is found to be a good grain refiner in MgB_2, which absorbs the impurities (mainly oxides at grain boundaries) and hence improve the grain connectivity [137]. Similar results of grain refining have been observed with the dopants Zr, Ta and CaB_6 [85]. Materials like Mn and Fe are reported to substitute at Mg site, but only at very low concentrations. Being a magnetic material Fe doped as nano Fe reduced the $J_C(H)$ of MgB_2 significantly [138]. While most of the other metals (Cu, Ag, Au, Ni ...) reacted with Mg/B to form intermetallics. These secondary phases reduces the grain connectivity and superconducting volume. So, many of these metallic dopants reduced the $J_C(H)$ than enhancing [60].

As stated earlier C successfully enters into the B site and modifies the electronic and superconducting properties of MgB_2. The substitution of C supplies one additional electron to the B plane, mean while due to the small covalent radii of C compared to B, the substitution locally distorts the lattice. This reduces the T_C with C substitution while enhances the scattering significantly. In MgB_2 the H_{C2} is strongly affected by the scattering and hence C substitution causes the H_{C2} to increase significantly. The lattice strains and distortions due to substitution can act as good flux pinning centers. Both these improve the $J_C(H)$ in C substituted MgB_2 significantly. Today a tyical C substituted MgB_2 tape has a J_C value > of 10^4 A/cm^2 at field 10-12 T and 4.2 K [139, 140], more than one order higher than that of undoped sample. C alloyed MgB_2 fibre showed a high H_{C2} of $\sim$ 55 T at 1.5 K [39] and $\sim$ 70 T is predicted for C doped thin films [82].

A significant breakthrough happened when Dou *et al* reported strong improvement in the $J_C(H)$ by nano SiC addition [141–143]. Nano SiC improves the $J_C(H)$ and H_{C2} of MgB_2 significantly, at all the temperatures, without decreasing the T_C much. Now nano SiC is the best dopant for MgB_2 superconductor which gives consistently high in-field $J_C(H)$ values. In their work Dou *et al* [142] observed that compared to the undoped sample, J_C for the 10 wt% SiC doped sample is higher by a factor of 32 at 5 K and 8 T, 42 at 20 K and 5 T, and 14 at 30 K and 2 T. At 20 K and 2 T, the J_C for the doped sample is 2.43×10^5 A/cm^2, which is comparable to J_C values for the best Ag/Bi-2223 tapes. A typical nano SiC doped MgB_2 conductor has a J_C value higher than 10^4 A/cm^2 at 4.2 K and H_{C2} values of > 33 T are reported for nano SiC doped wires [79]. Matsumoto *et al*

[144] reported a $H_{C2}(0)$ value exceeding 40 T for SiC doped MgB_2 bulk samples, sintered at a temperature as low as 600 °C.

Compared with elemental C addition nano SiC needs only a lower reaction temperature for better C substitution. The doped samples have improved $J_C(H)$ values both at low temperatures and high temperatures, without much reduction in T_C. Even for the 30 wt% of SiC addition T_C of MgB_2 is lowered by only 2.6 K [142], for C doping the T_C falls sharply with C content. The enhancement of J_C(H) in MgB_2 by SiC addition is explained by the dual reaction model [131, 132]. SiC decomposes and reacts with Mg (forms Mg_2Si) for temperatures as low as 650 °C and release fresh C which subsequently substitutes at B site. The C substitution at B site enhances the scattering and hence the H_{C2}. The SiC addition results in a large number of nanometer sized (5-30 nm) dislocations within the MgB_2 grains [141, 142] and these dislocations can strongly pin the flux lines. When SiC reacts with liquid Mg and amorphous B at the reaction temperature, the nanoparticles of SiC will act as nucleation sites to form MgB_2. The other nonsuperconducting reacted phases such as Mg_2Si, BC, $Si_xB_yO_z$ along with unreacted SiC will be incorporated within the grains as inclusions [64, 141, 142]. These highly dispersed reaction-induced products also contribute to the flux pinning [141, 142]. Thus the improvement of both H_{C2} and flux pinning occurs as a result of SiC addition, which consequently enhances the in-field J_C significantly.

Realizing the strong positive influence of C on MgB_2 many groups tried various forms of C based dopants. These include nano carbon, carbon nanotubes (monowalled, double walled and multi walled), graphite and diamond. All these types resulted strong improvement in the H_{C2} and J_C of MgB_2. In many of these dopants including nano C powder, a higher sintering temperature (900-1000 °C) favors better C incorporation into the lattice and better superconducting properties. One main limitation of C substitution is the reduction of T_C and hence a strong improvement of $J_C(H)$ is obtained only in low temperatures (< 10 K). For higher temperatures (> 25 K) the enhancement is not very significant. Using nano C powder, graphite or diamond as a C source, the substitution of C for B cannot be achieved at the same temperature as that of the MgB_2 formation (around 650 °C). Higher sintering temperatures (900-1000 °C) favor better C substitution, but does not favor fine grains (weakens grain boundary pinning) and can cause more MgO formation. Nanosize precursor particles are expensive

and there are always agglomerations of the nano additives. Both these difficulties are reduced using hydrocarbons as the C source.

Now a lot of hydrocarbons including sugar, acetone, benzene, paraffin, toluene, ethanol, sterates, maleic acid etc are tried into MgB_2 with good results [84, 85, 130–133]. The main advantages of carbohydrates are their easy availability and low cost compared to the nano additives. They can be coated on the B powder surfaces with suitable solvent, giving better mixing with reduced agglomeration [145]. Even at lower temperatures carbohydrates melt and release fresh and highly reactive C for the substitution. The main drawback of carbohydrate addition is that most of them contain oxygen, which can easily react with Mg to form MgO which can degrade the grain connectivity and hence the critical current density.

Some silicides ($ZrSi_2$, WSi_2, Mg_2Si), hydrides (ZrH_2), and borides (TiB_2, NbB_2, ZrB_2, WB) are also tried with moderate improvements in flux pinning and critical current density values [84, 85, 130–133]. These dopants are not incorporated into MgB_2 lattice. Si and silicides directly react with Mg. The reaction induced impurities as well as the added particles acts as flux pinning centers. A slight amount MgO in the MgB_2 grains is found to improve the flux pinning properties. Addition of metal oxides like Al_2O_3, Fe_2O_3, Co_3O_4, ZrO_2, TiO_2 and SiO_2 are found to increase the MgO formation. However on the extend of $J_C(H)$ improvement by these metal oxide additions, different works disagree with each other. Some reported decremental effect on $J_C(H)$ by these oxides, while some reported some marginal benefits. The incorporation of nano rare earth (RE) oxides such as Y_2O_3, Ho_2O_3, Dy_2O_3 and Pr_6O_{11} improved the flux pinning in MgB_2 [146–149]. In all these RE oxide additions the RE reacted with B to form their respective borides (YB_4, HoB_4, DyB_4 and PrB_6). For the Y_2O_3 doped sample J_C of $\sim 2 \times 10^5$ A/cm^2 (at 2 T) and H_{irr} of 11.5 T are reported at 4.2 K and for Ho_2O_3 addition J_C of $\sim 1.2 \times 10^5$ are observed at 5 T, 5 K [146, 147].

Based on the performance of J_C(H) due to addition/doping, Dou *et al* [130–132] classified the additives/dopants in MgB_2 into four categories (groups). Table 1.5 summarizes the different categories of dopants and their effects on MgB_2. The first group includes dopants like nano-SiC and carbohydrates which can have both reaction with Mg/B and C substitution. The second group includes materials such as nano-C, CNT and B_4C which

Table 1.5: Classification of different categories of additives added to MgB_2.

Group	Description	Typical additive	Improvement of $J_C(H)$	Main reason for affecting $J_C(H)$
1	C substitution and reaction with Mg/B	nano SiC, carbohydrates	Significant	C substitution[a] and pinning by the reaction induced impurities.
2	C substitution, but no reaction with Mg/B	nano C, CNT	Significant	C substitution.[b]
3	Reaction with Mg/B, but no C substitution	Silicides, Si, RE oxides	Moderate	Pinning by reaction induced impurities.
4	No C substitution and no reaction with Mg/B	BN, MgO	Slight improvement or decrement	Degrading grain connectivity.

[a] C substitution at the same temperature of MgB_2 formation.
[b] C substitution at higher temperature of MgB_2 formation.

can have C substitution without any reaction. The third group includes materials such as Si, Zr, Ti, RE oxides and silicides which can react with Mg/B without any C substitution, and the fourth group includes materials such as BN and MgO which do not have any reaction with Mg/B nor any C substitution. From the first group to the fourth group the enhancement of J_C(H) decreases gradually.

1.10 Objective of the present work

The brief overview presented above highlighted the importance of MgB_2 superconductor for practical applications. In order to exploit its full potential as a conductor it is essential to prepare long multifilamentary conductors in the form of wires, tapes or cables with good mechanical and superconducting properties. The research work presented in the thesis addresses some of the important issues on development of MgB_2 conductors for practical applications. The specific aims of the thesis are:

1. Development of good quality MgB_2 based superconductors in bulk, wire and tape geometries by simple and cost effective methods.

2. Improvement of the in-field critical current density of pristine MgB_2 superconductor by chemical addition.

Powder-In-Tube technique is found to be the most suitable method for the preparation of long length multifilamentary MgB_2 conductors. Several

aspects such as the feasibility of mechanical working (for rolling, drawing etc) and chemical compatibility with Mg and B must be studied for selecting suitable sheath/barrier materials. The quality of the final conductor is influenced by factors like initial packing density, heat treatment temperature and duration, number of filaments, core to sheath area etc. For better superconducting properties these factors must be optimized. For practical applications, superconductors with high in-field critical current density [$J_C(H)$] are required. MgB_2 has a high self-field J_C, however, the J_C falls sharply in applied magnetic fields due to weak flux pinning. Significant research is being continued for the improvement of flux pinning and hence $J_C(H)$, H_{irr} and H_{C2} in MgB_2. Chemical addition/doping is an effective method for introducing flux pinning centers in a superconductor.

In situ PIT technique is used in the present work for preparing MgB_2 conductors. A systematic study on the chemical reactivity of various sheath materials with Mg/B is conducted for selecting the suitable material. After detailed investigations a systematic synthesis procedure is developed for the preparation of MgB_2 conductors using Fe as sheath, Cu as thermal stabilizer and Ni as outer sheath material. A novel, energy efficient and simple electrical self heating method is also developed for the preparation of sheathed MgB_2 conductors.

For improving the in-field $J_C(H)$ of MgB_2 chemical addition with additives of different chemical and physical nature is carried out. A rare earth oxide, Tb_4O_7 is added into MgB_2 first. Tb_4O_7 addition improved the $J_C(H)$ in MgB_2, but the improvement was not drastic. Strong improvement in the $J_C(H)$ of MgB_2 is reported for Carbon based nano materials. Especially, nano-SiC is reported to be one of the most effective additive for enhancing the $J_C(H)$ of MgB_2, by many groups. Based on the strong positive result of nano-SiC and other C based additives/dopants, studies are conducted on introduction of carbon containing additives/dopants into MgB_2. In the present work a novel, inexpensive additive for C source, burned rice husk, is explored and excellent results are obtained. Combined addition of two materials with different chemical and physical properties are also investigated for further increasing the $J_C(H)$.

Chapter 2

Materials and methods

This chapter describes the general preparation and characterization techniques used in the study. Some of the descriptions are brief and will be expanded upon in the relevant chapters of the thesis.

2.1 Preparation techniques

In this study, MgB_2 superconductor was prepared in bulk and wire/tape geometries. Wires/tapes are prepared and studied in mono and multi filamentary configurations. *In situ* preparation method was used for both the bulk and wires/tapes. Powders of Mg from GoodFellow (99.8%) and amorphous B from Merck (99%) are used for the preparations. Various metal/alloy tubes like Fe, Ni, Cu, SS, Monel also used for the present study.

2.1.1 Bulk MgB_2 preparation

MgB_2 bulk superconductors were prepared by a Powder-In-Sealed-Tube (PIST) method. Mg and amorphous B powders were stoichiometrically mixed, mechanically compacted in stainless steel (SS) tubes, ends sealed and heat treated in air at 650-900 °C for different durations. After heat treatment the MgB_2 bulk was recovered by mechanically removing the outer SS tube. Typical dimensions of PIST samples is 3 cm $\times$ 1 cm $\times$ 0.5 cm.

2.1.2 MgB_2 wire and tape preparation

MgB_2 wires and tapes were prepared by Powder-In-Tube (PIT) method. The processing steps are discussed in detail in chapter 4. For monofilamentary wire preparation, homogeneously mixed Mg and B powders were filled in Fe tubes of suitable dimensions and mechanically compacted. These powder filled tubes were then groove rolled to desired dimension. For mono filamentary tapes, the groove rolled wires were then flat rolled to the required dimensions. Photographs of groove and flat rolling machines used for the wire and tape rolling are shown in figure 2.1.

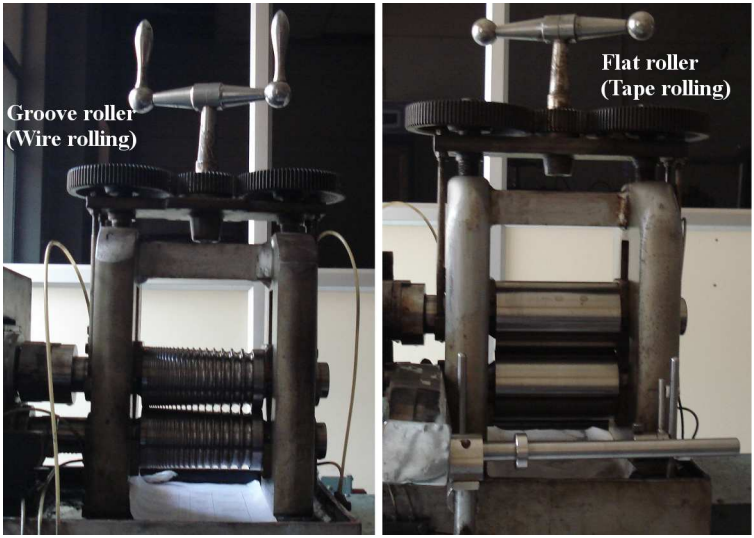

Figure 2.1: Photograph of rolling machines.

For multifilamentary conductors, as rolled mono wires were cut into small pieces and bundled together with Cu rods (stabilizer) and filled in suitable Ni tubes. These composites were then groove rolled for multifilamentary wires, followed by flat rolling for multifilamentary tapes. After rolling the ends of the wires/tapes were sealed by arc welding and then heat treated at 650-750 ^{0}C in air. A wet cloth was wound around the specimens during welding to avoid heating up of the samples. Short length wire samples for various characterizations were then selected by properly cutting out the reaction mixture area of the wire. The maximum length of multi-

filamentary wire prepared so far is about 5 m and the maximum number of filaments in multifilamentary wires is 10. Typical stabilized tape has the dimensions of $\sim$ 1.2 mm thickness and 3-4 mm width.

2.2 Structural characterization techniques

2.2.1 Phase and structural analysis : Powder XRD

X-ray diffraction is a very useful and easy method for the phase identification of crystalline materials. XRD data can be used for a semi-quantitative phase analysis. Besides the phase analysis XRD data gives useful information regarding the crystal lattice parameters, strain, grain size etc.

In the present study powder XRD patterns of samples were taken using a Philips X'pert Pro (Model No: PW 3040/60) X-ray diffractometer with Cu K_α radiation employing X'Celerator and a monochromator at the diffracted beam side. The system has $\theta - 2\theta$ Bragg-Bentano geometry with fully automated operation and data acquisition. Phase identification of the samples was performed using X'Pert Highscore software with support of the ICDD-PDF-2 database. The samples, either bulk or core of wire/tape were ground thoroughly to fine powder. The powder samples were filled in standard holders and the XRD data were recorded at room temperature. For less amount of powder (especially from small wires/tapes) a standard zero back ground holder is used. Appropriate slits were used to restrict the X-ray beam to the sample area. General scans were performed under 40 KV and 30 mA tube Voltage and Current values. Usually the samples were scanned for 21-85° 2θ values with a step size of < 0.02°. The average scan takes about 20 minutes, while some slow scans were also performed in special cases.

The XRD data were analyzed for phase identification and lattice parameter calculations. The volume percentages of different phases in the samples were assessed semi-quantitatively, from the integrated X-ray peak intensities, using the relation

$$\text{Vol.\% of phase X} = \frac{\Sigma \text{ Integrated peak intensities of phase X}}{\Sigma \text{ Integrated peak intensities of all phases}}$$

The d-values of selected peaks of MgB_2 were used for its lattice parameter calculations. Lattice parameters were calculated for the hexagonal crystal structure of space group *p*6/*mmm*, using the relation

$$\frac{1}{d^2} = \frac{4(h^2 + hk + k^2)}{3a^2} + \frac{l^2}{c^2}$$

The FWHM (full width at half maximum) of a XRD peak depends on factors like crystalline size, lattice strain and instrumental parameter etc. The FWHM of selected peaks of MgB_2 were used for qualitatively assessing the lattice strain and grain size.

2.2.2 Microstructural analysis

Optical microscopy

In the present study optical microscopy is mainly used for analyzing the cross sectional features of the wires/tapes. The cross sectional analysis gives informations on the geometry, size, orientation, uniformity of the filaments and the interfaces between core/sheaths for the multifilamentary conductors. For the optical microscopy, samples of small size (1-2 cm) were cut from long conductors, polished mechanically and placed under the microscope in suitable holders. An OLYMPUS SZ-PT model microscope is used for the study and the samples were examined under magnification upto 30 X. Optical microscopy measurements, taken with the help of a scale built into the eyepiece, were used for the exact estimation of core and sheath cross sectional areas of mono/multifilamentary wires/tapes for determining the J_C. Some of the samples for SEM were pre-examined and short listed with the help of optical microscope.

Scanning Electron Microscopy

With greater resolution, higher magnification and large depth of focus Scanning Electron Microscopy (SEM) gives a detailed information of the microstructure of the sample. The SEM scan the sample with high energy electron beam in a raster scan pattern. The scan produces different signals including secondary electrons, back scattered electrons, characteristic X-rays, auger electrons etc, which contain the microstructural information of the sample. In the present study a JEOL JSM 5600LV system equipped with an x-ray energy dispersive spectrometer (EDS) was used for

secondary electron imaging (SEI) microstructural analysis. Typical magnification used was 5000 X or 10000 X, while other magnifications are also used for special cases. In most cases fractured surfaces were used, while polished surfaces were also used for some samples especially for wire/tape cross sectional analysis. The samples were mounted on a metal base using adhesive carbon tapes and loaded into the instrument. No gold coating was used for the superconducting MgB_2 samples.

Transmission Electron Microscopy

Compared with SEM, TEM has a higher magnification and resolution, allowing a more detailed microstructural examination. TEM diffraction patterns can be used to obtain precise structural information. TEM allows lattice scale imaging of the samples. In this study TEM is mainly used to get intra and inter grain features of sub micron or nano sized MgB_2 particles and to determine the morphology, size and content of the nano size dopants. The instrument used was HRTEM FEI-Tecnai G^2 30 S-Twin 300 KV equipped with an X-ray energy dispersive spectrometer (EDS). For the TEM, samples were finely powdered, sonicated in acetone to remove agglomeration, and then placed on copper grids.

Energy Dispersive Spectroscopy

Energy Dispersive Spectroscopy (EDS) allows a semi-quantitative elemental characterization of the samples. In the present study EDS analysis was done using automated EDS system integrated either to SEM or to TEM. The spectrum was taken either for a large area or for a single spot depending on the requirement. The limitation of EDS in the present study was its inability to accurately detect B because of its low atomic weight.

2.3 Superconducting characterization techniques

The superconducting parameters T_C, J_C, $J_C(H)$ and H_{irr} were measured using both transport and magnetic measurements for assessing the quality of samples. For transport measurements an indigenously designed cryostat integrated with an imported cryocooler is used. Figure 2.2 shows the schematic sketch of the cryocooler integrated cryostat. The cryocooler used is a Gifford-McMohan cooler manufactured by Sumititomo Heavy

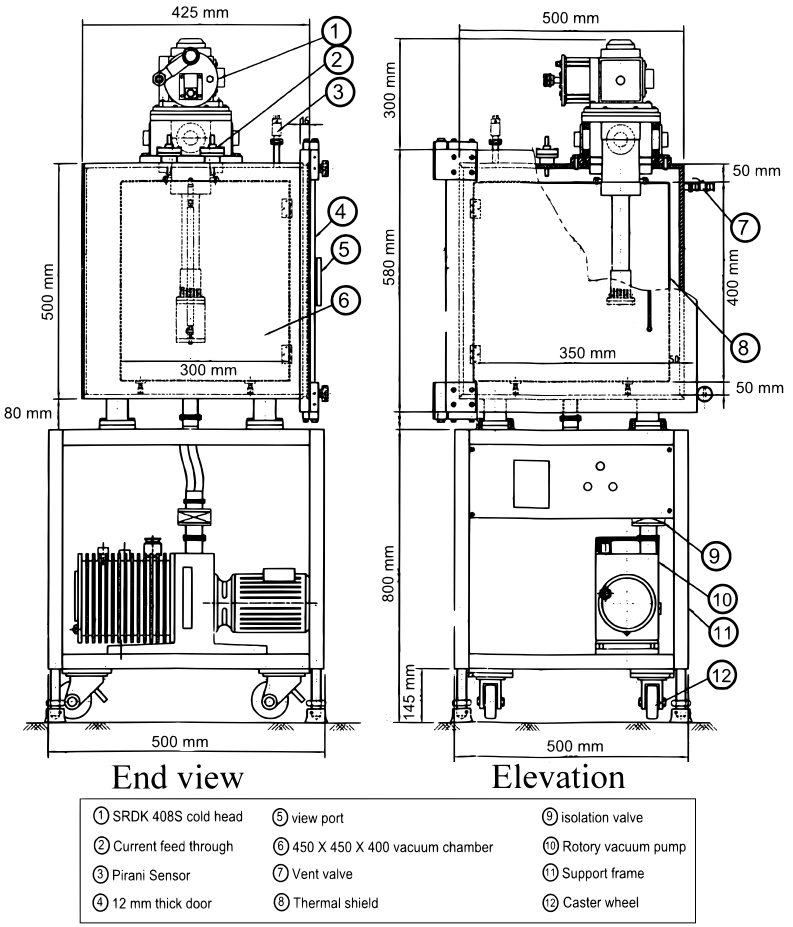

Figure 2.2: Schematic sketch of the cryocooler integrated cryostat.

Industries Ltd. The model number of compressor unit is CSW-71D and the cold head model is SRDK-408. Some of the wires and tapes were measured in liquid helium for transport properties at IPR, Gandhinagar. Magnetic measurements were done using a VSM or SQUID system in PPMS (Quantum Design, USA) with collaboration of RRCAT, Indore and JNCASR, Bangalore. For transport measurements wire/tape samples were used while for magnetic measurements bulk samples were used.

2.3.1 Transport measurements

For transport measurements wires/tapes of 2-3 cm were properly anchored to the second stage of the cryocooler with a home made sample holder. Four probe resistivity method is used for the transport measurements. A schematic diagram of the four probe resistivity measurement arrangement is shown in figure 2.3. High quality insulated copper wires were used for current and voltage terminals. The leads from the terminals were directly soldered to the outer sheath using ortho phosphoric acid as a flux, after thoroughly cleaning the sheath surface with a sharp blade/knife edge.

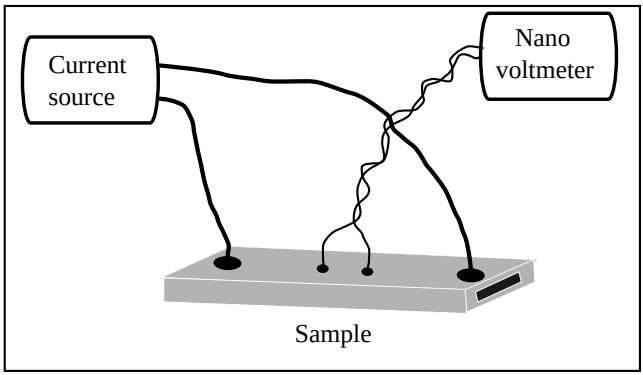

Figure 2.3: Schematic diagram showing the four probe resistivity setup.

Resistance-Temperature (R-T) and Current-Voltage (I-V) characteristics of the samples were measured to determine the T_C and I_C, of the samples. A programmable Keithley 220 current source and Keithley 181/2182A nano voltmeters were used for R-T measurements. A current of 10/100 mA was used for the R-T measurements. For I-V measurements programmable current sources of capacity 30/100/1000 A, manufactured by APLAB were used. All the R-T and I-V measurements were automated and controlled by a PC interfaced with the system through GPIB. Lakeshore L332/L340 model temperature controllers were used for monitoring and controlling the sample temperatures.

The temperature at which resistance falls sharply is taken as the T_C and the difference between the temperatures corresponding to the 90% and

10% of normal state resistivity (T_{C90}-T_{C10}) is defined as ΔT_C for the samples. From the I-V characteristics the current at which the voltage shows a sharp rise is defined as the transport I_C. Ratio of I_C to the total cross sectional area is taken as the engineering critical current density (J_E) and the ratio of I_C to the cross sectional area of MgB_2 core is taken as the critical current density (J_C) for the samples. All the transport measurements (R-T and I-V) were automated using the GPIB interface.

2.3.2 Magnetic measurements

High field magnetic measurements for the present study were done in collaboration with RRCAT, Indore and JNCASR, Bangalore. Bulk samples of typical dimensions 3 mm $\times$ 3 mm $\times$ 1.5 mm were used for the measurements. The measurements were done with magnetic field applied along the longest dimension of the samples. M-T measurements were done at 100 Oe or at 25 Oe mainly in zero field cooling (ZFC) condition. M-H hysteresis loops were measured at 5 K (15 K also for some samples) upto 8 T. T_C of the sample is defined as the temperature at which the ZFC magnetization begin to fall in the M-T curve. ΔT_C is taken as difference between temperatures corresponding to the 90% and 10% of the maximum shielding signal. Magnetic field dependence of the critical current density [$J_C(H)$] of the sample was estimated based on Bean critical state model using the formula

$$J_C(H) = \frac{20 \times \Delta \mathrm{M}}{\mathrm{a}\,(1 - \mathrm{a}/3\mathrm{b})}$$

where ΔM (in emu/cm^3) is the width of M-H loop, a and b (in cm) are dimensions (a $<$ b) perpendicular to the field, for a parallelepiped shaped sample. H_{irr} values of selected samples were estimated as the field at which J_C falls below 100 A cm^{-2}. The values of H_{irr} were estimated from Kramer plot also. For this the function $J_C^{0.5} \times H^{0.25}$ plotted against H and H_{irr} was determined by linear extrapolation to zero of the Kramer curves.

Chapter 3

Preparation and characterization of MgB_2 bulk superconductor

For practical applications, it is required to prepare good quality bulk MgB_2 with high phase purity, and acceptable superconducting properties. There are two main routes to prepare bulk MgB_2 :- reaction of Mg and B sources (*in situ* technique) and the sintering of pre-reacted MgB_2 powders (*ex situ* technique). The *ex situ* prepared samples generally have higher density and better homogeneity compared to the *in situ* samples. However for better superconducting properties, the *ex situ* samples need much higher sintering temperatures compared to the *in situ* samples. Further, doping of impurity elements has limitations in *ex situ* method.

Volatile Mg loss and Mg oxidation are two main hurdles for the *in situ* synthesis of MgB_2. Mg vapor loss at elevated temperature causes non-stoichiometry or B rich phases in the final product, and the MgO that forms at the grain boundaries acts as weak links. This affects the grain connectivity and reduces the critical current density of the superconductor [71]. Several synthesis procedures are reported for the preparation of *in situ* MgB_2 bulks at relatively low temperatures with short durations of heat treatments [87–100]. The starting materials are Mg in powder/flakes/chips/lumps and amorphous/crystalline B in powder forms. In a few reports MgH_2 powder is also used as Mg source [87, 88]. The bulk synthesis is done at

650-1000 °C for 30 min-5 hours heat treatment in vacuum/inert/reducing atmospheres.

We prepared bulk MgB_2 by a method designated herein as Powder-In-Sealed Tube (PIST) method, in which Mg and amorphous B powders were sealed inside stainless steel (SUS 304/SUS 316 L) tubes and heat treated. Stainless steel is chosen for the preparation of MgB_2 since it is non reactive with Mg and B at elevated temperatures and has adequate ductility and strength. The preparation route illustrated here can eliminate Mg evaporation loss and significantly reduce the oxidation of Mg, and reduce the cost of synthesis by avoiding expensive Nb/Ta tubes/foils, inert gases and special furnaces.

Parameters such as the temperature and duration of the heat treatment and the size of starting Mg powder were optimized for obtaining good quality MgB_2 bulk superconductor, in terms of phase purity, crystallinity and superconducting properties.

3.1 Preparation of MgB_2 bulk by Powder-In-Sealed-Tube (PIST) method

3.1.1 Starting materials

Mg powder from GoodFellow (99.8% pure) and amorphous B powder from Aldrich (99.0% pure) were used for the synthesis of *in situ* MgB_2 by the PIST method. Figure 3.1 shows the XRD patterns of starting Mg and B powders. Mg powder has good crystallinity and contained no detectable impurities including MgO. Though the B powder used is amorphous, it showed some small amount of crystalline phases. The observed crystalline phases are B in rhombohedral structure and a minor quantity of B_2O. Figure 3.2 shows the SEM images of Mg and B powders used. B powder is very fine and homogenous in nature. The Mg powder is much bigger compared to the B powder and has irregular size and shape. Commercially available SUS 304/SUS 316 L stainless steel tubes of length 5-10 cm with different outside diameter (OD) and inside diameter (ID) (Typical OD/ID are : 12/10, 10/8, 6/4 : all in mm) were used for the filling of starting powders.

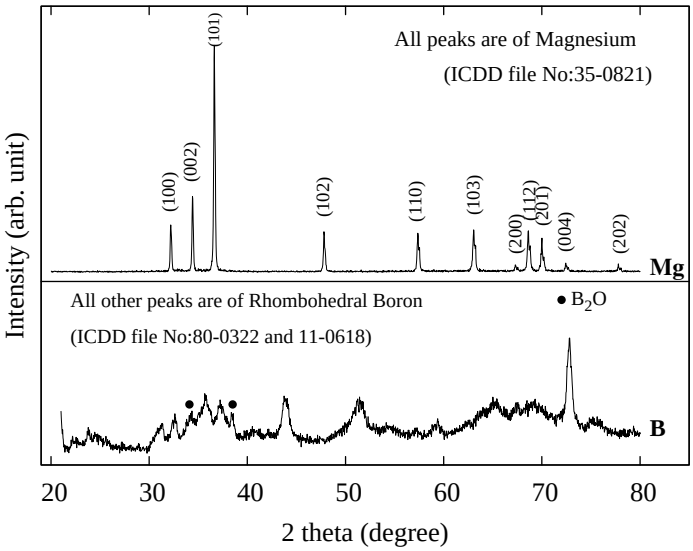

Figure 3.1: XRD pattern of the Mg and B starting powders.

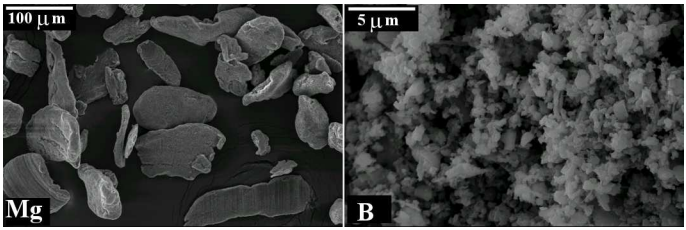

Figure 3.2: Secondary electron SEM image of starting Mg and B powders.

3.1.2 Sample preparation

Stainless steel (SUS 304) tubes of 10 cm long with an outside diameter (OD) of 6 mm and inside diameter (ID) of 4 mm were used for synthesis. One end of the tube was pressed uniaxially at a pressure of $\sim$ 1 GPa using a hydraulic press (HERZOG TP 20P) so that it became tape shaped. Stoichiometric weights of Mg powder and B powder were taken using an electronic balance (Mettler AE240). The powders were mixed, homogenized and ground thoroughly for about 1 hour using an agate mortar and

pestle. Then the powder mixture was densely packed through the open end of the pressed tube leaving some space unfilled. The unfilled portion was pressed with the same pressure that was used for the first end such that both ends are of equal length. Subsequently powder filled middle area was subjected to uniaxial pressing under 1 GPa to get a tape shaped portion. End sealing was performed by arc welding. A wet cloth was wound around the specimen during welding to avoid heating up of the sample.

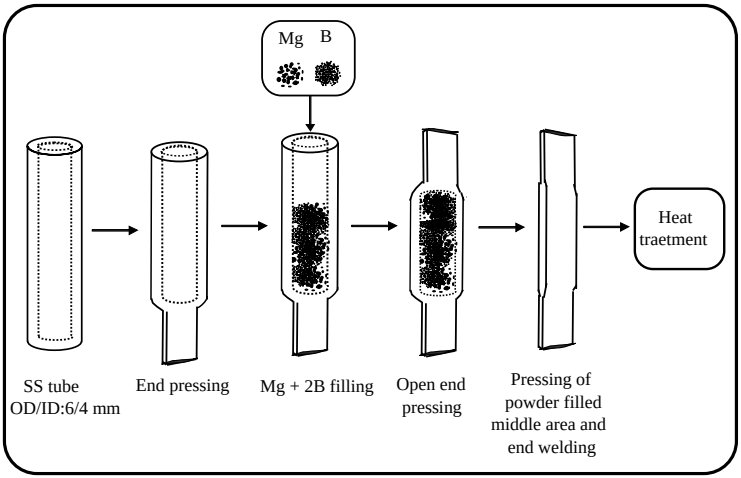

Figure 3.3: Schematic diagram of the preparation procedure in PIST method.

Figure 3.3 shows a schematic diagram of the sample preparation procedure. Figure 3.4 shows the photograph of a typical SS tube used for the filling of the powder and a powder filled sealed sample. Such samples were then heat treated in air at different temperatures and durations (typically 670 °C-900 °C for 0.5-10 hours) in a muffle furnace with a ramp rate of 10 °C/minute and subsequently furnace cooled. After heat treatment the outer SS sheath was mechanically removed and the MgB_2 core was retrieved for characterizations.

3.1.3 Characterizations

The structural and phase analysis of the samples were performed using an X-ray Diffractometer (Philips X'pert Pro) with Cu K_α radiation employ-

ing X'Celerator and monochromator at the diffracted beam side. Phase identification of the samples was performed using X'Pert Highscore Software in support with ICDD-PDF-2 database. Microstructural examination and elemental analysis of the samples were done by using an optical microscope (OLYMPUS SZ-PT), scanning electron microscope (SEM-JEOL JSM 5600LV) and transmission electron microscope (HRTEM FEI-Tecnai G^2 30 S-Twin 300 KV) equipped with an X-ray energy dispersive spectrometer (EDS). DC magnetic measurements (M-T and M-H) were carried out by a vibrating sample magnetometer in Physical Property Measuring System (PPMS), Quantum Design, USA on samples having size 3 mm $\times$ 3 mm $\times$ 1.5 mm. Variation of resistance with temperature (R-T plot) were taken in a heavy duty closed cycle cryocooler-interfaced cryostat (Cold head Model : SHI SRDK-408) using DC four probe method.

Figure 3.4: Photograph of the bare and and powder filled pressed SS tube (L $\sim$ 10 cm, OD/ID = 6/4 mm).

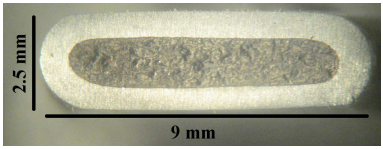

Figure 3.5: Optical photomicrograph of the transverse cross-sectional view of the polished surface of PIST sample after heat treatment.

3.1.4 Structural properties of PIST MgB_2

Figure 3.5 shows the optical micrograph of the cross-sectional view of the polished surface of SS sheathed MgB_2 processed at 850 °C for 2 hours. The core layer is observed to be dense and black. The interface region

between MgB_2 core and SS tube is sharp and distinct and there is no sign of any interfacial reaction occurring between the core and the sheath at this temperature.

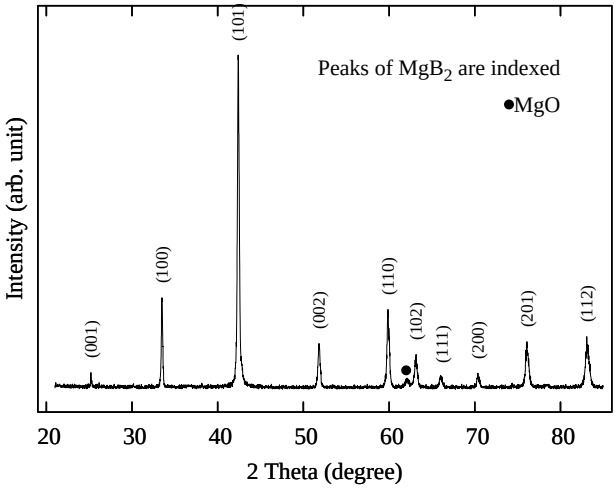

Figure 3.6: Powder XRD pattern of PIST MgB_2.

Figure 3.6 shows a typical XRD spectrum of the MgB_2 core heat treated at 850 °C for 2 hours. Crystalline MgB_2 is the main phase with only a trace of MgO as the impurity phase. The sharp peaks of MgB_2 is indexed to the hexagonal crystal structure of ICDD file number 38-1369. The very small amount of MgO observed is due to the air entrapped inside the tube before sealing the ends. No boron rich phases such as MgB_4 or MgB_7 are observed which ensures complete suppression of Mg evaporation loss during the heat treatment.

The lattice constants of the prepared MgB_2 phase were determined from the XRD data, considering the hexagonal crystal structure and the values are a = 3.0862 Å, c = 3.5260 Å, consistent with reported values for MgB_2 [11, 21]. The geometric density of the bulk MgB_2 was determined by measuring the mass and dimensions of rectangular shaped pieces cut from the MgB_2 core. The PIST samples have high level of porosity and hence have a low average density of $\sim$ 1.3 g/cc ($\sim$ 50% of the theoretical density).

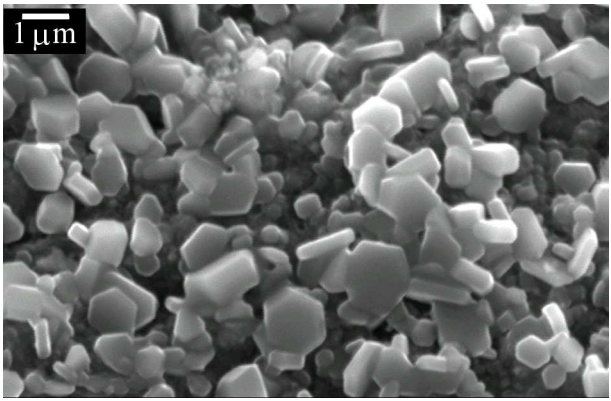

Figure 3.7: Secondary electron SEM image of PIST MgB_2.

Figure 3.7 shows a typical secondary electron SEM image of the fractured surface of PIST MgB_2 heat treated at 850 °C. The microstructure of the sample is homogeneous in nature. The sample show fine faceted hexagonal and randomly oriented MgB_2 grains of varying sizes. The grains have size varying around 1 μm. The EDS analysis of a typical sample is shown in figure 3.8. The EDS shows presence of Mg, B and traces of O in the grains, which is in agreement with the XRD results.

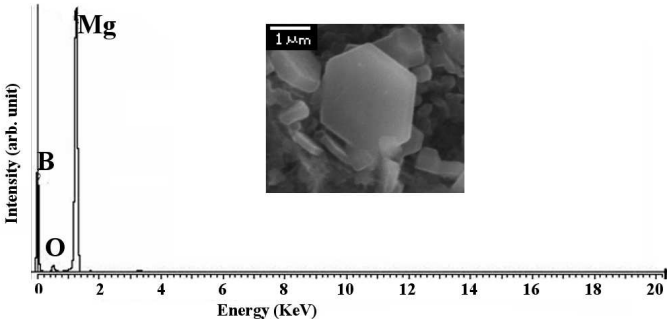

Figure 3.8: EDS spectrum of typical PIST MgB_2. Inset of the figure shows the hexagonal MgB_2 grain.

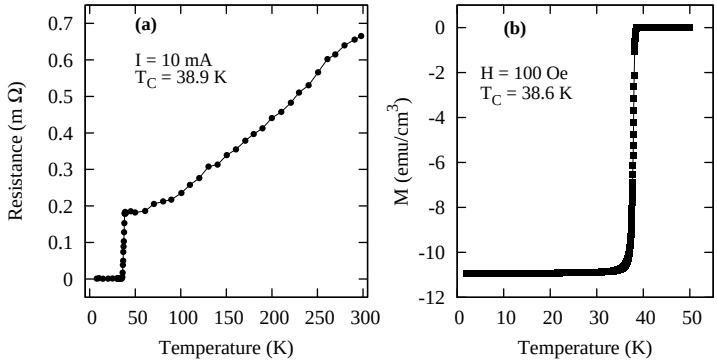

Figure 3.9: Temperature dependence of (a) resistance (R-T) and (b) magnetization (M-T) curves of PIST MgB_2.

3.1.5 Superconducting properties of PIST MgB_2

Both transport and magnetic measurements show sharp superconducting transition with T_C = 38-39 K and ΔT_C < 1 K for the PIST MgB_2. Figure 3.9 (a) shows the temperature dependency of resistance (R-T plot) in the temperature range 8-300 K, of a typical bulk MgB_2 measured using a closed cycle cryocooler. The MgB_2 shows superconducting transition at 38.9 K. Zero field cooled (ZFC) magnetization plot in the temperature range 2 to 50 K, taken at 100 Oe is shown in figure 3.9 (b). The sample show sharp superconducting transition with T_C around 38.6 K and ΔT_C < 1 K. The consistently high T_C and small ΔT_C values show that the sample has excellent crystallinity and good homogeneity.

The field dependent magnetization (M-H plot) of a typical PIST MgB_2 sample is shown in figure 3.10. Thermo-magnetic flux jumps are observed for fields below 2 T for the sample without any dopants at 5 K, as observed in many previous reports [60, 150–152]. The flux jump occurs only under conditions of extremely high critical currents, high magnetic diffusivity and low heat capacity causing localized motion of magnetic flux. In MgB_2, since the magnetic diffusivity into the sample is much larger than the thermal one, flux jump is considered as a process of magnetic diffusion. The temperature of the sample increases during flux jump and the sample may transit from superconducting state to normal sate. Flux jump is more at lower temperatures. At 15 K no flux jump is observed.

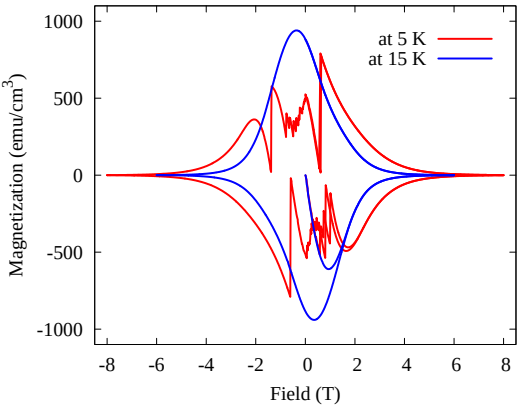

Figure 3.10: M-H plot of a typical PIST MgB_2.

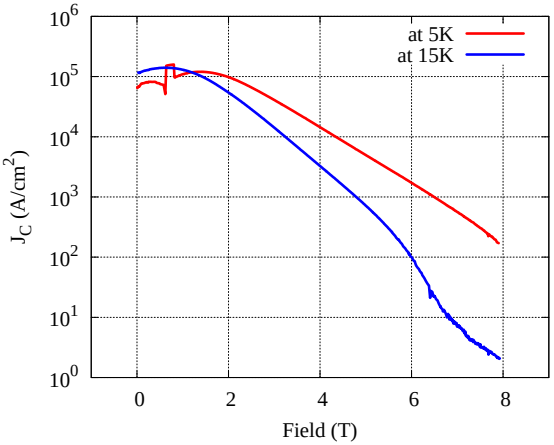

Figure 3.11: Magnetic $J_C(H)$ characteristics of typical PIST MgB_2.

Figure 3.11 shows the field dependence of a magnetic critical current density [$J_C(H)$] of typical PIST MgB_2 sample at 5 K and 15 K, deduced from M-H data. The $J_C(H)$ is estimated based on Bean critical state model using the formula. At 5 K, at lower fields the estimation of J_C is not accurate due to flux jumps. At 5 K the magnetic J_C is $\sim 10^5$ A/cm^2 at 2 T and $\sim 0.8 \times 10^4$ A/cm^2 at 5 T. At 15 K the J_C is $\sim 6 \times 10^4$ A/cm^2 at 2 T

and $\sim 5 \times 10^3$ A/cm^2 at 5 T. The H_{irr} of the sample, defined as the field at which J_C falls below 100 A/cm^2 is higher than 8 T at 5 K and is ~ 6 T at 15 K. All these values are comparable with many of the good quality MgB_2 bulks reported worldwide. Table 3.1 summarizes the properties of bulk MgB_2 prepared by PIST method.

Table 3.1: Features of PIST method.

Main advantages	No vacuum or inert atmosphere needed and reduced Mg oxidation and vapor loss
Starting materials	Mg and B in powder form
Filling tube	SS 304/SS 316 L
Sealing	By arc welding
Heat treatment	800-850 °C in air
Impurities in the final samples	Only traces of MgO
Average MgB_2 grain size	1 μm
T_C	38-39 K
J_C	> 10^5 A/cm^2 at 2 T, 5 K > 10^4 A/cm^2 at 2 T, 15 K and > 10^3 A/cm^2 at 5 T, 15 K
H_{irr}	> 8 T at 5 K, $\sim$ 6 T at 15 K
F_{Pmax}*	1-2 GN/m^3 at 5-15 K

* F_{Pmax} is the maximum flux pinning force density.

3.2 Optimization of preparation conditions

For *in situ* synthesized MgB_2, the $J_C(H)$, H_{irr} and H_{C2} depends sensitively on factors like chemical composition, homogeneity, density, microstructure, grain connectivity and flux pinning of the sample. These factors are influenced by the process conditions, as well as the purity, size and nature of starting raw powders [83, 92, 93, 153–157].

For the *in situ* MgB_2 bulk, based on the synthesis method and nature of starting materials many reported heat treatment at 700-850 °C for 30 min-5 hours for optimized superconducting properties. A low synthesis temperature/duration favors fine sized grains, enhancing grain boundary pinning, at the cost of incomplete reaction, reduced crystallinity and or low lattice substitution (for the case of doping). Higher synthesis temperature/duration causes grain growth, improves crystallinity and level of substitution at the expense of low grain boundary pinning and increased MgO formation. So an optimum preparation condition has to be needed for detailed studies.

3.2.1 Effect of heat treatment conditions on structural properties

Samples heat treated in air at 700 °C, 800 °C, and 900 °C for 1, 2, 5 and 10 hours were prepared by *in situ* PIST method. Crystalline and microstructural characterization of the samples are done using XRD and SEM studies.

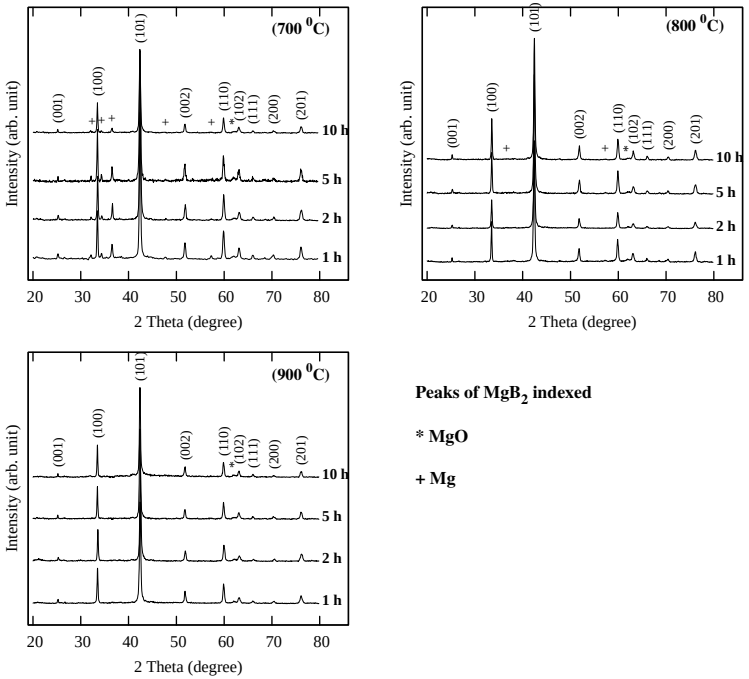

Figure 3.12: Powder XRD patterns of the samples heat treated at 700 °C, 800 °C and 900 °C for 1, 2, 5 and 10 hours.

Powder XRD patterns of the samples heat treated at 700 °C, 800 °C, and 900 °C for 1-10 hours are shown in figure 3.12. Crystalline MgB_2 is the major phase observed in all the samples, with traces of MgO. Unreacted Mg is observed in some samples heat treated at 700 °C and 800 °C for lower sintering durations. The amount of unreacted Mg decreases and crystalline MgB_2 increases with increasing heat treatment durations.

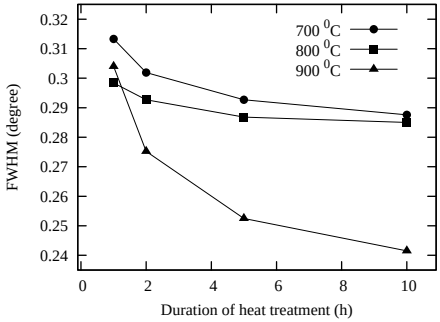

Figure 3.13: FWHM of (101) peak of the samples heat treated at 700 °C, 800 °C and 900 °C for 1, 2, 5 and 10 hours.

Figure 3.13 shows the full width at half maximum (FWHM) of (101) peaks of the samples. The figure clearly shows that the FWHM decreases with increase in the temperature of synthesize. The FWHM decreases more sensitively with increase in the duration of heating. The decrease in FWHM is more for samples heated at 900 °C. The decrease in the FWHM indicates the increase in the MgB_2 grain size, with increase in heating temperature and duration.

Table 3.2: Lattice parameters of the samples, calculated from XRD data

	Heat treatment temperature (°C)					
Heat treatment	700		800		900	
Duration (h)	*a* (Å)	*c* (Å)	*a* (Å)	*c* (Å)	*a* (Å)	*c* (Å)
1	3.085	3.526	3.088	3.534	3.088	3.522
2	3.086	3.525	3.088	3.522	3.089	3.519
5	3.084	3.526	3.086	3.523	3.089	3.532
10	3.086	3.524	3.086	3.529	3.086	3.522

Table 3.2 shows the lattice parameters *a* and *c* of the samples, calculated from the XRD data. The lattice parameters of the samples show no significant variations within the experimental error.

Figure 3.14 shows the secondary electron SEM images of the samples heat treated at 700 °C, 800 °C and 900 °C for 1 and 10 hours. The mi-

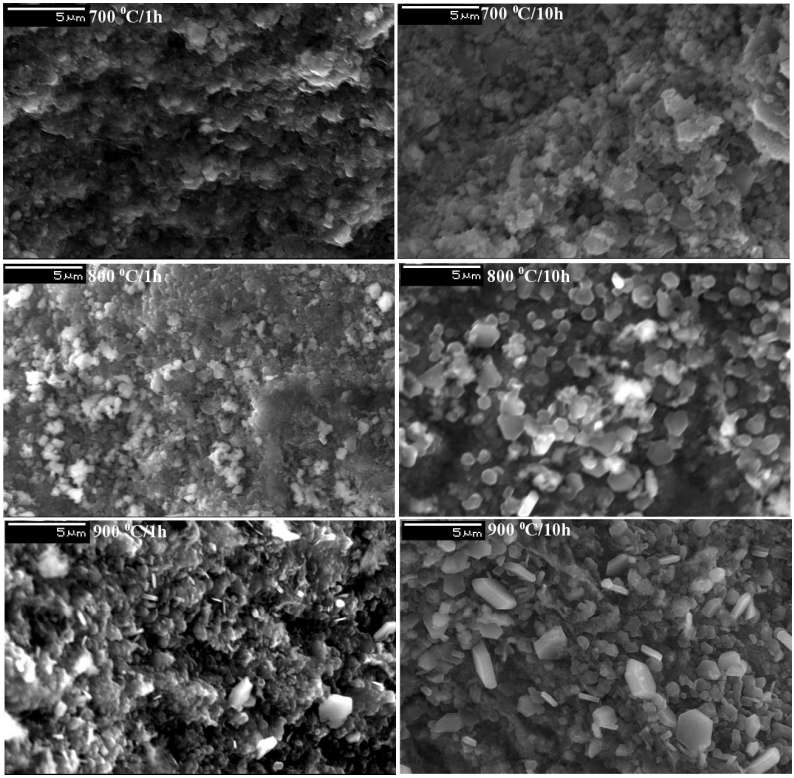

Figure 3.14: Secondary electron SEM images of the samples heat treated at 700 °C, 800 °C and 900 °C for 1 and 10 hours.

crostructure of all the samples is homogeneous in nature. The samples show fine hexagonal MgB_2 grains of varying sizes. SEM images show that the average grain size and grain connectivity of the samples are improved with increase in sintering temperature. The grain size also improves with the sintering duration, for each sintering temperature. The information from the SEM images are in good agreement with the FWHM of the samples shown in figure 3.13.

The results indicate that both the sintering temperature and duration of sintering have influence on the crystalline and microstructural properties of *in situ* polycrystalline MgB_2. As the sintering temperature and its duration

increase the amount of crystalline MgB_2 increases. The average grain size of crystalline MgB_2 increases with increasing the sintering temperature and durations.

3.2.2 Effect of heat treatment temperature on the superconducting properties

Based on the above results on the crystalline and microstructural properties, four samples were prepared for superconducting measurements. The samples were heat treated at 750 °C, 800 °C, 850 °C, and 900 °C for 2 hours. The samples were named as MB750, MB800, MB850 and MB900 respectively.

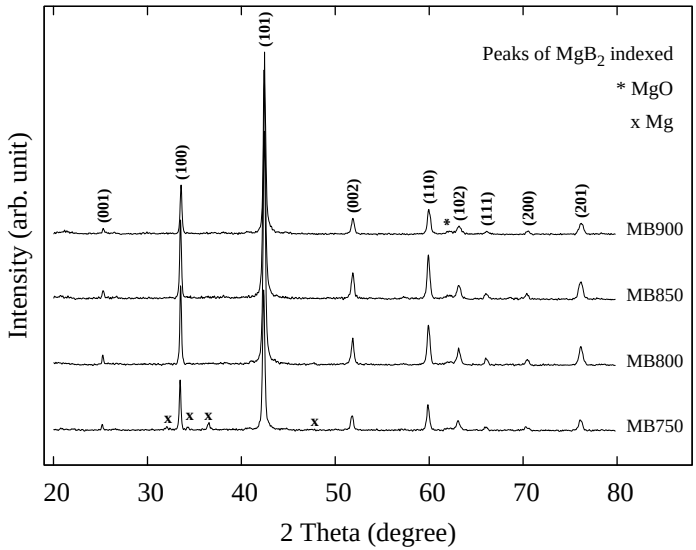

Figure 3.15: Powder XRD patterns of the samples heat treated at 750 °C, 800 °C , 850 °C and 900 °C for 2 hours.

Powder XRD patterns of the samples are shown in figure 3.15. MgB_2 is the main phase and small amount of MgO is observed in all the samples. Small amount of unreacted residual Mg is detected for the sample

heat treated at 750 °C. No peaks of MgB_4 or other higher borides are observed in any of the samples. The very small quantity of MgO observed is due to the entrapped air before end-sealing of the tubes. Table 3.3 shows the lattice parameters *a*, *c* axes, unit cell volume and the full width at half maximum (FWHM) of the (110) and (002) peaks of the samples. FWHM of both the peaks decreases significantly with increasing sintering temperature, indicating increase in MgB_2 grain size with sintering temperature.

Table 3.3: Lattice parameters and FWHM of the samples, calculated from XRD data

Sample	*a*	*c*	Cell volume	FWHM (degree) of peaks	
	(Å)	(Å)	($Å^3$)	(002)	(110)
MB750	3.086	3.524	29.070	0.328	0.327
MB800	3.088	3.521	29.073	0.306	0.317
MB850	3.087	3.523	29.081	0.286	0.308
MB900	3.090	3.519	29.089	0.256	0.237

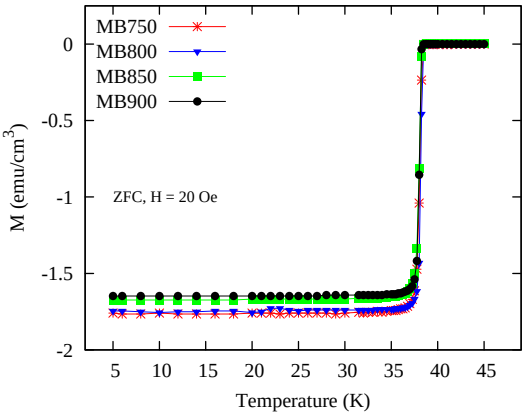

Figure 3.16: M-T plots of the samples heat treated at 750 °C, 800 °C , 850 °C and 900 °C for 2 hours.

Temperature dependence of magnetization (M-T) at 20 Oe of the samples is shown in figure 3.16. All the samples show sharp superconducting transition with T_C around 38.5 K and $\Delta T_C \sim 0.8$ K. The almost identical

T_C and ΔT_C values indicate that the samples are identical with respect to stoichiometry, lattice or structural defects and the electronic states in the superconducting B planes.

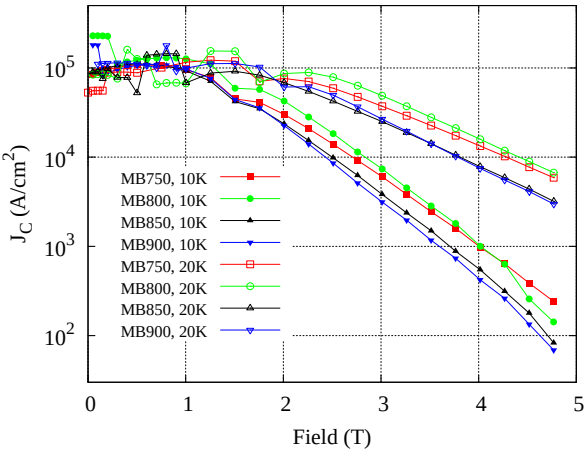

Figure 3.17: $J_C(H)$ plots of the samples heat treated at 750 °C, 800 °C , 850 °C and 900 °C for 2 hours.

The in-field critical current density [$J_C(H)$] at 10 K and 20 K, estimated from the M-H curves is shown in figure 3.17. At 10 K, and at low fields J_C jumps abruptly due to the flux jumps. But at higher fields the $J_C(H)$ follows systematic behavior for all the samples. Sample heat treated at 800 °C shows higher J_C in external fields, at both 10 K and 20 K. In general, the $J_C(H)$ is better for samples heat treated at low sintering temperatures (750 °C and 800 °C), while it is lower for samples heat treated at relatively higher temperatures (850 °C and 900 °C). The slightly higher $J_C(H)$ of the samples MB750 and MB800 is mainly due to the smaller grains.

Thus the critical temperature of the MgB_2 remains almost same for samples prepared at different temperatures, while $J_C(H)$ is slightly higher for samples prepared at relatively lower temperatures.

3.2.3 Effect of Mg particle size

In this section the role of Mg particle size on the reactivity of Mg with B was studied. The samples were synthesized using Mg particles of four different size categories. The superconducting properties of selected samples were evaluated for finding an optimum Mg particle size.

Effect on reaction between Mg and B

At first two sets of samples-one set with Mg particle size 25-53 μm (+500 to -300 mesh) and other 106-180 μm (+150 to -85 mesh)- were prepared. For all the samples B powder used was of size < 44 μm (-325 mesh). The two sets of the samples were prepared at 700, 800, 850 and 900 °C for 2 and 10 hours. The samples were then characterized using powder XRD analysis. The samples prepared using smaller and larger Mg particles were named as MB S and MB L respectively.

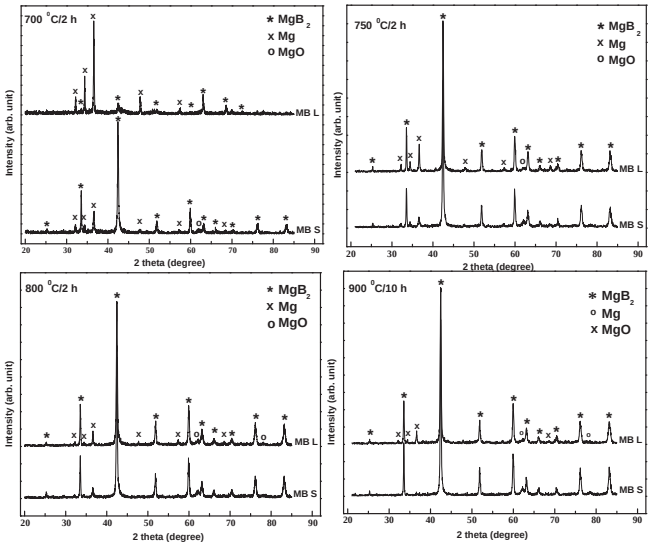

Figure 3.18: Powder XRD patterns of MB S and MB L heated at different temperatures and durations.

Powder XRD patterns of the samples MB S (Mg size: 25-53 μm) and MB L (Mg size: 106-180 μm) at different heat treatment temperatures (700-900 °C) and durations (2 and 10 hours) are shown in figure 3.18. Quantitative data of various phases formed (MgB_2, MgO and remnant Mg) are shown in table 3.4. MgB_2 is the main phase and small amounts of MgO and remnant Mg are observed for MB S. However, for MB L, remnant Mg is much higher and the amount of MgB_2 is lower compared to MB S. Most importantly, at 700 °C /2 h, the amount of MgB_2 is very low and the remnant Mg is high for MB L.

Table 3.4: Volume percentage of MgB_2 , MgO and Mg in MB S and MB L heat treated at different temperatures and durations.

Heat	Volume percentage of (%)					
treatment	MgB_2		MgO		Mg	
	MB S	MB L	MB S	MB L	MB S	MB L
700 °C/2h	82.01	14.67	0.42	0.00	17.57	85.33
750 °C/2h	91.11	84.20	2.15	0.89	6.74	14.91
800 °C/2h	93.13	90.53	2.25	2.11	4.62	7.36
850 °C/2h	97.46	93.44	2.54	1.16	0.00	5.40

To find the more usable Mg particle size for better superconducting properties four more samples were prepared with different Mg particle sizes. The Mg particles sizes used were < 25 μm, 25-53 μm, 53-106 μm and 106-180 μm. The samples were heat treated at 850 °C for 2 hours. The samples were named as MB1 (Mg size: < 25 μm), MB2 (Mg size: 25-53 μm), MB3 (Mg size: 53-106 μm) and MB4 (Mg size: 106-180 μm) respectively. Powder XRD patterns of the samples are shown in figure 3.19. Residual Mg is detected for all samples except MB1 and its amount increases significantly with increase in the starting Mg particle size. No peaks of MgB_4 or other higher borides are observed in any of the samples. There may be unreacted amorphous B, but cannot be detected in XRD. The very small quantity of MgO observed is due to the entrapped air before end-sealing of the tubes. The starting Mg powders were free from oxygen as their XRD patterns showed no MgO within the detection limit.

Quantitative phase analysis of the samples is shown in table 3.5. From the table it is clear that both MgB_2 and MgO are higher for samples synthesized from smaller sized Mg powders (MB1 and MB2). As the particle

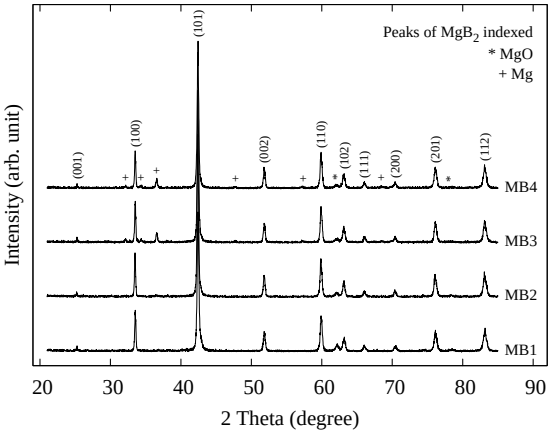

Figure 3.19: Powder XRD patterns of the samples MB1, MB2, MB3 and MB4 heated at 850 °C/2h.

size of starting Mg powder increases, both MgB_2 and MgO decrease and the residual Mg increases (MB3 and MB4). For MB1 and MB2 the initial Mg particle size (< 25 μm for MB1 and 25-53 μm for MB2) is comparable with that of B (< 44 μm). For MB3 and MB4 the initial Mg particle size (53-106 μm for MB3 and 106-180 μm for MB4) is significantly higher compared to the B powder. This clearly shows that the amount of residual Mg increases significantly as the Mg particle size increases above the B particle size.

Table 3.5: Volume percentage of MgB_2 , MgO and Mg in MB1, MB2, MB3 and MB4 heat treated at 850 °C /2h.

	Volume percentage of (%)		
Sample	MgB_2	MgO	Mg
MB1	97.40	2.60	0.00
MB2	98.04	1.44	0.52
MB3	93.83	1.12	5.05
MB4	93.08	1.04	5.87

Figure 3.20 shows the secondary electron SEM images of the samples. The samples show distinct difference in microstructure with respect to Mg

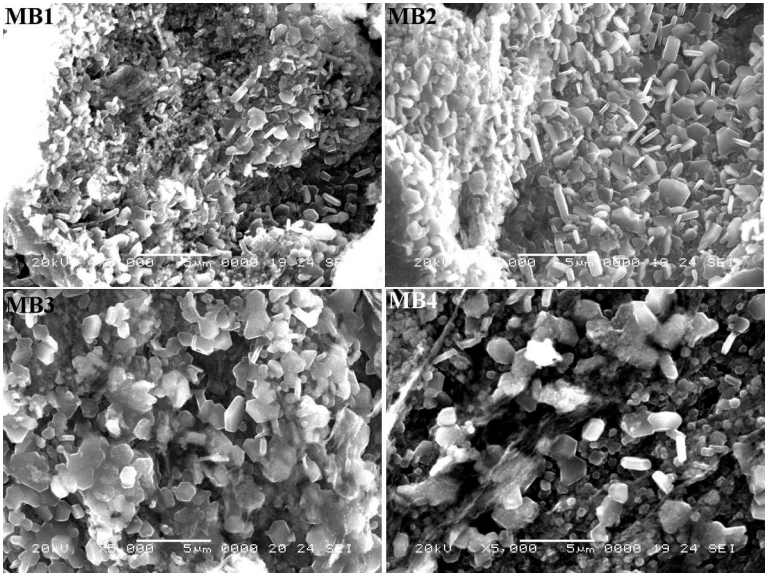

Figure 3.20: SEM images of MB1, MB2, MB3 and MB4 heated at 850 °C/2h.

particle size. Samples MB1 and MB2 show homogeneous microstructures with randomly oriented hexagonal MgB_2 grains of varying size. The grains are densely packed and the average grain size is around 1 μm. All the grains are well connected and sharp grain boundaries can be seen for higher sized grains. But for MB3 and MB4 the microstructure is less homogeneous with larger grain size compared with those of MB1 or MB2, and contain significant amount of amorphous like regions. In MB3 and MB4 hexagonal grains of different sizes are loosely packed and the grains are not well connected as those of MB1 and MB2. Some of the hexagonal grains of MB4 have notably high grain sizes. A significant portion of the MB4 contains amorphous like (or less crystallized) regions.

The full width at half maximum (FWHM) of (101), (002) and (110) peaks for the samples is shown in figure 3.21, which clearly indicates higher FWHM for MB1, implying reduced MgB_2 grain size in this sample, in accordance with the SEM images.

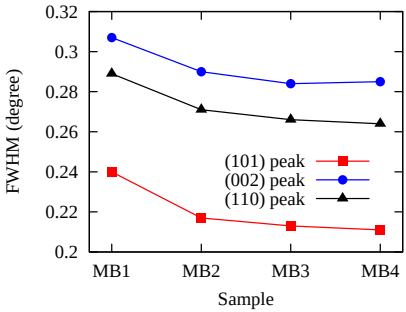

Figure 3.21: FWHM of (101), (002) and (110) peak of the samples.

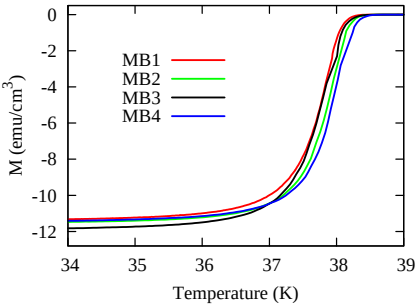

Figure 3.22: M-T plots of MB1, MB2, MB3 and MB4 heated at 850 °C/2h.

Effect on the superconducting properties of MgB_2

In order to study the influence of Mg particle size on the superconducting properties of MgB_2 with Mg particle size the samples MB1, MB2, MB3 and MB4 further characterized using DC magnetization measurements. Temperature dependence of magnetization (M-T) of the samples is shown in figure 3.22. All the samples show sharp superconducting transition with T_C in the range 38.4-38.6 K and ΔT_C ($T_{C90\%}$-$T_{C10\%}$) $\sim$ 1.1-1.2 K. The almost identical T_C and ΔT_C values of the samples indicate that unreacted Mg or B do not cause any significant change in the superconducting transition temperature of MgB_2. This is consistent with the earlier studies on the Mg_xB_2 samples, in which T_C was found to be nearly constant, with a spread of only 0.3 K for $0.6 < x < 1.3$ [93, 158].

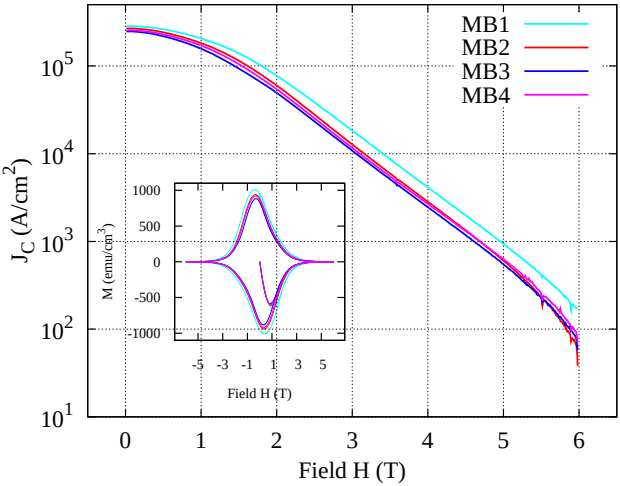

Figure 3.23: Magnetic $J_C(H)$ plots at 15 K for the samples MB1, MB2, MB3 and MB4 heated at 850 °C/2h. Inset of the figure shows the corresponding M-H curves of the samples at 15 K.

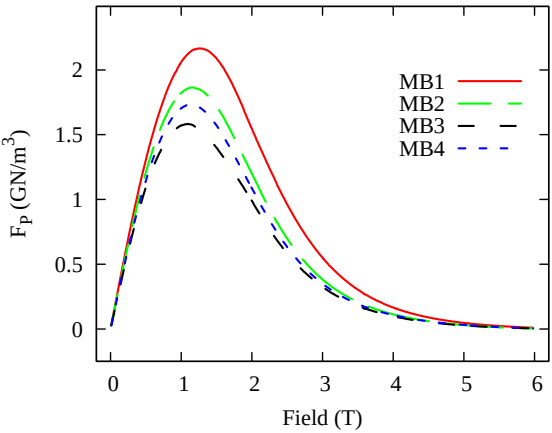

Figure 3.24: Field dependence of flux pinning force density for the samples MB1, MB2, MB3 and MB4

Figure 3.23 shows the J_C at 15 K in applied fields, estimated from the isothermal M-H curves by using the Bean model. Inset of the figure shows the corresponding M-H curves at 15 K for the samples. The sample MB1 has the best J_C value among all the samples upto the maximum field (6 T) studied. At high fields the J_C of MB2, MB3 and MB4 are comparable but distinctly lower than that of MB1.

The flux pinning force density F_P ($F_P = J_C \times B$) as a function of applied field for the samples is shown in figure 3.24. The sample MB1 clearly show enhanced flux pinning compared to the others. The flux pinning behaviour of all other samples is almost same. For the sample MB1 both F_{Pmax} and the field for F_{Pmax} are higher, implying increased number and strength of pinning centers in the sample.

3.2.4 Discussion of the results

The results of above studies indicates :

1. As the sintering temperature and its duration increase the amount of crystalline MgB_2 increases.

2. The average grain size of crystalline MgB_2 increases with increasing the sintering temperature and durations.

3. The critical temperature of the MgB_2 remains almost same for samples prepared at different temperatures, while $J_C(H)$ is slightly higher for samples prepared at relatively lower temperatures.

4. The reactivity of Mg with B is better for smaller sized Mg particles. A considerable amount of Mg left unreacted in samples prepared from larger sized Mg powders.

5. The critical temperature of MgB_2 is almost unaffected by the Mg size variation, but the critical current density is affected. $J_C(H)$ and flux pinning strength were higher for samples synthesized with lower sized Mg particles and lower for samples synthesized with higher sized Mg particles.

The observed results can be explained as follows. The reaction mixture is considered as a homogeneous mixture of Mg and B powders. Mg melts at $\sim$ 650 °C and the melting temperature of B is higher than 2000 °C.

Detailed kinetic analysis for the Mg + B system shows that MgB_2 phase starts to form much below the melting of Mg (< 650 °C) [159–161]. At these temperatures, solid-solid diffusion of Mg and B particles takes place and the MgB_2 phase starts to form at a slow rate. The reaction between Mg and B powders starts at the Mg-B interface and a layer of MgB_2 forms at the interface [159–161]. Once the temperature reaches the melting point of Mg (∼ 650 °C), Mg melts and then liquid-solid reaction takes place, through diffusion. At the reaction temperature Mg melts but remains as globules and can be considered as particles in liquid phase. The formation of MgB_2 generates heat, further promotes the melting and reaction of Mg with B. The reaction between Mg and B starts at Mg-B interface and the particles diffuse further across the formed MgB_2 layer, and the reaction grows around the layer [159–161], until the growth is pinned (mainly by pores). The rate of diffusion depends on the temperature and more particles diffuse with increased sintering temperature and durations.

At lower temperatures and durations the rate of diffusion is low and is the reason for the observed unreacted Mg in these samples sintered at lower temperatures and durations. At much higher temperatures the vapor pressure of Mg is high and a great deal of liquid Mg turns into Mg vapor, leading to a vapor-solid interaction. At higher sintering temperatures the diffusion rate is higher which improves the grain growth, resulting MgB_2 crystals of increased grain sizes.

As the MgB_2 grain grows at the Mg-B interface, diffusion rate decreases with increase in the thickness of the interfacial MgB_2 layer. The reaction kinetics of *in situ* MgB_2 discussed by Cui *et al* [162] also suggests that the rate of reaction is most likely to be inversely proportional to the thickness of the MgB_2 layer formed between the reactants. For Mg particles of size smaller or comparable with B, the Mg-B interface will be sufficient to diffuse and react the Mg and B particles completely. For Mg particles of size much higher compared to B particles, some Mg will remain unreacted and this will be trapped inside the MgB_2 layers as inclusions since all the Mg inside may not diffuse as the diffusion rate decreases with growth of interfacial MgB_2. Thus the reaction between Mg and B practically ceases locally after a certain period since diffusion rate approaches zero. In the SEM images of samples (figure 3.20) synthesized with higher sized Mg powders a lot of separated (not well connected) MgB_2 grains can be seen. This may be due to the ceasing of local grain growth. But in samples synthesized with smaller sized Mg powders, the grains are comparably well

connected and the microstructure is more homogeneous. As no MgB_4 or other higher borides are detected in the samples, due to the incomplete reaction, small quantity of B can be at the grain boundaries as an amorphous impurity. For smaller starting Mg powders the MgB_2 grains formed will be also small, since Mg is the nucleation site and the reaction grows along the Mg-B interface. SEM images of the samples show that the grain size is lower for samples synthesized from smaller sized Mg powders, which is further supported by the FWHM results.

Grain boundaries are good flux pinning centers in MgB_2 [61, 122–124] and flux pinning improves with reduced grain size [125]. This is why samples with lower sized grains showed higher $J_C(H)$ values.

3.3 Summary and conclusion

Bulk MgB_2 superconductor was prepared by a simple a Powder-In-Sealed Tube (PIST) method. In this method, Mg and B powders were sealed inside stainless steel tubes and heat treated in air, ie without any inert or vacuum atmosphere. The MgB_2 prepared by PIST method has good phase purity and superconducting properties. Only a trace amount of MgO is observed as an impurity in typical PIST sample and the sample has T_C 38-39 K with a $\Delta T_C \sim 1$ K and J_C of 10^5-10^6 A/cm^2 at 5 K.

Influence of heat treatment temperature, duration and size of starting Mg powder on the microstructural and superconducting properties of *in situ* MgB_2 were studied for optimizing the preparation conditions. Reactivity of Mg with B decreases significantly due to the reduction in diffusion of particles across MgB_2 layer and the residual Mg increases with increase in the size of the starting Mg powder. MgB_2 prepared using Mg powder of size smaller or comparable with B powder has no/lesser residual Mg, and show better J_C in applied fields compared to other samples. Based of the phase analysis, crystalline and microstructure analyses and evaluation of superconducting properties, a sintering temperature of 800-850 °C for 2 hours is found to be the optimum for PIST method. Considering the availability and the observed good results Mg particles of size 25-53 μm is selected for the further studies in the present work.

Chapter 4

Preparation and characterization of MgB_2 wires and tapes

This chapter describes the preparation and characterization of MgB_2 superconductor in mono and multifilamentary wire and tape geometries. Over the years many techniques were developed for making LTS and HTS materials into wires and tapes. Of these, Powder-In-Tube (PIT) method is an easy and scalable method for large scale production of long length conductors. For MgB_2 also PIT is the most preferred for long length fabrication. In the present study also chose *in situ* PIT method for the preparation of MgB_2 wires and tapes as the method is most efficient for large scale industrial production of long length conductors.

In PIT method, the precursor powder is filled into suitable metallic tubes, mechanically rolled/extruded/drawn into desired size and shape followed by a heat treatment. In the case of MgB_2, the metallic sheath chosen must be chemically compatible with MgB_2 and should not degrade the superconductivity. It must be non-reactive with Mg, B and MgB_2. The sheath metal must have adequate strength to give mechanical support to the brittle superconducting core, but also must be ductile enough to withstand the mechanical working. The metal sheath has to play a role of diffusion barrier for the volatile and reactive Mg. Several sheath materials such as Cu, Ag, Ni, Nb, Ti, Fe and some alloys like SS, monel (Cu-Ni) are tried for

MgB_2. Of these most of the sheath materials form intermetallics or solid solutions with Mg/B, affecting the superconducting properties of the system to different extents depending on the reactivity [60].

In order to select a suitable sheath material, we carried out a systematic study of the reactivity of the commonly available sheath materials such as Fe, SS, Cu, Ag, Ni and Ta by mixing their fine powders with stoichiometric Mg and B and heat-treating the reaction mixtures at different temperatures. The studies showed that among the above metals only Fe, SS and Ta are acceptable for use as sheath materials for MgB_2 wire/tape fabrication. In the present work MgB_2 based wires and tapes were fabricated in both mono and multifilamentary geometries using Fe as the sheath material.

4.1 Reactivity of sheath materials with Mg/B

4.1.1 Experimental Details

The samples for reactivity study were prepared by *in situ* Powder-In-Sealed-Tube (PIST) method as detailed in chapter 3. Commercially available seamless stainless steel (SUS 304) tubes of 10 cm length with an outside diameter (OD) of 10 mm and inside diameter (ID) of 8 mm were used for the study. Stoichiometrically weighed and uniformly mixed Mg powder and amorphous B powder, added with a 10 wt.% sheath material powder viz. Ag, Cu, Fe, Ni, SS and Ta (99% purity, -200 mesh) were packed into the tubes, compacted mechanically and end-sealed by arc welding. Thirty such samples (five each with six different sheath material powders) were prepared and each set was subjected to heat treatment at 600 °C, 675 °C, 750 °C, 825 °C and 900 °C for 2 hours.

4.1.2 Characterizations

The phase analysis of the samples were performed by using powder XRD. Phase identification of the samples were performed using X'pert Highscore Software in support with ICDD-PDF-2 database. Quantitative phase analysis of the samples were carried out from the XRD. Microstructural examination and elemental analysis of the samples were done by using a scanning electron microscope (SEM-JEOL JSM 5600LV) equipped with an X-ray energy dispersive spectrometer (EDS).

4.1.3 Results and discussion

Figure 4.1 shows XRD patterns of the various sheath material viz. Ag, Cu, Fe, Ni, SS and Ta added samples heat treated at different temperatures viz. 600, 675, 750, 825, 900 °C for 2 h. The XRD measurements were performed on the ground cores, taken out by mechanically peeling off the SS sheath. From all the XRD patterns, it can be seen that MgB_2 formation is almost complete in all samples at around 825 °C and small peaks corresponding to MgO are also present.

For the Ag added sample (figure 4.1 a), reaction between Mg and Ag starts even at the temperatures of 600 °C. At 600 °C reaction between Mg and Ag forms an intermetallic $Ag_{0.24}Mg_{0.76}$, and after 750 °C, the $Ag_{0.24}Mg_{0.76}$ fully converts into MgAg, reducing the effective superconductor volume. Above 750 °C the amount of MgAg phase is considerable and some of the peaks are very strong and sharp. The presence of Ag-Mg phases strongly impede the flow of super-currents from grain to grain, causing a decrease of current carrying capacity of the system [60].

For the Cu added sample (figure 4.1 b), the competition in reaction among Mg, Cu and B led to different phase formations. Significant Mg-Cu reaction tookplace even at 600 °C resulting in the formation of the binary phase Mg_2Cu. As the reaction temperature is increased above 750 °C, Mg_2Cu undergoes partial decomposition and releases a part of the Mg and this results in a phase composition of $MgCu_2$. Thermodynamically, the Gibb's free energy of $MgCu_2$ is lower than that of Mg_2Cu and this explains the formation of $MgCu_2$ which is more stable at higher reaction temperatures. There were reports on the deleterious effects of $MgCu_2$ formation in Cu sheathed conductors at temperatures above 750 °C [163–165]. These reactive phases both Mg_2Cu and $MgCu_2$ act as obstacles to the supercurrent flow, creating weak links among MgB_2 grains.

For the Fe introduced sample, Fe remains inert towards both Mg and B at temperatures up to 825 °C (figure 4.1 c). For the 900 °C heat treated sample, the intermetallic compound Fe_2B begins to form due to reaction of Fe with boron. Being highly brittle in nature Fe_2B worsens the mechanical and conduction properties of the superconductor. Studies by Grovenor *et al* [166] showed the formation of Fe_2B at temperatures in excess of 850 °C. However, the best J_C for MgB_2 wires are generally obtained with Fe as the

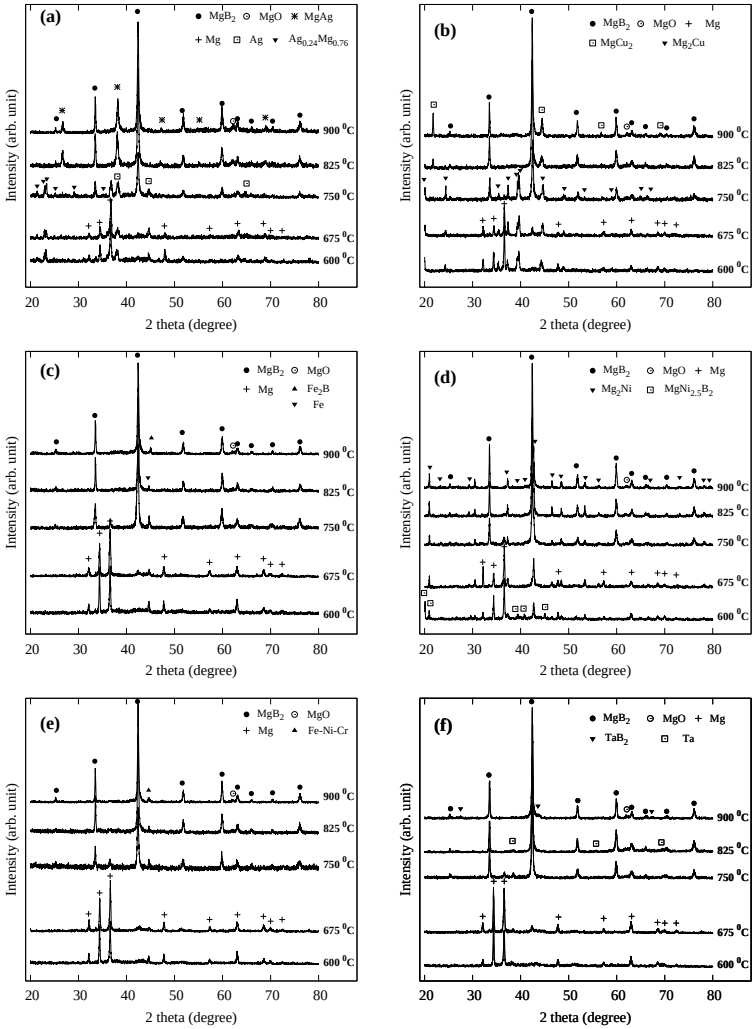

Figure 4.1: Powder XRD pattern of sheath material viz.(a) Ag, (b) Cu, (c) Fe, (d) Ni, (e) SS and (f) Ta added samples heat treated at different temperatures.

sheath material [167, 168], for relatively low temperature (< 850 °C) heat treated wires/tapes wherein the reaction between Fe and Mg/B is minimal.

Ni added samples showed significant reaction at temperatures as low as 600 °C causing the formation of Mg_2Ni (figure 4.1 d). At higher temperatures, boron also take part in the reaction process resulting in the formation of the tertiary compound $MgNi_{2.5}B_2$ in large quantities. Bellingeri *et al* [169] observed a thick reaction layer of $MgNi_{2.5}Bi_2$ by neutron diffraction at the Ni-MgB_2 interface while fabricating monofilamentary tapes.

Mg and B are found to be exceptionally inert with respect to stainless steel even up to the highest heat treatment temperature of 900 °C (figure 4.1 e), suggesting the chemical compatibility of SS for MgB_2 wire fabrication. It may be recalled that SS tubes were used for preparing all the samples in this study. However, not even a trace of any reacted phase is observed in any of the samples under the extreme heat treatment conditions used. No chemical reactions have been observed for the Ta introduced *in situ* processed samples upto a temperature of 825 °C (figure 4.1 f). At higher temperatures, Ta begins to react with B forming TaB_2 inside the core. The results of reactivity of *in situ* processed MgB_2 with various sheath materials at different temperatures are summarized in Table 4.1.

Table 4.1: Reaction products of Mg/B with various sheath materials.

Sheath	Heat treatment temperature				
material	600 °C	675 °C	750 °C	825 °C	900 °C
Ag	$Ag_{0.24}Mg_{0.76}$	$Ag_{0.24}Mg_{0.76}$	$Ag_{0.24}Mg_{0.76}$	MgAg	MgAg
Cu	Mg_2Cu	Mg_2Cu	Mg_2Cu	$MgCu_2$	$MgCu_2$
Ni	Mg_2Ni, $MgNi_{2.5}Bi_2$	$MgNi_{2.5}Bi_2$	$MgNi_{2.5}Bi_2$	$MgNi_{2.5}Bi_2$	$MgNi_{2.5}Bi_2$
Fe	No reaction	No reaction	No reaction	No reaction	Fe_2B
SS	No reaction	No reaction	No reaction	No reaction	No reaction
Ta	No reaction	No reaction	No reaction	No reaction	TaB_2

Figure 4.2 depicts the formation profile of the various phases formed in the reaction mixture with different sheath material powders during the *in situ* processing of MgB_2 heat treated at different temperatures. 'Other phases' labeled in the figure refers to all phases other than MgB_2 present in the samples and 'reactive phase' refers to compounds of sheath material with Mg and B. In all the cases formation of MgB_2 starts at 600 °C and the reaction rate attains a maximum in the temperature range from 675

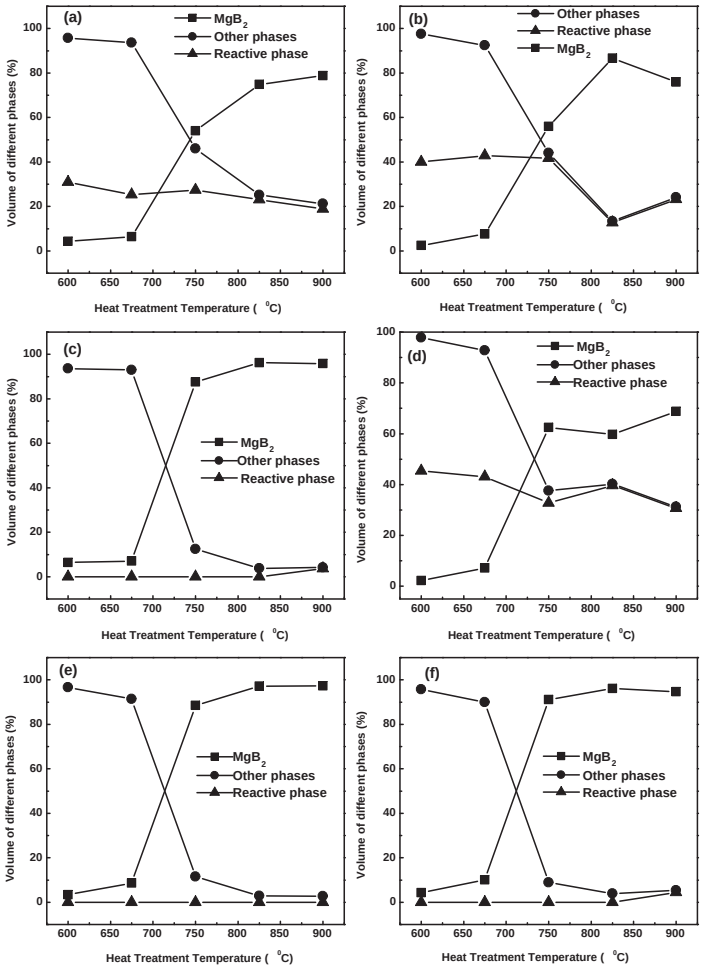

Figure 4.2: Quantitative values of the various phases formed in the sheath material (a) Ag, (b) Cu, (c) Fe, (d) Ni, (e) SS and (f) Ta introduced *in situ* processed MgB_2 at different temperatures.

to 750 °C irrespective of the added sheath material powder. For Fe, SS and Ta the MgB_2 formation curves are almost identical (figure 4.2 c, e and

f) yielding high purity MgB_2 (Vol.% of 96.2, 97.2 and 96.1 respectively) at a temperature of 825 °C with little or no reacted phases. Beyond this temperature the rate of MgB_2 formation stagnates without any significant deterioration in purity upto 900 °C. But Ag, Cu and Ni added samples show (figure 4.2 a, b and d) markedly larger amount of reactive phases, considerably reducing the relative amount of MgB_2 phase in the core to 78.8%, 86.8% and 68.8% respectively within the temperature 900 °C. Of these, volume % of MgB_2 is lowest for the Ni added samples. The much higher reactivity of Ag, Cu and Ni make them unsuitable for the fabrication of MgB_2 based conductors even at lower temperatures.

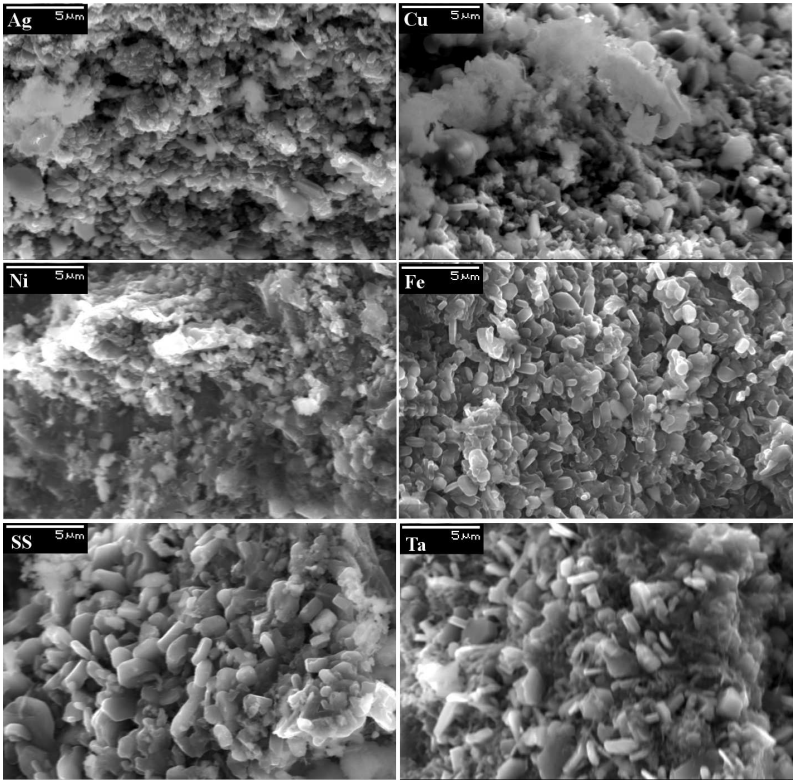

Figure 4.3: SEM images of the sheath material viz. Ag, Cu, Fe, Ni, SS and Ta added samples heat treated at 900 °C/2h.

Figure 4.3 shows the scanning electron micrographs (SEM) of various sheath material introduced *in situ* processed MgB_2 samples heat treated at 900 °C/2h. Typical hexagonal grains of MgB_2 can be observed in all the microstructures. However, larger quantities of fine grained precipitates of the reacted products are observed for Ag, Cu and Ni added samples, showing their extensive reaction with Mg and/or B. In order to find out the atomic composition of the reacted phases energy dispersive X-ray (EDX) analysis was carried out. Figure 4.4 shows typical energy dispersive spectra (EDS) of the precipitated areas of Ag and Cu added *in situ* processed MgB_2 samples. The EDX microanalysis has revealed that the precipitated area of Ag added sample has an approximate atomic composition Mg : Ag of 1:1 (MgAg) and for Cu added sample, it has a composition Mg:Cu of 1:2 ($MgCu_2$). These observations are consistent with the X-ray diffraction studies.

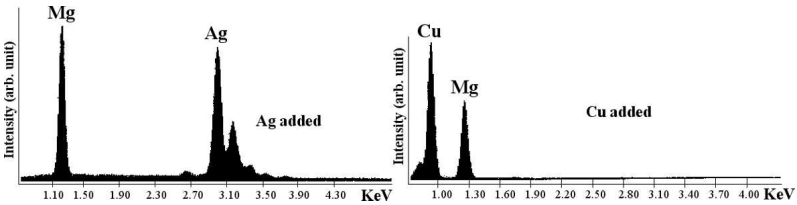

Figure 4.4: Energy dispersive spectra (EDS) of the reactive phase formed in Ag and Cu added samples heat treated at 900 °C/2h.

For an *in situ* conductor fabrication method, the sheath material plays a very crucial role in determining the superconducting properties of MgB_2 conductors. Conductors with better properties could be achieved if we use the right sheath material which should be primarily non-reactive with Mg/B at heat treatment temperatures. The present study shows that Ag, Cu and Ni undergo markedly higher reaction during the *in situ* processing of MgB_2, which make them unsuitable for conductor fabrication. On the other hand, SS, Fe and Ta show no or very little reaction at the heat treatment temperatures and hence these can be considered as potential candidates for MgB_2 wire manufacturing. However, factors such as limited mechanical workability of SS and high cost of Ta make Fe, the best choice as the sheath material for *in situ* MgB_2 wire/tape fabrication.

4.2 Influence of sheath material reactivity on superconducting properties of MgB_2

4.2.1 Experimental Details

Based on the above study of the reactivity of various sheath materials with Mg/B, four samples, added with Fe, SS, Cu and Ni, (10 wt.% of each) and heat treated in air at 825 °C for 2 hours were selected for superconducting property measurements. Here after the samples added with SS, Fe, Cu and Ni are named as MBSS, MBFe, MBCu and MBNi respectively. The superconducting magnetic measurements were carried out by a vibrating sample magnetometer in Physical Property Measuring System (PPMS), Quantum Design, USA on the rectangular shape of samples having sizes of 3mm $\times$ 3mm $\times$ 1.5mm.

4.2.2 Results and discussions

The XRD patterns of the samples are shown in different plots in figure 4.1. However for the sake of comparison, the XRD patterns of samples added with SS, Fe, Cu and Ni sheath powders and heat treated at 825 °C for 2h are shown in figure 4.5. All X-ray diffraction results give sharp peaks of MgB_2 phase with only a minute fraction of MgO. The impurity phases formed are marked in the figure. Lattice parameter calculations show that there is no significant variation in lattice parameters *a* or *c* of MgB_2 (table 4.2) within the experimental limit. This indicates that the added sheath materials are not substituted at either Mg or B sites in MgB_2. The lattice parameters *a* and *c*, Vol.% of MgB_2 phase, T_C, H_{irr} and J_C data for MBSS, MBFe, MBCu and MBNi samples obtained from this work are summarized in table 4.2.

Figure 4.6 illustrates the DC magnetization versus temperature (M-T) plots in zero field cooled (ZFC) condition under an applied field of 20 Oe for SS, Fe, Cu and Ni added MgB_2 samples. The ZFC branch of the magnetization undergoes a diamagnetic transition in the range 37.8-38.5 K. Fe added sample shows relatively higher T_C (38.5 K) while T_C of MBSS (38.2 K) and MBCu (38.3 K) are almost same and that of MBNi sample is slightly lower (37.8 K). The lower T_C of Ni added sample may be due to the reduction of superconducting volume (60% MgB_2) which is cleared from quantitative phase analysis of XRD data, as shown in table 4.2. The samples MBSS and MBFe exhibit positive magnetization above transition

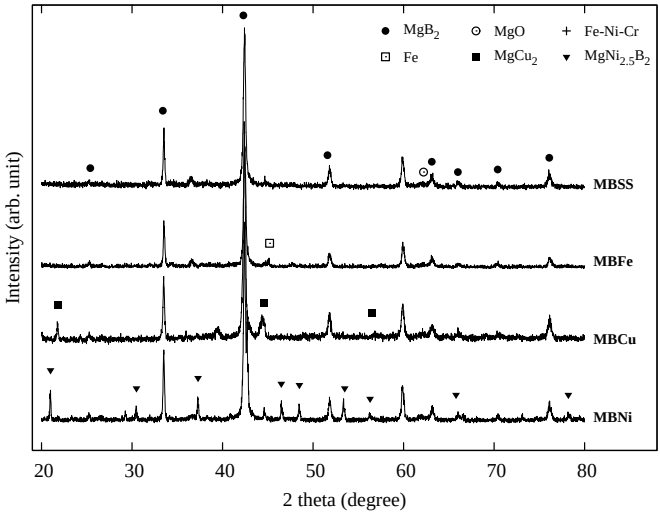

Figure 4.5: X-ray diffraction patterns for MgB_2 samples added with 10 wt.% of sheath powder SS, Fe, Cu and Ni and heat treated at 825 °C/2h.

temperature, likely due to the paramagnetic or ferromagnetic nature of additives. Although Ni is ferromagnetic below its curie temperature, Ni added MgB_2 sample does not show any positive magnetization above T_C since the Ni powder reacted with Mg and B forming $MgNi_{2.5}Bi_2$.

Table 4.2: Structural and superconducting characteristics of MgB_2 samples added with sheath materials. J_C and H_{irr} values are are at 5 K

Sample	a (Å)	c (Å)	Vol. of MgB_2 (%)	T_C (K)	J_C at 2 T (A/cm^2) ($\times 10^4$)	J_C at 5 T (A/cm^2) ($\times 10^3$)	H_{irr} (T)
MBFe	3.086	3.525	97.2	38.2	11.8	6.8	7.8
MBSS	3.089	3.523	96.2	38.5	8.5	5.2	7.7
MBCu	3.084	3.526	86.6	38.3	5.2	2.9	7.1
MBNi	3.086	3.525	60.0	37.8	4.5	2.0	6.9

The field dependent magnetization of MgB_2 samples added with sheath powders SS, Fe, Cu and Ni is shown in figure 4.7. It appears that the first

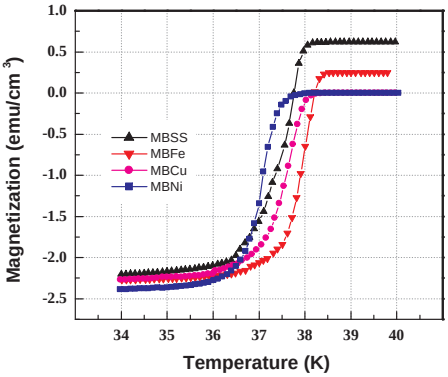

Figure 4.6: M-T plots in zero field cooled (ZFC) condition at 20 Oe for MBSS, MBFe, MBCu and MBNi.

and third quadrants and the second and fourth quadrants are replica to each other. The magnetic hysteresis loop widths of MBSS and MBFe are larger than those of MBNi and MBCu showing the former's higher magnetization under external magnetic field. Samples MBFe and MBSS show slight paramagnetic shift due to the presence of paramagnetic components such as Fe and SS powders.

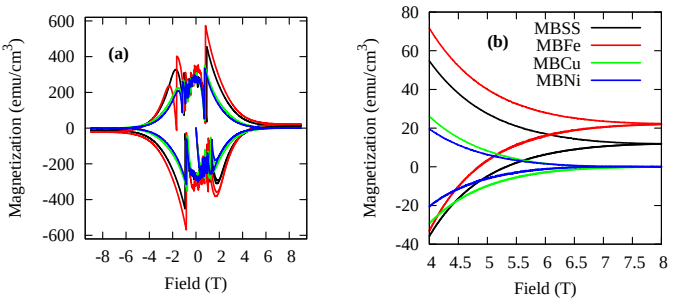

Figure 4.7: (a) M-H plots (at 5 K) of MgB_2 samples added with sheath powders SS, Fe, Cu and Ni and (b) enlarged view at high fields.

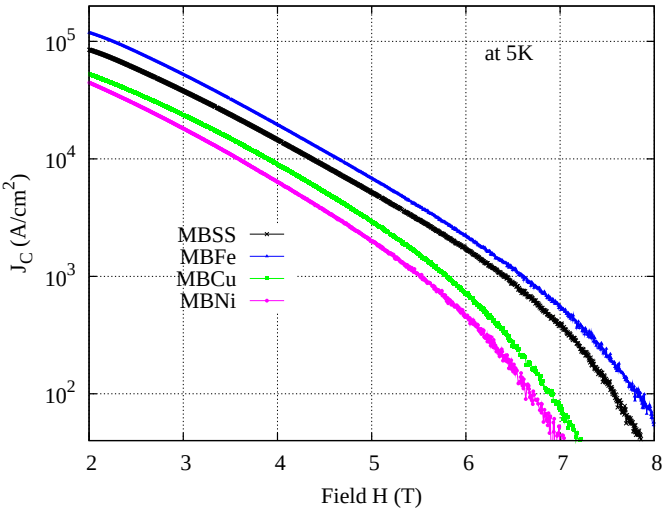

Figure 4.8: $J_C(H)$ curves at 5 K of MgB_2 samples added with sheath powders SS, Fe, Cu and Ni.

The critical current density (J_C) was estimated from the width of the M-H curves in applied fields (H) at 5 K by using Bean model. Figure 4.8 shows the dependence of J_C with magnetic fields upto 8 T. As shown in the figure $J_C(H)$ characteristics imply that the intragrain J_C of Fe added MgB_2 sample attains better values among all samples. The intragrain J_C values for MBFe sample are 11.9 $\times$ 10^4 A/cm^2 at 2 T and 6.8 $\times$ 10^3 A/cm^2 at 5 T whereas for MBSS sample J_C values at 2 T and 5 T are 8.5 $\times$ 10^4 A/cm^2 and 5.2 $\times$ 10^3 A/cm^2, comparable to that of Fe added sample. J_C values of sample MBCu are 5.2 $\times$ 10^4 A/cm^2 at 2 T and 2.9 $\times$ 10^3 A/cm^2 at 5 T and those of MBNi are 4.5 $\times$ 10^4 A/cm^2 at 2 T and 2 $\times$ 10^3 A/cm^2 at 5 T. Enhanced J_C values of Fe and SS added samples show a direct correlation with their better phase purity comparing with Cu and Ni added samples. At higher fields MBSS and MBFe samples show two or three times larger J_C than the other samples containing reacted phases. The steep drop in J_C at higher fields (> 6 T) in all samples is attributed to the flux penetration into the grain boundaries that may contain impurities. The weaker grain connectivity and greater flux penetration due to the presence of impurities of reacted sheath powders in the grain boundaries lead to a larger reduction of J_C in MBCu and MBNi samples at higher fields.

The irreversibility field H_{irr}, defined as the field at which critical current J_C falls below 100 A/cm^2, for all samples at 5 K is shown in table 4.2. For MBFe and MBSS H_{irr} values at 5 K are 7.8 T and 7.7 T while those of MBCu and MBNi are 7.1 T and 6.9 T respectively. Higher H_{irr} of Fe and SS added samples is attributed to the higher superconducting area, better microstructure and unreacted sheath powders in MgB_2 acting as grain boundary pinning centers. The reacted additives in Cu and Ni added samples reduce the superconducting area and weaken the grain connectivity without any enhancement in flux pinning, causing reduced $J_C(H)$ and H_{irr} values.

From the results it is very clear that Fe is the most suitable material with respect to chemical inertness with Mg/B at the reaction temperature and retention of superconducting properties of the MgB_2 core. Fe is easily available and is relatively cheap. It has adequate hardness to give mechanical support to the brittle superconducting core. It has enough strength and ductility to withstand mechanical rolling. Fe sheath effectively acts as a diffusion barrier for the volatile and reactive Mg. Considering these facts we choose iron as the sheath material for MgB_2 conductor fabrication.

4.3 Preparation of MgB_2 conductors

Mono and multifilamentary MgB_2 wires and tapes were prepared by the *in situ* Powder-In-Tube (PIT) method. Figure 4.9 presents the preparation method of mono and multifilamentary MgB_2 wires and tapes.

4.3.1 Monofilamentary wires and tapes

Fe tubes of length 2.5-5 cm, outside diameter 4 mm and inside diameter 2 mm were used for the regular short length conductor fabrication. For long length conductors 5-10 cm long and OD/ID of 8/6 or 5/3 mm tubes were used. The tubes were filled with homogeneously mixed Mg and B powders and mechanically compacted. Brass studs were used as plugs to seal the ends of the tubes. The composite tubes were groove rolled down to desired dimensions without any intermediate annealing. The regular wires prepared had a diameter of 1.4-2.0 mm, while the minimum diameter for rolled wire was $\sim$ 1.1 mm. For the preparation of tapes these groove rolled wires were then flat rolled to the desired geometry, using a flat roller. Typical flat rolled tapes had dimensions 3-4 $\times$ 0.8-1.6 mm (width $\times$ thickness).

The ends of the wires and tapes were sealed by arc welding. These wires and tapes were then heat treated at 650-750 °C for 0.5-2 hours. Some of the wires/tapes were heat treated by electrical self-heating (described in section: 4.8) and others were heat treated in a muffle furnace. After heat treatment short length samples were cut for various characterizations.

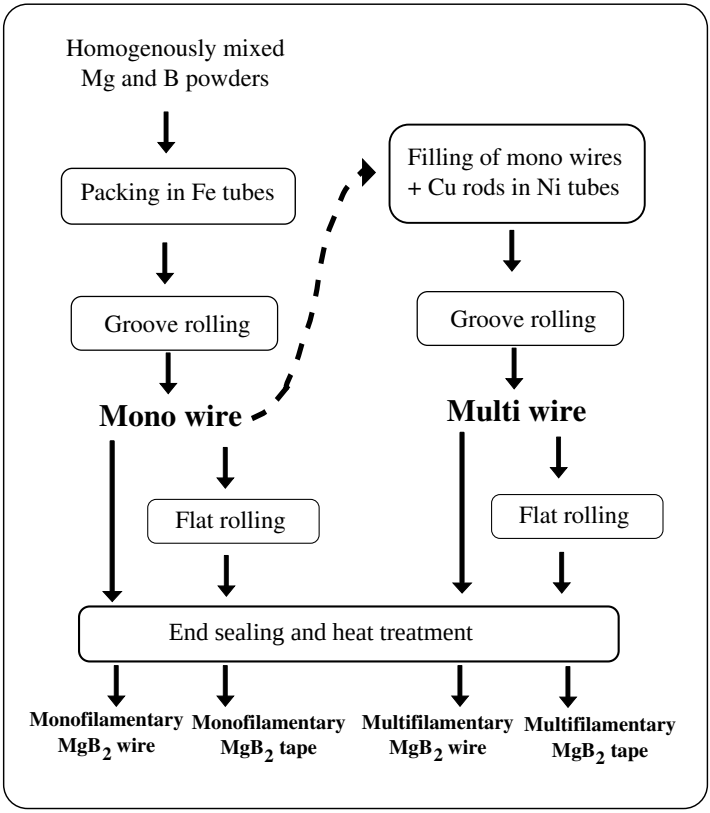

Figure 4.9: Flowsheet showing the preparation method of mono and multifilamentary MgB_2 wires and tapes.

4.3.2 Multifilamentary wires and tapes

In a stabilized practical multifilamentary conductor, there has to be many filaments of sheathed MgB_2 superconductor in a metallic matrix. A signifi-

cant area fraction of the multifilamentary conductor must contain a thermal stabilizer material:- metals with high thermal and electrical conductivities. During an accidental quench the stabilizer has to dissipate the heat generated in the conductor as fast as possible. The stabilizer also provides a parallel path to the current flow during the quench. In the present work we prepared multifilamentary MgB_2 conductors using Fe as inner sheath, Cu as stabilizer and Ni as outer sheath. Cu is used as the stabilizer, since it has high thermal and electrical conductivity and relatively low cost.[1] The outer sheath must have good mechanical properties to support the conductor and must be chemically stable with environment. We have considered stainless steel (SS), mild steel (MS), monel (an alloy of Cu and Ni) and Ni for the outer sheath material. Among these Ni is chosen as the outer sheath due to its high oxidation resistance at high temperature heat treatment and good mechanical properties.

To prepare multifilamentary wires the grove rolled monofilamentary wires (OD $\sim$ 2-2.5 mm) were cut, bundled and packed inside Ni tubes of outside diameter 8 mm and inside diameter 6 mm. Cu wires of diameter 0.75-2 mm were also bundled inside the Ni tube along with the filaments. The composite was then then groove rolled for multifilamentary wires. For the preparation of tapes these groove rolled wires were then flat rolled to the desired geometry. The rolled wires and tapes were then heat treated as in the case of monofilamentary ones. The maximum length of the wire prepared is about 2 m and the maximum number of filaments in multifilamentary wires is 10. A typical wire has 1.5-2 mm outside diameter and a typical stabilized tape has the dimensions of $\sim$ 1-2 mm thickness and 3-5 mm width and upto 10 superconducting filaments.

Figure 4.10 shows a schematic diagram of the filling and rolling processes for both mono and multifilamentary conductors and for both wire (groove rolling) and tape (flat rolling) rolling. For the rest of the thesis, the following short names are used to represent mono and multi filamentary wire and tape samples.

Mono (Single) filamentary Wire	SW
Mono (Single) filamentary Tape	ST
Multi filamentary Wire	MW
Multi filamentary Tape	MT

[1] Silver (Ag) also has high thermal and electrical conductivity, but it is expensive.

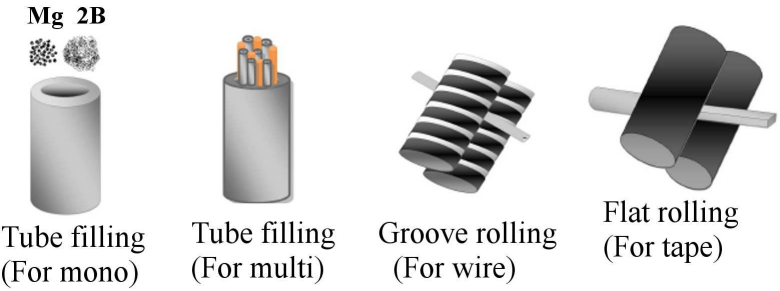

Figure 4.10: Schematic diagram of the filling and rolling processes for mono and multifilamentary conductors.

4.4 Problems faced during fabrication of conductors

Compared to the MgB_2 bulk preparation, the wire and tape preparations were faced with a number of problems. The major problem faced during fabrication was the cracking of the sheath material. Even micro cracks proved costly because MgO content of such samples was very high which seriously affected the superconducting property. Figure 4.11 (a) shows a piece of wire which cracked during rolling. Figure 4.11 (b) shows the same region after the heat treatment. Here the crack is further developed and the MgO formed is seen as a white cloudy mass. For wires and tapes the surface cracking during rolling arises mainly due to work hardening and/or sheath thinning. By selecting tubes with proper wall thickness, optimizing the initial powder packing density and controlling the area reduction rate during rolling etc we could solve the sheath cracking problem completely. For tapes, in addition to the surface cracking, there was edge cracking also. This generally occurred during initial stages of flat rolling, where the cross section of the conductor starts to change from circular to rectangular. This problem also was solved by controlling the rolling parameters such as rolling speed and area reduction ratio per pass etc. For both wires and tapes the cracking tendency was higher for multifilamentary geometries. The problem of cracking was more in lower grooves.

In the case of multifilamentary conductors the ductility mismatch between Fe, Cu and Ni also caused rolling problems. These materials elongate differently during the initial stages of rolling. The initial non uniform

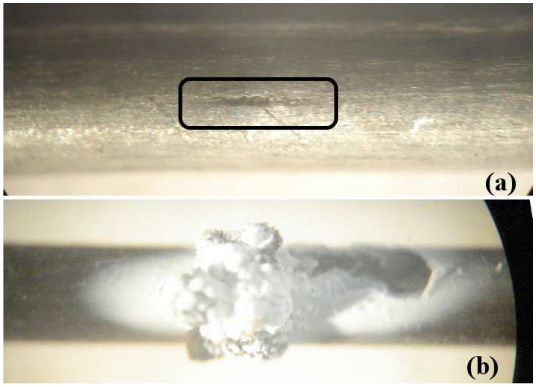

Figure 4.11: Photograph of (a) a macro scale crack on the surface of a rolled mono wire and (b) the same region after heat treatment (The photograph is taken on electrically self-heated sample). Here the crack is further developed and the MgO formed is seen as a white cloudy mass.

elongation results non uniform properties at both the ends, compared to the middle of the conductor. As the rolling progresses the diameter of the composite tube gets reduced and the whole composite elongates together. In order to account this, a portion of both ends of the rolled conductors were cut before heat treatment. The end sealing of conductors before heat treatment also raised some hurdles. Fe is easily weldable while Ni and Cu are not. A capping technique is used to perfectly seal the ends. In this, the ends of the conductors were inserted to suitable iron tubes of short length and mechanically fixed with the conductor and then ends of the iron tubes were welded. Figure 4.12 shows schematic illustrations of the problems as described above.

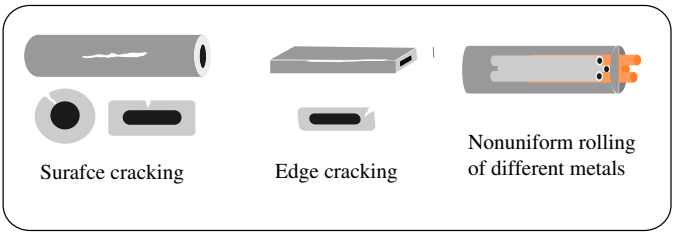

Figure 4.12: Schematic Illustrations of some of the problems faced during rolling.

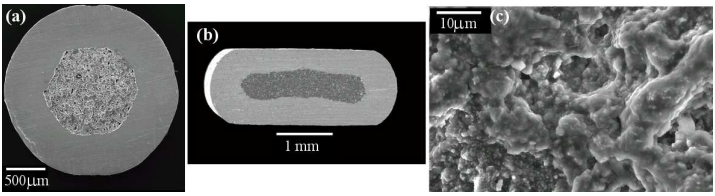

Figure 4.13: SEI SEM images of cross sections of (a) mono wire, (b) mono tape and (c) the core of mono wire.

4.5 Structural characteristics of MgB_2 conductors

Figure 4.13 shows the SEI SEM images of a mono filamentary wire (a) and tape (b). The images also show distinct and clear sheath and core as observed in the optical micrographs. Figure 4.13 (c) shows the enlarged view of the core of the wire. The image shows large pores in the core, characteristics of *in situ* synthesized MgB_2, caused due to the low green

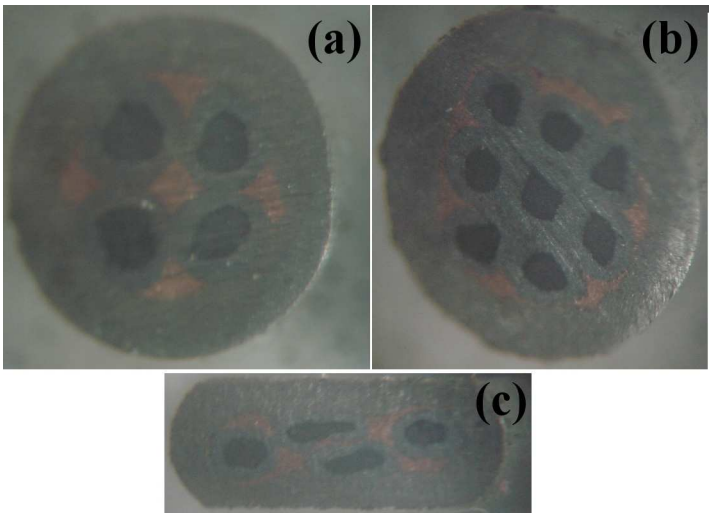

Figure 4.14: Optical micro graphs of multifilamentary MgB_2 conductors (a) 4 filament wire (b) 8 filament wire and (c) 4 filament tape. Dimensions : OD = 2.1 mm for wires and cross section = 4×1 mm^2 for tape.

density of the mixtures and the volume shrinkage during MgB_2 formation.

Figure 4.14 shows the optical micrographs of the cross sections of some of the monofilamentary and multi filamentary samples. The micrographs show the MgB_2 core distinct and clear in both mono and multi. The outer sheath, superconducting core and the metallic matrix are clearly visible and distinguishable. The core-sheath interface is observed to be distinct, indicating the non-reactivity of the core with sheath metal. The Cu wires are also clearly visible without any significant diffusion between the different metals. No cracks or non uniformities were observed and the cross section of the wire and tape are almost circular and rectangular respectively in the micrographs.

Optical microscopy measurements, taken with the help of a scale built into the eyepiece, were used for the exact estimation of core and sheath cross sectional areas of mono/multi filamentary wires/tapes. For both mono wires and tapes, MgB_2 core has $\sim 25\%$ and the Fe sheath has $\sim 75\%$ of the total cross sectional area respectively. The relative cross sectional area of MgB_2 core for mono filamentary wire and tapes are shown in figure 4.15. For a typical multifilamentary conductor the cross sectional area $\sim 10\%$ for MgB_2 core, $\sim 8\%$ for Cu, $\sim 35\%$ for Fe and $\sim 47\%$ for the outer Ni sheath.

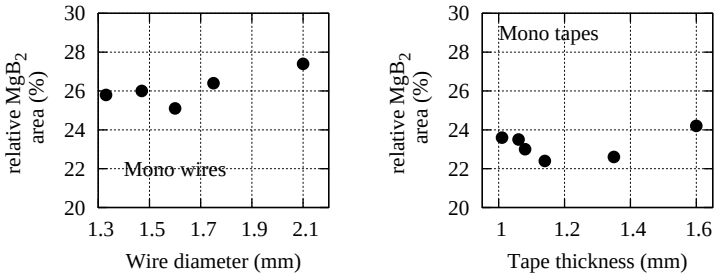

Figure 4.15: The cross sectional area of MgB_2 core (in percentage) for mono filamentary wires and tapes for different diameter and thickness.

The powder XRD pattern of the ground MgB_2 core of a monofilamentary wire is shown in figure 4.16, as a typical case. Crystalline MgB_2 with minor amounts of MgO is observed in the samples. Unlike some of

the earlier reports no peaks of Fe containing phases such as Fe_xB phases are observed in the samples. This shows the non-reactivity of the sheath material with the Mg/B powders at the reaction temperature. The quality (crystallinity and phase purity) of MgB_2 formed in the wire/tape is as good as that of MgB_2 bulks prepared by PIST method as discussed in chapter 3. Calculated lattice parameters of the prepared MgB_2 wires and tapes were consistent with the values observed for bulks.

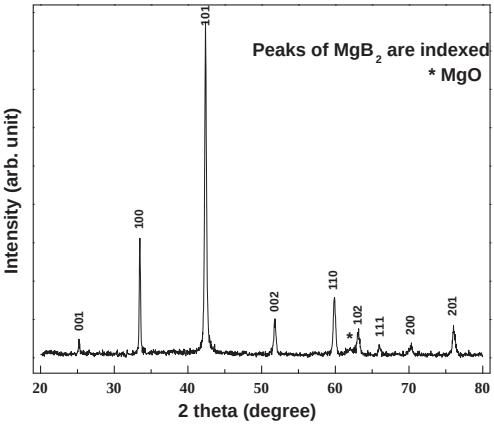

Figure 4.16: Powder XRD pattern of the ground MgB_2 core of a monofilamentary wire.

4.6 Superconducting properties of MgB_2 conductors

Figure 4.17 and 4.18 show the resistance versus temperature plots of a mono and multifilamentary wire and tape samples. Inset of the figures show the enlarged plots near the transition region. Both mono and multi wire and tape have sharp transition at around 39 K. Mono filamentary conductors have a transition temperature (T_C) in the range 38.2-39.0 K with transition width ΔT_C < 1 K. For multi filamentary conductors the T_C was in the range 38.0-38.5 K with transition width ΔT_C < 1.5 K. The almost

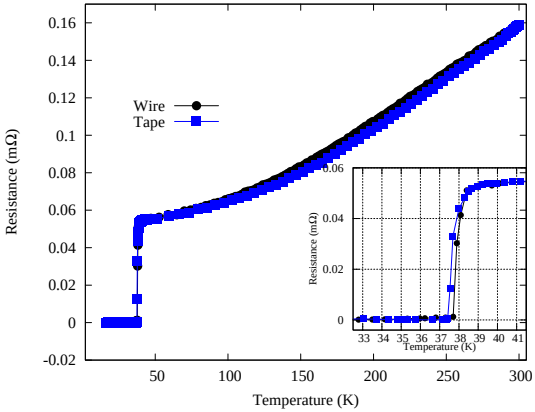

Figure 4.17: R-T plots of typical monofilamentary wire and tape. Inset of the figure shows zoomed view near the superconducting transition.

constant T_C and low ΔT_C values of the wires/tapes as those observed in bulk samples indicate the good quality and homogeneity of the superconducting core in the wire/tape.

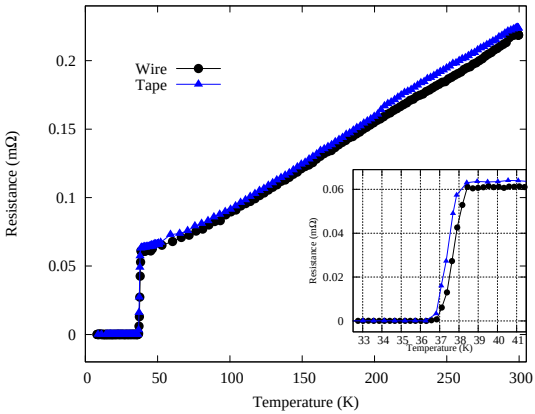

Figure 4.18: R-T plots of typical multifilamentary wire and tape. Inset of the figure shows zoomed view near the superconducting transition.

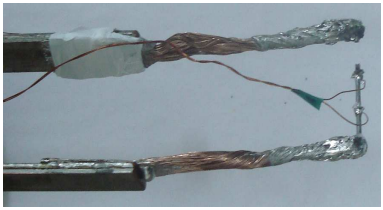

Figure 4.19: Photograph of a sample contact melted during high current transport measurement.

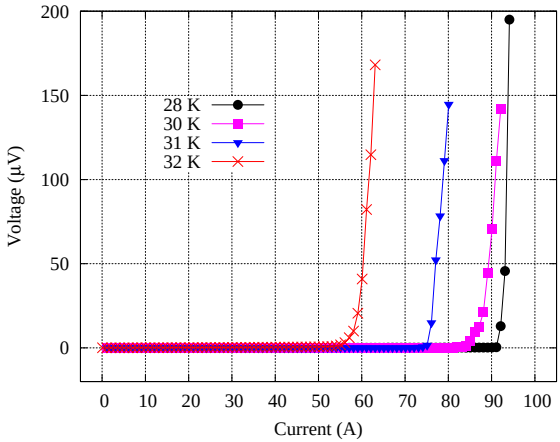

Figure 4.20: I-V plot of a typical monofilamentary MgB_2/Fe wire (1.33 mm diameter) at different temperature.

Another important task is to find the current carrying capability of the prepared conductors. The measurement of transport current properties of MgB_2 conductor is difficult especially at high currents (in self-field). The rapid warming of the current contacts may cause a premature quench and subsequent burn out of the sample. In cases when very high currents are passed the contact, especially the solder joints melts. Figure 4.19 shows the photograph of such a sample where the contact is broken. The current contact melted while passing $\sim$ 870 A current through the sample (monofilamentary wire of OD $\sim$ 1.33 mm, length 3 cm) at 4.2 K and self-field. In the present study I-V measurements (cryocooler based) were done at relatively high temperatures to restrict the current to low values, other

wise the heat generated at the current leads and contacts make the transport measurements difficult in the conduction cooling system.[2]

Figure 4.20 shows the I-V characteristics of a monofilamentary MgB_2 wire at different temperatures. The sample had a length of 6.5 cm and $\sim$ 1.33 mm diameter. The wire had a MgB_2 core of $\sim$ 0.68 diameter. the sample was heat treated at 650 °C for 1 hour. The I-V measurement is done at 28, 30, 31 and 32 K using a closed cycle cryostat, where the sample is cooled by conduction. Current is passed through the sample for few seconds and the corresponding voltage drop across a tap of gap 2 cm is noted and then the current was switched off for few seconds to remove the heat generated in the current leads. The wire showed a critical current of $\sim$ 91 A at 28 K, 85 A at 30 K, 75 A at 31 K and 56 A at 32 K respectively. Table 4.3 shows the corresponding critical current density and engineering current density for the sample. The sample have a engineering current density of more than 10^3 Acm^{-2} and critical current density of more than 10^4 Acm^{-2} at a temperature around 30 K.

Table 4.3: Critical current characteristics of the sample for the I-V plot shown in figure 4.20

Temperature (K)	I_C (A)	J_E ($\times 10^3$ Acm^{-2})	J_C ($\times 10^4$ Acm^{-2})
28	91	6.5	2.5
30	85	6.1	2.3
31	75	5.4	2.1
32	57	4.0	1.5

Figure 4.21 shows the I-V characteristics of selected multi filamentary wires and tapes at 30 K. The corresponding engineering and critical current densities are tabulated in the inset of the figure. The wires have 1.6 mm diameter and 5 (for MW1) and 8 (for MW2) superconducting filaments. The tapes measured have cross sections 3.2 $\times$ 1.0 and 2.6 $\times$ 1.1 (in mm)

[2]During the undesirable quench the measured parameters may not be the intrinsic property of the conductor. It has also been suggested that some of the high *n* (sharp transitions) values measured arise due to the heating during the I-V measurement, rather than the intrinsic value [170]. In order to avoid these difficulties it is a general practice to measure the transport properties at relatively higher temperatures or higher applied fields [171–174].

and 4 superconducting filaments. Sample MW1 has a sharp transition at around 96 A, while the 8 filament multifilamentary wire of same OD has a less sharp transition at around 80 A. The tape samples have relatively lower I_C and J_C values compared to the wire samples.

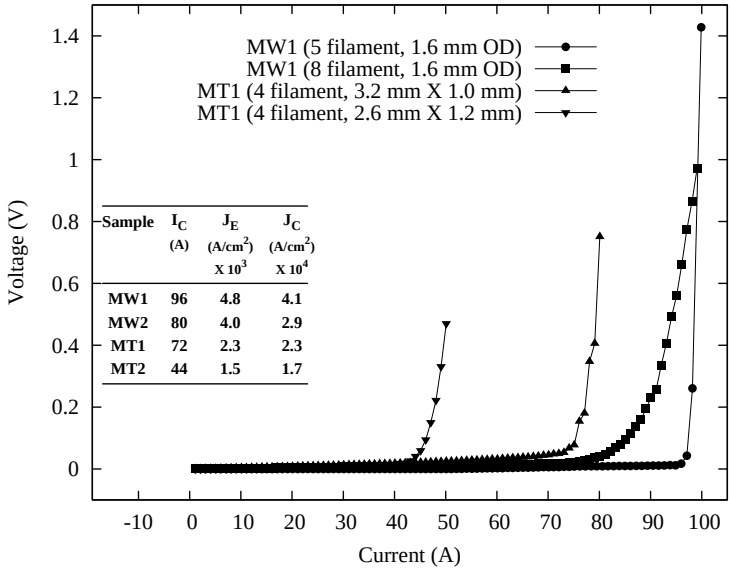

Sample	I_C (A)	J_E (A/cm^2) X 10^3	J_C (A/cm^2) X 10^4
MW1	96	4.8	4.1
MW2	80	4.0	2.9
MT1	72	2.3	2.3
MT2	44	1.5	1.7

Figure 4.21: I-V plot of typical multifilamentary MgB_2 conductors at 30 K.

4.7 Continuous current characteristics of multifilamentary MgB_2 conductors (In helium vapour)

In the present work transport current measurements of the MgB_2 conductors were done using a closed cycle cryocooler based cryostat or in a liquid helium cryostat. In the cryocooler based measurements the sample was in a vacuum chamber and was cooled by conduction. In the liquid helium dewar or cryostat, the sample was in liquid or vapor helium and was cooled by the direct contact with liquid or vapor helium. In the cryocooler measurements transport currents were passed for short durations only, while in

the liquid helium cryostat measurements the transport currents were passed continuously, with different ramp rates. This section describes the results and analysis of continuous transport current measurements done in liquid helium cryostat. All the measurements were done at the superconductor and magnet division, Institute of Plasma Research (IPR), Gandhinagar.

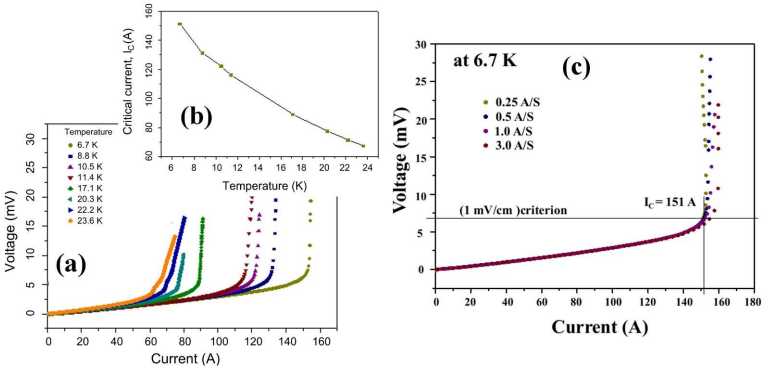

Figure 4.22: (a) I-V plot of a multifilamentary wire at different temperatures, (b) the variation of critical current with temperature and (c) I-V plot for different current ramp rates.

Figure 4.22 (a) shows the I-V plots of a multifilamentary wire at different temperatures. Figure 4.22 (b) shows the plot of critical current (I_C) versus temperature for the sample. The measurements were done with current ramp rate of $\sim$ 1 A/S. The sample measured had an outer diameter of $\sim$ 2.0 mm, length of 10.5 cm. The voltage taps were soldered in the middle of the sample with a gap of 6.5 cm between them. The sample shows relatively sharp transition at lower temperatures, but the transition is less sharp or slightly broadened at higher temperatures. In the I-V plot at 6.7 K, the voltage across the voltage tap increases sharply above 151 A. And thus 151 A is taken as the I_C of the sample at 6.7 K. The sample has I_C of 151 A 6.7 K, while at 23.6 K the value of I_C is decreased to 68 A. The value of I_C of the sample decreases almost linearly with the temperature.

In all the I-V plots, before the sharp rise in the voltage (for currents below I_C) a current depended linear background voltage is observed. This background voltage observed is due to the current transfer problem [pages 307-317 of ref: 175]. In principle, for currents far below the critical current

the voltage should be close to zero. This background voltage observed in the samples is due to the current sharing problem between the superconducting filaments and the metallic materials (sheath, matrix and stabilizer), and the problem of current transfer needs special attention for the development of MgB_2 conductor.

In a sheathed conductor, the transport current has to pass through the contact materials (current lead and solder) and also through the metallic sheath before entering into the superconducting core. The penetration of current from the outer core to the superconducting core happens over a length, depending on the nature of the sheath material and the interface between the sheath and superconductor [176, 177, and pages 306, 307 of ref:14]. such a current transfer is accompanied by additional voltage close to the current contact [178, 179]. [3]

Figure 4.22 (c) shows the I-V characteristics of the wire measured with different current ramp rates at 6.7 K. The background voltage observed is independent of the current ramp rate at all the temperatures. But the onset of sharp rise in voltage (I_C) shows some dependence with the current ramp rate. In general the value of I_C is slightly higher for measurements done with higher current ramp rate. This is behavior is observed for measurements done at other temperatures also.

Two more multifilamentary samples (one wire and one tape) were measured for analyzing the transition details. The details of samples are given in table 4.4. The samples used had four MgB_2 filaments and voltages from

[3] In a straightforward model of a joint between a metal lead and a superconductor the current in the lead decays exponentially [179, 180] and the current transfer length is approximated as the ratio between the transverse matrix to filament resistance and the longitudinal matrix resistance. So that

$$\lambda = \sqrt{\frac{R_b \times t_n}{\rho_n}}$$

where R_b is the resistance per unit area of the matrix-superconductor interface and t_n is the interface thickness and ρ_n is the longitudinal resistivity of the matrix (sheath). From this equation it is clear that the current transfer length increases with interface resistance and its thickness, which are much higher in the case of multifilamentary conductors. For a typical Fe sheathed mono filamentary MgB_2 conductor the current transfer length will be several (1-4) milli meters [178, 179]. For a multifilamentary conductor (as studied here) there are materials with different resistivities and different interfaces, making the current transfer from the outer sheath to the superconductor much more complex.

two sets of taps from each sample were monitored for studying the nature of transition.

Table 4.4: Details of samples measured for I-V characteristics.

Sample name	Geometry	Cross sectional dimensions	Length (cm)	Distance (cm) between voltage taps	
				Tap 1	Tap 2
MW	wire	ϕ = 2.1 mm	10.5	6.0	10.0
MT	tape	3.0 × 1.2 mm^2	7.5	3.7	7.0

Figure 4.23 shows the I-V characteristics of the MW and MT samples, at 15 and 21 K, respectively. Figure 4.23 (a) shows the I-V plots in linear scale and, while figure 4.23 (b) shows the same with the y axis (Voltage) in log scale. For both the samples current is charged at $\sim$ 1 A/s. The sample MW shows a sharp transition at 208.4 A (at 15 K). The transition point is same (208.4 A) for both the voltage taps having gap 6 and 10 cm, and the voltage rises sharply for both the taps above the transition. The similar response in both the voltage taps indicates good superconducting homogeneity along the length of the sample. For the tape sample the transition is less sharp compared to the wire. The transition (voltage rise) started at around 110 A in both the voltage taps and the slop of the curve changed significantly around 150 A.

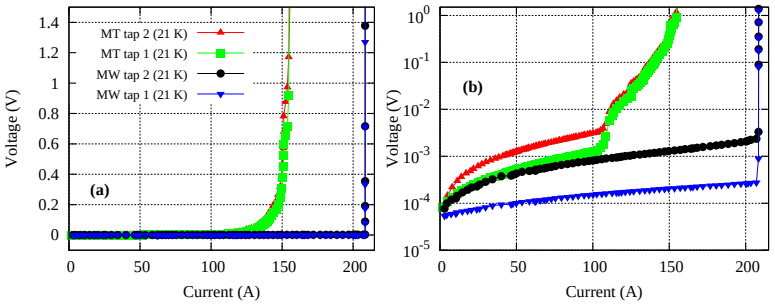

Figure 4.23: I-V plot of samples MW and MT in(a) linear-linear and (b) log-linear scales.

The log scale plot given in figure 4.23 (b) clearly shows the current depended voltage below the sharp rise in voltage. The values of background

voltage were more in tap 2 for both the wire and tape samples. This is expected as the tap 2 has large gap between them and are close to the current contacts than tap 1. So that the current transfer interfered with these readings. The background voltage is more for the tape sample.

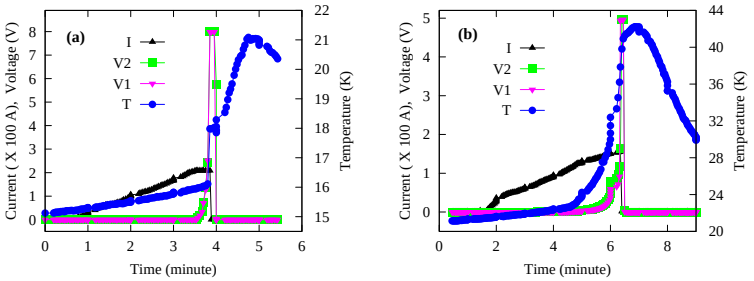

Figure 4.24: Transport current, voltage across taps and the sample temperature during the measurement, for (a) wire and (b) tape sample. Legends are I:Current, V1: Voltage at tap 1, V2: Voltage at tap 2 and T: Temperature.

Figures 4.24 (a) and (b) show the transport current, voltage across the two voltage taps on the sample and the sample temperature during the measurement for the wire and tape samples respectively. The current values are shown in multiples of hundred for clear visibility. For both the wire and tape the two figures show identical behavior (except the values of the parameters). Considering the plot of wire sample, the sample showed an I_C of 208.4 A as shown in I-V plots. At this value of current the voltage across of both the taps raised sharply. The current sources voltage (not shown here) also rose suddenly for this current and as the power supply voltage reached a preset value (8 V in this case) the current is cut off automatically. Consequently the voltages across the two taps decreased.

The temperature of sample was 15 K at the start of current charging and the temperature linearly increased with current upto $\sim$ 208 A. At this current the sample temperature was 16 K, 1 K above the starting temperature. This increase in temperature is due to the current sharing with resistive matrix and insufficient thermal stability of the composite conductor. The current passing through the normal resistive layers near the current contacts (within the CTL) generates heat. This heat generation at the ends of the composite can cause undesirable quenching of the superconductor at

transport currents much lower than the current it can actually carry. In the present case, at the onset of transition (around 208 A) the sample temperature is 16 K and then there is sudden increase of temperature by $\sim$ 2 K. The sample showed increased temperature even after the current is turned off and the temperature settled at 4 K above the temperature before transition. This shows the sudden quenching and rapid warming of the sample at around the current of 208.4 A.

For the tape sample the rise of temperature was even higher. During the quenching the temperature of the increased from 21 K to 42 K!. This is above the transition temperature of MgB_2. One thing here to suspect is whether the observed I_C is a true critical current of the sample or a reduced one due to the temperature increase (insufficient cryostability). These results clearly shows the insufficient thermal stability of the prepared multifilamentary MgB_2 conductors. For the practical use of multifilamentary MgB_2 conductors the thermal stability has to be ensured and there is a great need for further research to address this issue. As observed earlier for the above wire and tape samples the relative area of MgB_2 core is $\sim$ 10% and the area of Cu thermal stabilizer is $\sim$ 8%. The low thermally and electrically conducting Fe and Ni occupy a significant percentage of the area of the crosssection ($\sim$ 82%). This is the reason for the in sufficient thermal stability of the conductures. Future research must be focussed on increasing the Cu and MgB_2 area fraction without sacrifising the strength and quality of the conductor.

4.8 Preparation and characterization of MgB_2 conductors by electrical self-heating

In the electrical self-heating method sheathed MgB_2 conductors were prepared by heating the conductor using electric current (either DC or AC), instead of the regular furnace heating. For the electrical self-heating method, mono filamentary wires/tapes were rolled as described in section 4.3. These fabricated wires were then subjected to electrical self-heating by employing a DC current source (Voltage : 0-20 V, Current : 0-30 A).

4.8.1 Experimental details

For a typical sample preparation wire sample of length about 50 cm was held horizontally through the axis of a tubular thermal insulator (inside

diameter: 2.5 cm) fabricated from alumina fiber board and the ends of the sample were connected to the current source through a programmable temperature controller, a thermocouple which was kept at the middle of the sample to monitor the temperature. The sample was heated by passing a suitable current through the sample, either manually or automatically through a PC interface. A schematic diagram of the set up used for electrical self-heating is shown in figure 4.25. Figure 4.26 shows the photograph of the set up used to electrically self-heat samples of length 10-30 cm in air. The thermal insulation is removed for clear visibility of the sample.

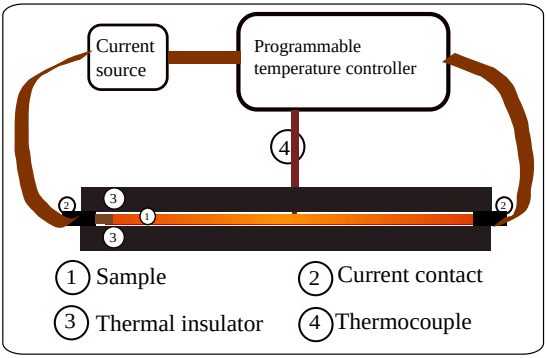

Figure 4.25: Schematic diagram of the preparation of MgB_2 conductors by electrical self-heating method.

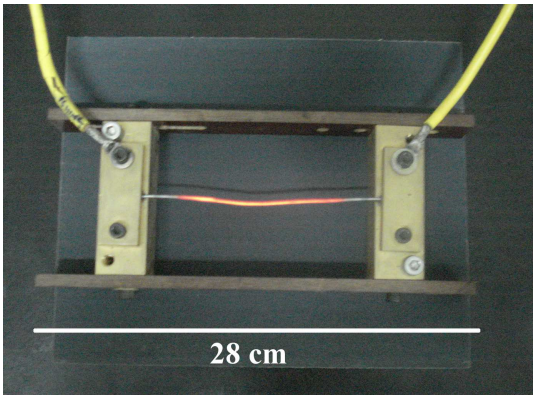

Figure 4.26: Photograph of electrical self-heating of a MgB_2 conductor.

4.8.2 Results and discussion

The results of two monofilamentary wire samples, SW1 with OD = 1.1 mm and length = 40 cm and SW2 with OD = 1.6 mm and length = 25 cm are discussed here. For both the samples the Fe sheath to MgB_2 area fraction is around 80:20. The sample SW1 was heated at 750 °C for 15 minutes and SW2 was heated at 700 °C for 30 minutes. The figure 4.27 shows power schedule for sample preparation for the two typical cases. For SW1 the energy required for one typical experiment is estimated to be about 60 Whr only, of which about 30 Whr (7 V $\times$ 17 A $\times$ 0.25 hr) is used for soaking for 15 minutes and 30 Whr is used for controlled heating and cooling. The time required for one experiment is typically 45 minutes. For SW2, the total energy required is about 70 Whr, of which $\sim$ 45 Whr is used for soaking at 700 °C for 30 minutes and the remaining 25 Whr is equally shared for heating and cooling. The total time taken for SW2 is one hour. Evidently, the ESH method is highly energy efficient since the electric power is used only for heating the sample alone.

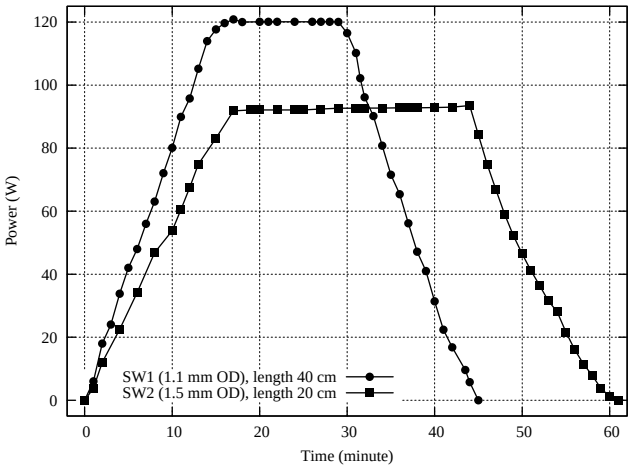

Figure 4.27: Power schedule for typical electrical self-heating experiments.

Figure 4.28 shows the XRD patterns of the wire samples SW1 and SW2 prepared by electrical self-heating method. The XRD patterns reveal that almost phase pure MgB_2 is formed in the samples with very sharp and

strong peaks comparable to that observed in furnace heat treated wire/ tape samples. No peaks of Fe_xB phases are observed here also suggesting that the sintering temperature used here is suitable for the formation of MgB_2 wires with little or no reaction between Fe and the superconductor matrix. Calculated lattice parameters of the prepared MgB_2 were obtained as a = 3.086 $\pm$ 0.002 Å and c = 3.524 $\pm$ 0.001 Å, which are consistent with values observed for bulks and other furnace heat treated conductors.

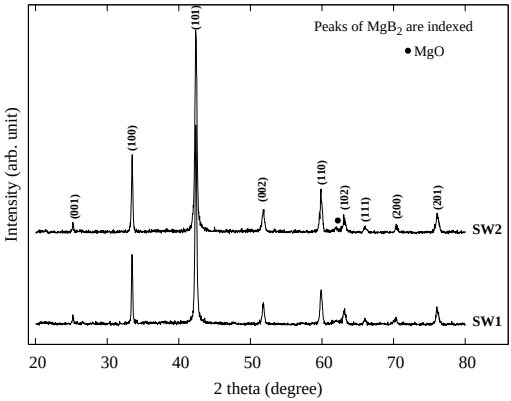

Figure 4.28: XRD spectra of the core of samples prepared by electrical self-heating method.

The T_C of the samples from R-T measurements were found to be 37.90 K and 38.45 K for SW1 and SW2 respectively. The I-V plots at 25 K for the samples are also shown in figure 4.29. The sample SW1 has a relatively low I_C due to its smaller cross section. These transport properties are comparable to those of samples prepared with furnace heat treatment. Thus it is demonstrated for the first time that good quality MgB_2 conductors can be prepared by a simple and energy efficient electrical self-heating method.

The electrical self-heating produces good quality MgB_2 conductors with crystalline and superconducting properties as good as those of furnace heat treated samples. Most of the electrical self-heating synthesis are done with DC power source. However since AC power source is cheaper the use of AC source is also carried out and the results are found to be identical as that of DC power source.

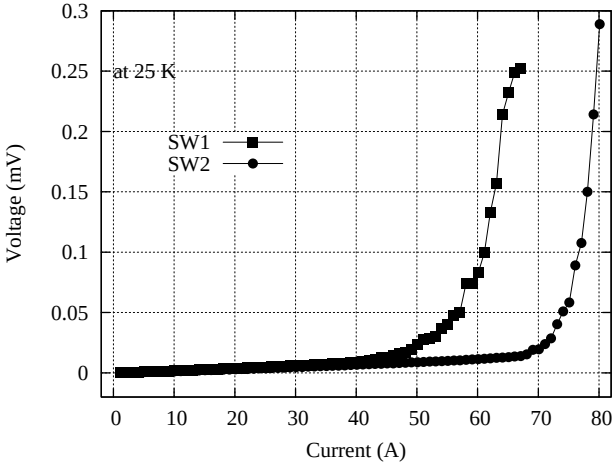

Figure 4.29: I-V plots of samples prepared by electrical self-heating method.

The electrical self-heating method has many advantages such as less power consumption, short preparation time, less preparation cost due to the avoidance of special furnaces with inert gas atmosphere. The method is highly suitable for processes wherein rapid heating or cooling is essential. It is possible to translate the method into a continuous hot rolling process with an array of groove rollers initially for wire making followed by a pair of rollers at the end to which electrical power can be supplied directly. Thus from an industrial point of view the present method is more economical and easy for continuous production of sheathed MgB_2 conductors.

4.9 Summary and conclusions

A systematic study on the chemical computability of different sheath materials with Mg/B is conducted and based on the results of the study, Fe is selected as a suitable sheath material for the MgB_2 wire and tape preparation. Fe sheathed MgB_2 wires tapes were prepared by *in situ* Powder-In-Tube method in mono and multifilamentary geometries. The prepared multifilamentary wires were characterized for phase purity and superconducting properties. The prepared multifilamentary conductors have good transport current carrying, comparable to the internationally reported for

MgB_2 conductors. A simple and energy efficient electrical self-heating method is introduced for the preparation of MgB_2 conductors.

Chapter 5

Enhancement of in-field critical current density of MgB_2 by selective chemical addition

For technological applications of MgB_2 superconductor, enhancement of both the in-field critical current density [$J_C(H)$] and upper critical field (H_{C2}) are essential. MgB_2 has high J_C values in self-field, typically 10^5-10^6 A/cm^2 at 4.2 K and 10^5-10^4 A/cm^2 at 20-30 K [12, 133], however the J_C falls sharply in applied magnetic fields, due to weak flux pinning and low upper critical field (H_{C2}). In the recent years, significant research is being continued and various techniques have been developed for the improvement of flux pinning and hence $J_C(H)$ and H_{C2} of MgB_2. Section 1.9 of chapter 1 discusses these issues.

Lattice defects and inclusions of suitable size can act as intense vortex pinning centers [126] and improves the high field performance of MgB_2 considerably. In MgB_2, since lattice structure is rather rigid and the number of elements in the structure is only two, the density of defects introduced by general preparation procedures is too low to provide effective flux pinning. In pristine MgB_2 flux pinning is mainly provided by grain boundaries. For effective pinning, lattice defects or inclusions can be introduced by a variety of methods like thermo mechanical treatments, irradiation of

high energy particle and chemical doping etc.

Irradiation of high energy radiation introduces atomic scale defects (point or extended) and improves the high field J_C of MgB_2 considerably [127–129]. Though the J_C and H_{C2} increase, the irradiation technique is not easily scalable for large scale production of long length conductors. On the other hand chemical doping is considered to be the most suited and preferred method for the introduction of pinning centers in practical superconductors.

From metallic LTS to cuprate HTS, chemical substitution/addition has been a major approach to improve their superconducting properties. Chemical substitution is easy, favorable for large-scale production compared to other methods used to improve the superconducting properties. Chemical doping, like in other superconductors is an effective and scalable method for modifying the properties of MgB_2. Based on the nature of the dopant, it can cause substituition at Mg/B site, or react with Mg/B to form reacted secondary phases or can be included in the superconductor matrix without any chemical reaction. All these defects can act as flux pinners and can increase the H_{C2} and H_{irr} values and hence enhance the in-field J_C of MgB_2.

The final properties of added MgB_2 depend on the chemical nature of the additive, method of introduction and its distribution in the superconductor matrix. Various nano/submicron particles and materials including metallic elements, carbon (in variuos forms like nanopowders, nanotubes, graphite and diamond), carbides, silicides, nitrides, borides, oxides, and some hydrocarbons have been introduced in MgB_2 (see the recent papers and reviews [84, 85, 130–134] and references therein). These additives improved the flux pinning and $J_C(H)$ of MgB_2 to different extents. The better results are achieved for C based additives like nano C, diamond, graphite, CNT, SiC, B_4C and hydrocarbons [84, 85, 130–134]. This is mainly due to the substitution of C at B site[1] which induces lattice disorders and strains, modifies the σ and π band scattering and enhances the H_{C2} of MgB_2 significantly [69, 181]. Besides the H_{C2} enhancement, the

[1] Numerous attempts were made to substitute other elements for Mg and B in MgB_2. However, MgB_2 has not accepted substitution by other elements except Al, Mn and Sc for Mg site. All these substitutions resulted in a reduction of T_C of MgB_2 without any considerable improvement on J_C.

lattice distortions/defects and strains caused by C substituition improves the flux pinning strength also.

The additives selected for the present work include materials commercially available nano particles of rare earth oxides, nano particles of carbides and a non conventional natural material. The materials studied have quite different chemical and physical properties and reactions with Mg/B system. By the selective doping studies a significant enhancement of high field critical current density by nearly two order of magnitude is achieved in technically useful temperatures and fields.

All the samples were prepared by the *in situ* Powder-In-Sealed-Tube (PIST) method as described in chapter 3. The superconducting characterizations (DC magnetization) of the samples were done using a SQUID or VSM based PPMS in collaboration with RRCAT, Indore and JNCASR, Bangalore. Microstructural analyses were done at NIIST using powder XRD, SEM, TEM and EDS measurements.

5.1 Influence of nano rare earth oxide (Tb_4O_7)

For most of the cuprate based HTS materials addition of rare earth based materials is found to have strong influences on crystalline, microstructural and superconducting properties. Since RE ions are larger than Mg^{2+}, they are likely to increase axis length if they are incorporated in the lattice of MgB_2. From the pressure dependence of axis lengths and T_C of MgB_2, this can increase the T_C [80, 182]. However the substitution of trivalent RE ions for Mg^{2+} can decrease the hole density of states (DOS) at the Fermi level of MgB_2 and can decrease the T_C, as in the case of Al doping (see the extensive review [80] and references therein). Another possible effect of RE doping is a change in critical current density. Although the predominant pinning center in MgB_2 is thought to be grain boundaries, it has been reported that additions of REO introduce REB_4 or REB_6 particles in MgB_2 grains, which would act as pinning centers.

Addition of nano and submicron particles of rare earth oxides (RE oxides) such as Y_2O_3, Dy_2O_3, Ho_2O_3 and Pr_6O_{11} are found to increase the flux pinning in *in situ* MgB_2. Wang *et al* first reported the improvement of $J_C(H)$ of MgB_2 by nano particles of Y_2O_3 addition. The addition resulted precipitates of nearly 10 nm size at the grain boundaries and nearly 3-5 nm

sized precipitates uniformly distributed in the MgB_2 grains, which acted as pinning centers. Followed by this, Chen *et al* reported improved flux pinning using submicron sized Dy_2O_3 as the additive.

Based on these backgrounds, the possibility of RE substitution in MgB_2 is explored, and the influences of REO addition on the lattice parameters, T_C and J_C are also investigated. Nano Tb_4O_7 was chosen as the rare earth oxide and the choice was quite arbitrary.

MgB_2 + x wt.% of nano Tb_4O_7 (where x = 0, 1, 5 and 10) samples were prepared by *in situ* PIST method, using Mg (-325 mesh, 99.8%), amorphous B (-325 mesh, 99%) and nano Tb_4O_7 (< 60 nm, 99.5%) as starting powders and heat treatment at 800 °C for 2 hours. The samples prepared with 0, 1, 5 and 10 wt.% of Tb_4O_7 are named as MBTB0, MBTB1, MBTB5 and MBTB10 respectively.

5.1.1 Results: Superconducting properties

Figure 5.1 shows the field dependence of magnetic J_C [$J_C(H)$] of the samples at 5 K, deduced from M-H data. At lower fields the estimation of J_C is not accurate due to flux jumps. The $J_C(H)$ is enhanced for all the added samples compared to the undoped sample for the entire field of study. At low fields the improvement in $J_C(H)$ is higher for samples with lower amounts of Tb_4O_7 addition, but at higher fields the sample with higher amount of Tb_4O_7 addition show better $J_C(H)$ performance. As shown in the table 5.1, at 5 K and 6 T the J_C of undoped sample is 1.6×10^3 A/cm^2, while it is 2.6×10^3 A/cm^2 for the 10 wt.% Tb_4O_7 added sample. The H_{irr}, determined by the linear extrapolation to zero for the high field low J_C segments of the Kramer curves is also improved for the added samples, as shown in table 5.1. At 5 K the H_{irr} value of undoped sample is 7.5 T, while for the 10 wt.% Tb_4O_7 added sample it is 8.1 T.

Table 5.1: Superconducting properties of the nano Tb_4O_7 added samples.

Sample	T_C	J_C at 5 K (A/cm^2)		H_{irr} at 5 K
	(K)	3 T ($\times 10^4$)	6 T ($\times 10^3$)	(T)
MBTB0	38.6	4.6	1.6	7.5
MBTB1	38.8	6.6	2.4	7.9
MBTB5	38.5	6.9	2.5	7.9
MBTB10	38.6	5.5	2.6	8.1

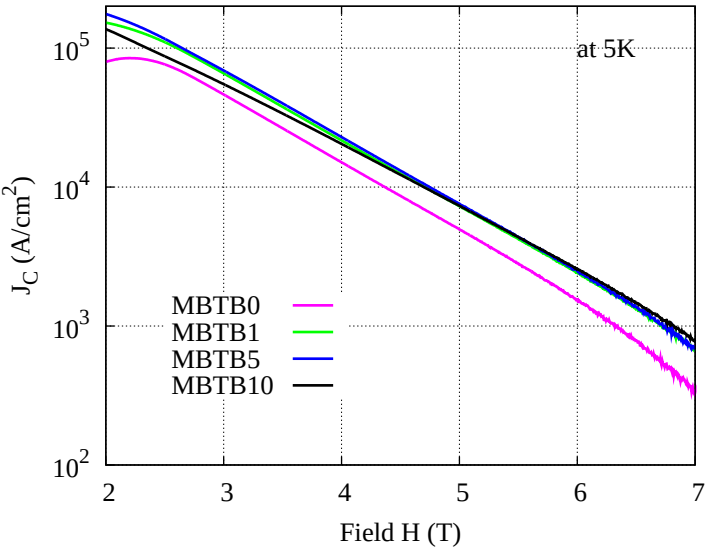

Figure 5.1: $J_C(H)$ curves of nano Tb_4O_7 added samples.

The normalized flux pinning force density F_P/F_{Pmax}, where $F_P = J_C(H) \times \mu_0 H$) as a function of applied magnetic field is plotted in figure 5.2. The flux jumps at low fields have marks on the shape of these curves also. From the figure it is clear that the added samples have enhanced flux pinning compared to the undoped sample. However the sample MBTB1 showed the maximum of F_P/F_{Pmax} at higher fields and the peak position of F_P/F_{Pmax} of MBTB10 is at comparatively lower fields. But at higher fields the F_P/F_{Pmax} of MBTB10 is higher compared to all other samples. This discrepancy in the position of maximum of F_P/F_{Pmax} may be related to the grain connectivity problems and consequent reduced J_C in low and medium fields in MBTB10 as seen in the $J_C(H)$ plots. The improvement in $J_C(H)$ in higher fields and H_{irr} of the added samples is due to the enhancement in flux pinning caused by the nano particle addition.

Zero field cooled (ZFC) magnetization plots in the temperature range 5 to 50 K, taken at 20 Oe are shown in figure 5.3. The samples show sharp superconducting transition with T_C around 38.6 K and $\Delta T_C < 1$ K. No considerable variation of T_C is observed for the added samples, indicating

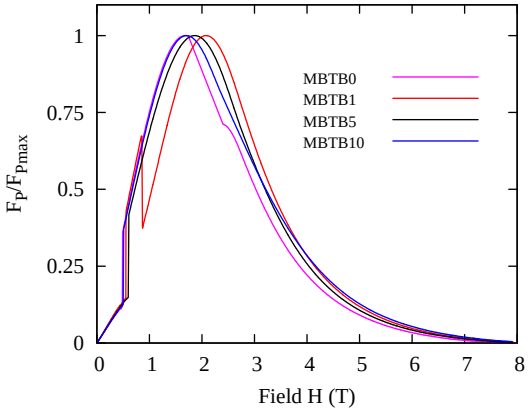

Figure 5.2: Normalized flux pinning force density versus applied magnetic field for nano Tb_4O_7 added samples.

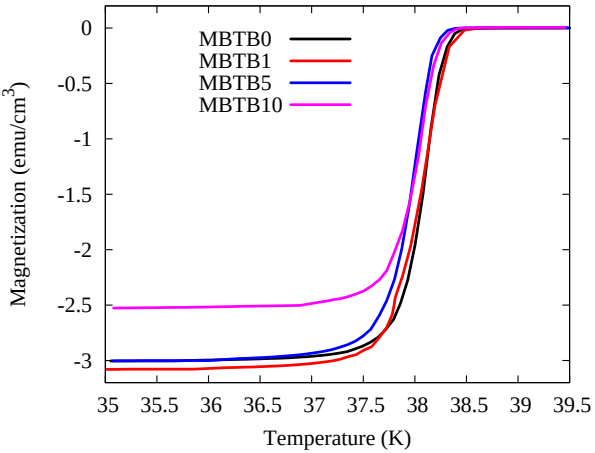

Figure 5.3: ZFC M-T plots of nano Tb_4O_7 added samples, taken at 20 Oe field.

that the RE is not substituted either at Mg or B site. The consistently T_C and small ΔT_C values show that the samples are of high quality and identical with respect to stoichiometry, lattice strains and the electronic states in the superconducting B planes.

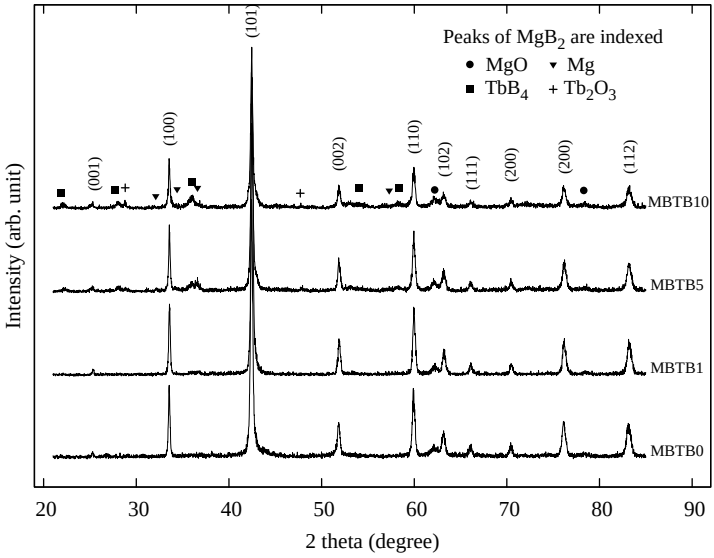

Figure 5.4: Powder XRD patterns of nano Tb_4O_7 added samples.

5.1.2 Results: Structural properties

Figure 5.4 shows the XRD patterns of MgB_2 with different amounts of Tb_4O_7 additions, heat treated at 800 °C for 2 hours. MgB_2 is the main phase, with a trace amount of MgO, observed in all the samples. No Tb_4O_7 is observed even for the 10 wt.% addition. TbB_4 and Tb_2O_3 are found, in increasing amounts with increasing Tb_4O_7 additions, in all the added samples. The peak intensities of MgB_2 are reduced in added samples, indicating that the undoped sample has better phase purity and crystallinity. The presence of TbB_4 and Tb_2O_3 indicates that some of the added Tb_4O_7 decomposed and reacted with B at the heat treated temperature. Also for other RE oxide additions in MgB_2, their respective borides (YB_4, DyB_4, HoB_4 and PrB_6 in Y_2O_3, Dy_2O_3, Ho_2O_3 and Pr_6O_{11} additions, respectively) are formed and their amounts are found to increase with the increase of added RE oxides [146–149]. The volume percentage of MgO in the samples is assessed from the Xray peak intensities and the values are 1.5, 1.8, 2.5 and 3.6 % for MBTB0, MBTB1, MBTB5 and MBTB10 respectively.

Table 5.2: Structural parameters nano Tb_4O_7 added samples.

Sample	*a*	*c*	FWHM (degree) of the peaks		Density
	(Å)	(Å)	(002)	(110)	gcm^{-3}
MBTB0	3.0863	3.5196	0.2843	0.3160	1.32
MBTB1	3.0866	3.5152	0.2986	0.3512	1.41
MBTB5	3.0824	3.5229	0.2784	0.3090	1.47
MBTB10	3.0837	3.5254	0.2647	0.2300	1.46

The *a* and *c* lattice parameters, calculated from the XRD data, for a hexagonal crystal structure, is given in table 5.2. The maximum standard deviation for *a* is 0.002 and for *c* is 0.003. The value of *a* decreases slightly and *c* increases slightly with the addition. However the very small change in the lattice parameters may be due to the strain induced by the nano particles, rather than a substitutional effect or structural change, as suggested by Wang *et al* [147] for the Y_2O_3 addition. The FWHM of (002) and (110) peaks of the samples are shown in table 5.2. The maximum variations in the FWHM values are $\pm$ 0.008 degrees. FWHM of both the peaks decreases significantly with doping, except for the samples MBTB1. For MBTB1 the FWHM of both the peaks are significantly larger compared to other samples. The sample showed finer and lower sized grains in the SEM image, which is in agreement with this FWHM values. Lattice strains, resulted from the nano particle addition also have contributions to the significant increase of FWHM of the sample. The geometrical density, also shown in table 5.2, of the samples improved with Tb_4O_7 addition. Undoped sample showed the minimum density with only 50 % of the theoretical density of MgB_2.

Figure 5.5 shows the secondary electron SEM images of the fractured surfaces of the samples. All the samples show randomly oriented hexagonal MgB_2 grains of varying size. The homogeneity of microstructure is more for undoped sample, and it decreases with increase of Tb_4O_7 addition. Undoped sample has grains of average size < 1 μm. Sample MBTB1 show much finer grains, and this is in agreement with the FWHM results. For samples with higher amounts of additions the grain size increases with increasing Tb_4O_7, which is also in agreement with the FWHM results. Some less crystallized (amorphous like) regions are observed in the added samples, which increased with increasing amounts of Tb_4O_7.

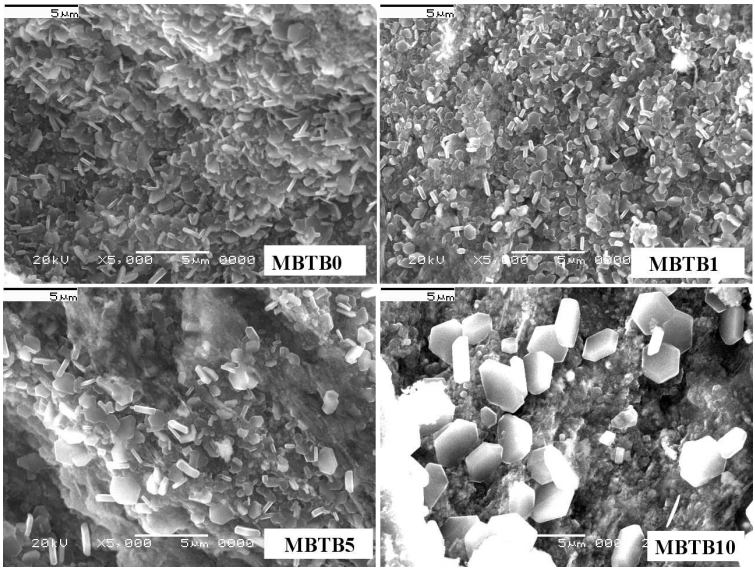

Figure 5.5: SEI SEM of nano Tb_4O_7 added samples.

5.1.3 Discussion of the results

The $J_C(H)$ is enhanced for all the added samples, but differently at low and high fields. The $J_C(H)$ behavior of the samples can be explained in terms of grain connectivity and flux pinning, due to the addition. From figures 5.4 and 5.5 (XRD and SEM) it is clear that the undoped sample has better phase purity, crystallinity and homogeneity in the microstructure. So the observed enhancement in flux pinning and the superconducting properties cannot be attributed to any improvement in any of the above quantities. In MgB_2, grain boundaries are strong flux pinners and therefore reduction of grain size improves flux pinning and hence improves the superconducting properties [122, 125]. Finer grains are observed for samples MBTB0 and MBTB1 (undoped and 1 wt.% of Tb_4O_7 added sample). However the observed enhancement in J_C at higher fields is for the samples added with higher amounts of Tb_4O_7. These samples have less homogeneous microstructure and much bigger grain size.

As observed in the XRD patterns the amount of reacted phases such as TbB_4, Tb_2O_3 and MgO are higher in higher amount of Tb_4O_7 added sam-

ples. These phases can be within the MgB_2 matrix and at the grain boundaries. The increased MgO reduces J_C in low magnetic fields, but improves the J_C in higher magnetic fields [183, 184]. The increased amounts of reacted phases such as TbB_4, Tb_2O_3 and MgO at the grain boundaries reduce grain connectivity and low field J_C, while these secondary phases act as strong flux pinners at higher fields. This is why the sample MBTB10 showed reduced $J_C(H)$ in low fields compared to MBTB1 and MBTB5, but improved $J_C(H)$ in higher fields among the added samples. Thus in the nano Tb_4O_7 added samples the addition induced secondary phases affects the grain connectivity and flux pinning, and the enhanced flux pinning is the reason for the enhancement in the $J_C(H)$ and H_{irr} of the added MgB_2 samples.

5.1.4 Conclusion of the addition

Nano Tb_4O_7 addition is found to be effective in improving the flux pinning properties of MgB_2, without affecting the T_C of the system. Better high field $J_C(H)$ is observed for 10 wt.% of Tb_4O_7 added MgB_2. The added nanoparticles and the addition induced normal particles act as strong flux pinners and this is the reason for the improvement in the $J_C(H)$ of the added samples. Though the nano Tb_4O_7 addition improved the $J_C(H)$, from a practical point of view the improvement is only moderate. So it has become necessary to explore other categories of additives.

5.2 Effect of carbon substitution using nano SiC

Since the effect of nano REO on improving $J_C(H)$ was only moderate, application of other categories of additives became necessary. Considering the significant improvement of $J_C(H)$ by C based additives nano SiC was chosen as the next additive. The benefit of nano SiC as an additive is first reported by Dou *et al* [142] and is confirmed by many groups worldwide.

MgB_2 + x wt.% of nano SiC (where x = 0, 2, 5, 10 and 15) samples were prepared by *in situ* PIST method, using Mg (-325 mesh, 99.8%), amorphous B (-325 mesh, 99%) and nano SiC (< 100 nm, 97.5%) as starting powders and heat treatment at 800 °C for 2 hours. The samples prepared with 0, 2, 5 and 10 wt.% of SiC are named as S 00, S 02, S 05, S 10 and S 15 respectively.

5.2.1 Results: Superconducting properties

Figure 5.6 shows temperature dependences of zero-field cooled magnetization for the undoped and SiC added samples in an external field of 100 Oe. Inset of the figure shows plots near the transition region. T_C is defined as the onset temperature at which the samples exhibit diamagnetic properties and the measured values of T_C are tabulated in table 5.3. It is observed that the undoped sample has a T_C of 38.5 K, which decreases systematically with increasing percentage of added SiC and the minimum T_C obtained for heavily added sample is 35.3 K. The width of superconducting transition, ΔT_C of the samples (table 5.3) is found to increase systematically with increasing addition of SiC. This can be attributed to C substitution which reduces crystallinity of the B planes.

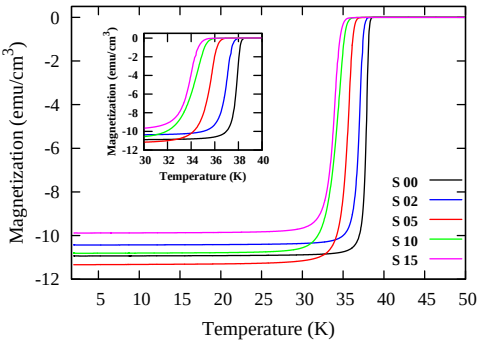

Figure 5.6: ZFC M-T plots of nano SiC added samples, taken at 100 Oe field.

The field dependence for J_C, calculated from magnetization using the Bean model, at 5 K and 15 K are illustrated in figure 5.7. At 5 K, J_C jumps abruptly at low fields where the estimation of J_C may not be accurate due to the flux jump. $J_C(H)$ behavior of all added samples is significantly enhanced with respect to the pure sample and it is the best for samples S 10 and S 15 at higher fields. Compared to the undoped sample J_C for 10 wt.% added sample increases by one order at 5 K and > 6 T and at 15 K and 6 T. J_C values for the same sample (S 10) are 5.4×10^3 A/cm^2 at 5 K and 8 T and 1.8×10^3 A/cm^2 at 15 K and 6 T. At higher levels of addition the $J_C(H)$ shows a saturating tendency with almost same behaviuor for S 10 and S 15. The J_C enhancement indicates that addition of SiC increases

the amount of pinning centers with respect to the undoped sample.

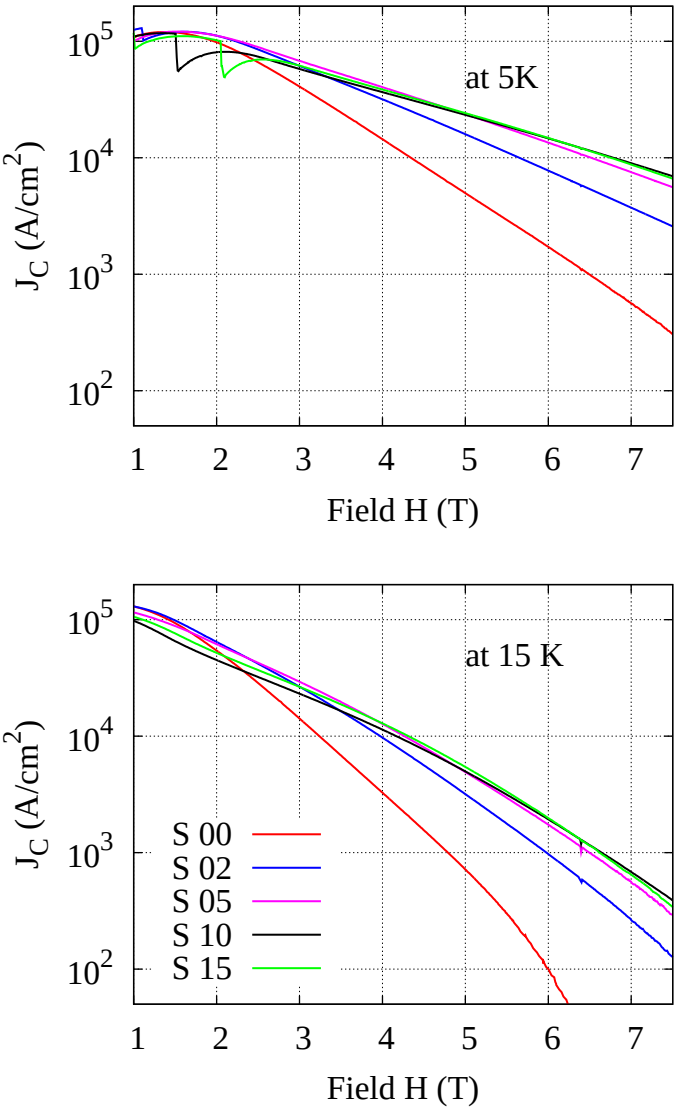

Figure 5.7: $J_C(H)$ curves of nano SiC added samples.

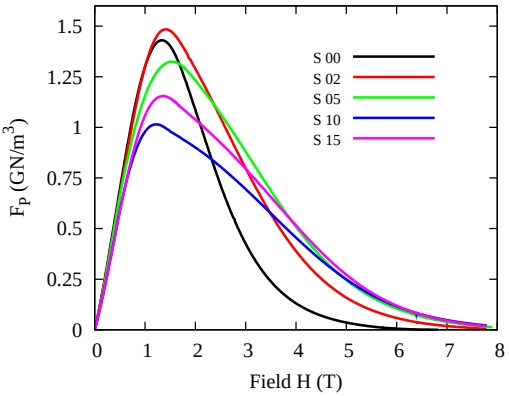

Figure 5.8: Flux pinning force density versus applied magnetic field at 15 K for nano SiC added samples.

The value of H_{irr}, determined from the Kramer's curves for the samples is shown in table 5.3. The value of H_{irr} is higher for the nano SiC added sample both at 5 K and 15 K. Figure 5.8 plots the field dependence of the volume pinning force, $F_P = J_C \times H$, of the samples at 15 K. At higher fields the nano SiC added samples have significantly higher F_P values compared to the undoped sample.

Table 5.3: Superconducting properties of the nano SiC added samples.

Sample	T_C	ΔT_C	J_C ($\times 10^3$ A/cm^2) at 5 T		H_{irr} (T) at	
	(K)	(K)	5 K	15 K	5 K	15 K
S 00	38.5	1.1	4.9	0.7	8.0	6.0
S 02	38.1	1.4	15.7	3.2	9.6	7.4
S 05	37.2	2.1	23.5	4.9	10.5	8.1
S 10	36.1	2.3	23.6	5.3	11.2	8.5
S 15	35.3	2.5	23.2	5.4	11.1	8.3

5.2.2 Results: Structural properties

Powder XRD analysis of pure and SiC added MgB_2 samples shows that the undoped sample consists of single phase of MgB_2 with a trace of MgO as shown in figure 5.9. Peaks of two secondary phases Mg_2Si and SiC are also

observed in the added samples. Quantitative phase analysis of the samples was also done from XRD data and corresponding volume percentage of MgB_2, Mg_2Si, SiC and MgO are tabulated in table 5.4. It is found that increasing the SiC doping level resulted increasing the relative amount of non superconducting phases such as Mg_2Si and SiC in added samples. This indicates that some of the added SiC dissociated into Si and C, and the Si reacted with Mg to form Mg_2Si while the C is incorporated into the MgB_2 lattice. No compounds of C with Mg or B are observed in the XRD.

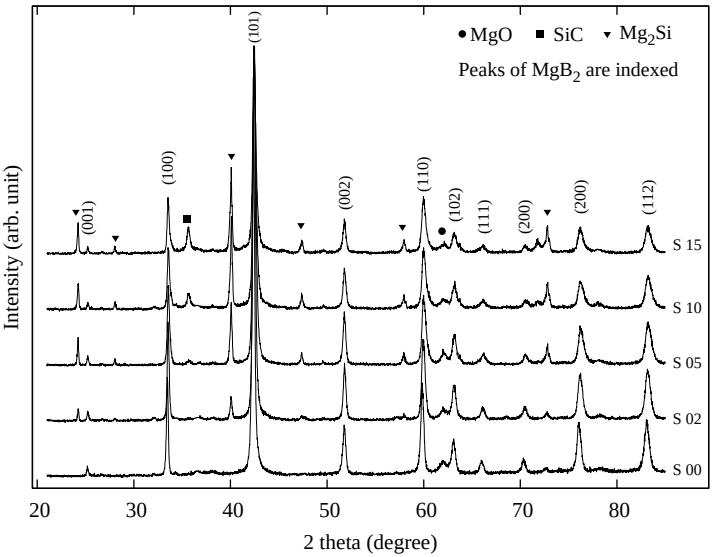

Figure 5.9: Powder XRD patterns of nano SiC added samples.

The lattice parameters *a* and *c* were calculated and the results are shown in figure 5.10. The lattice parameter *a* falls sharply for S 02 and S 05 samples and then shows nearly saturating behavior for S 10 and S 15 but no systematic change was observed in the *c* lattice parameter. The systematic shrinkage of *a* axis with increasing SiC doping is caused by carbon substitution for boron. It is to be noted that the presence of unreacted SiC is higher for S 10 and S 15 which also implies a nearly saturated behavior of C substitution in the MgB_2 lattice.

Table 5.4: Volume percentages of different phases observed in nano SiC added samples.

	Volume percentage of (%)			
Sample	MgB_2	MgO	Mg_2Si	SiC
S 00	98.27	1.73	0	0
S 02	91.00	1.37	6.62	0.98
S 05	78.78	1.35	16.79	3.07
S 10	70.92	1.37	22.28	5.43
S 15	64.88	1.31	26.05	7.75

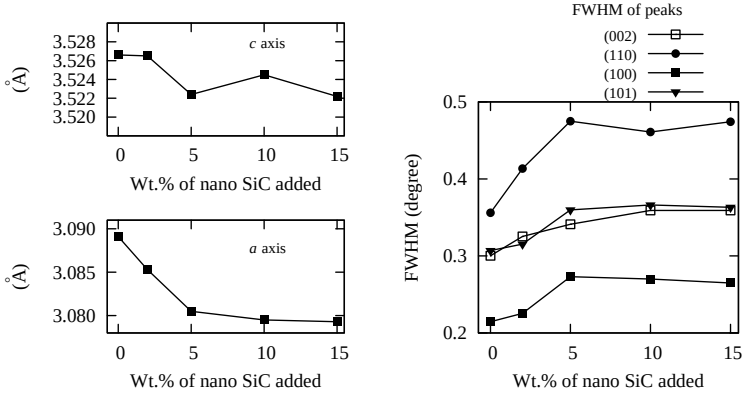

Figure 5.10: Lattice parameters and FWHM of the nano SiC added samples.

Figure 5.10 also shows the variation of full width at half maximum (FWHM) of (100), (101), (002) and (110) peaks of all samples. The data shows a clear and systematic trend with doping. The FWHM of the *(00l)* planes has hardly any effect but the FWHM of *(hk0)* is the most affected. It can be seen that the values of the FWHM increase gradually up to 5 wt.% of SiC and show a saturating tendency for the heavily added added samples similar to the variation of *a* axis length. Both the observed results on *a* axis variation and the FWHM of *(hk0)* are in accordance with most of the works reported on the doping studies of SiC or C or other C based additives and is due to the C substitution at B sites.

In the hexagonal structure *p*6/*mmm*, Mg atoms occupy the 1a site (0,0,0) and the B atoms at the 2d site $(\frac{1}{3},\frac{2}{3},\frac{1}{2})$. The reported works demonstrate

that C atoms preferentially occupy at the 2d site [69, 185]. This results in the contraction of inplane lattice, since the covalent radii of C is lower than that of B and the availability one extra electron. The lattice strains consequent to the C substitution at B site is responsible for the increased FWHM of the SiC added samples. The reduction of grain size as evidenced from the SEM images can also contribute to the increase of FWHM.

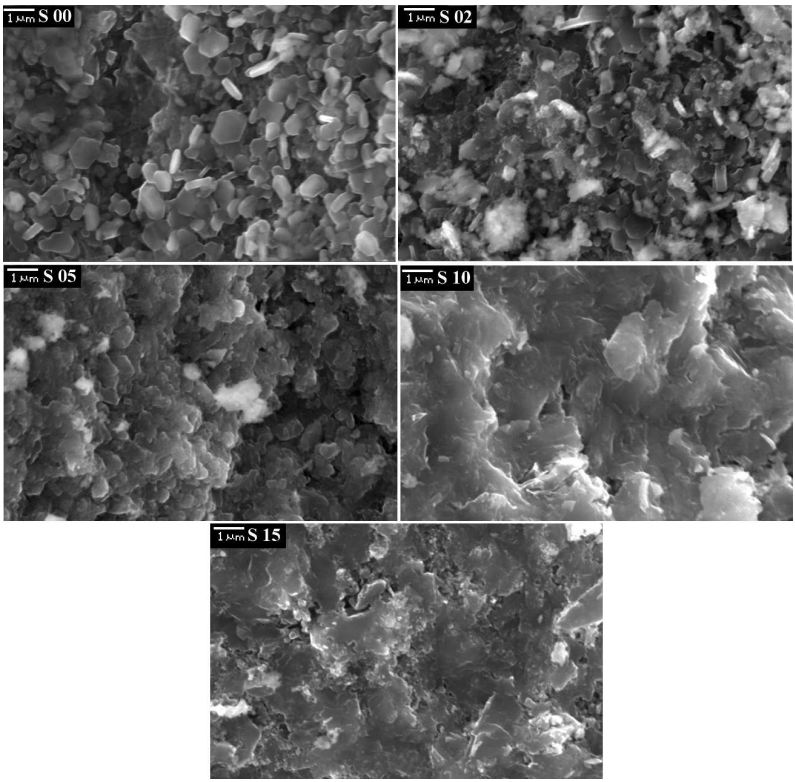

Figure 5.11: SEI SEM of nano SiC added samples.

Figure 5.11 shows the secondary electron SEM images of the fractured surfaces of the undoped and added samples. The undoped sample shows a homogeneous microstructure with tiny and well packed hexagonal grains of average size 1 μm wherein the grain boundaries are sharp and clear. As the level of SiC increases the sharpness of MgB_2 grain boundaries loses

and the grains become finer. The samples added with 10 and 15 wt.% of SiC show significant difference in microstructure in comparison with pure sample. The samples show a molten like grains without sharp grain boundaries. The presence of large quantity of impurity phases in the system possibly reduces the reaction temperature leading to the formation of molten-like grains in heavily added samples. Although the role of SiC for the formation of these molten-like grains is not fully understood at this stage, its clarification may give some insight into the importance of SiC in MgB_2.

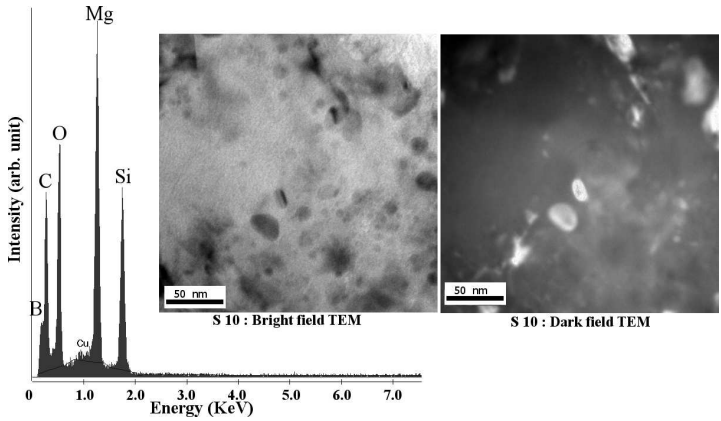

Figure 5.12: Bright and dark field TEM images and EDS spectrum of 10 wt.% of nano SiC added sample.

Typical bright and dark field TEM images of S 10 sample are shown in figure 5.12 and EDS analysis of same sample also given in the image. The images show nano scale inclusions (10-20 nm) within the MgB_2 grains. These uniformly distributed nano size impurities with size comparable to the coherence length of MgB_2 can pin the flux lines within the grains. EDS analysis of the selected area confirms the presence of Mg, B, C, Si and O. Analyses of XRD and EDS results suggest that the nano particles within the grains are Mg_2Si and SiC. These provide effective pinning at all the temperature up to T_C.

5.2.3 Discussion of the results

The addition of nano SiC is found to be very effective in improving the high-filed J_C of MgB_2. The enhancement of J_C is so strong that the values of J_C is enhanced by more than one order of magnitude at higher fields and temperatures. The enhancement of $J_C(H)$ by nano SiC can be explained by the dual reaction model proposed by Dou *et al* [131].

According to the dual reaction model [131], the nano scale SiC reacts with Mg at a temperature as low as 600 °C to form Mg_2Si, at the same time releases free atomic scale C as described by the reaction.

$$SiC + 2Mg = Mg_2Si + C$$

The formation of MgB_2 begins to take place at round this temperature and the highly reactive and free C can be easily incorporated into the lattice of MgB_2 via the reaction

$$Mg + (2\text{-}x)B + xC = MgB_{2-x}C_x$$

As a consequence of the dual reaction taking place at around the formation of MgB_2, better C substitution takes place as well as the secondary phases such as Mg_2Si, SiC or C and other Mg-B-Si-C-O precipitates can be effectively embedded within the grains as nano inclusions. The substitution of C at B site at the time of formation of MgB_2 may reduce the grain growth, resulting finer grains and hence increased grain boundary pinning centers.

The substitution of C at B site is evidenced by the reduction of T_C, decrease of *a* axis and in the variation of in-plane FWHM values. The reduction of grain size is observed in the SEM images as well as observed in the increased FWHM values. The nano scale inclusions are clearly observed in the TEM images also. Substitution of C at B modifies the σ and π bands of MgB_2 and hence their scattering rates. The H_{C2} of MgB_2 is strongly depended on σ and π band scattering rates (both inter and intra scattering), and the value of H_{C2} in MgB_2 enhances significantly upon tuning of the scattering rates. Thus the improvement of H_{C2} and better pinning by the nano inclusions are the reasons for the observed significant improvement in the $J_C(H)$ performance of nano SiC added samples. At higher levels of SiC addition both the C substitution level (as indicated in *a* and FWHM

values) and the $J_C(H)$ shows some saturation tendency, may be indication that C substitution has a major role than the nano inclusions on the $J_C(H)$.

5.2.4 Conclusion of the addition study

Nano SiC is found to be a suitable additive for improving the high-field J_C of PIST MgB_2 significantly. Strong enhancement of $J_C(H)$ of the order of more than one order were observed for SiC added samples at higher fields and temperatures. The addition of SiC caused considerable C substitution at B site, which is responsible for the strong $J_C(H)$ improvements. Additional pinning centers are provided by the nano scale inclusions of reaction induced secondary phases.

5.3 Effect of burned rice husk (BRH): An alternative for nano SiC

Considering the significant improvement in $J_C(H)$ by nano SiC addition, burned rice husk (BRH) is explored as an alternative low cost replacement for the costly nano SiC. BRH is a nonconventional raw material of SiC which contains ultra fine amorphous silica (SiO_2) and carbon [186–188]. The ratio of SiO_2 to C in BRH can be controlled by controlling the burning temperature of rice husk. The presence of amorphous SiO_2 in a matrix of friable carbon, easy availability and low cost make BRH a promising dopant for MgB_2.

The BRH used for addition was prepared by heating the raw rice husk in air at 300 °C for 1 h. Figure 5.13 shows the EDS spectrum of the BRH powder, which shows C ($\sim$ 65 at.%), Si ($\sim$ 25 at.%) and O ($\sim$ 10 at.%) elements in the sample. Inset of the figure shows the powder XRD spectrum of the BRH powder which shows only a broadened peak of SiO_2, indicating its amorphous nature.

MgB_2 + x wt.% BRH (where x = 0, 5, 10 and 15) samples were prepared by *in situ* PIST method, using Mg (-325 mesh, 99.8%), amorphous B (-325 mesh, 99%) and BRH as starting powders and heat treatment at 800 °C for 2 hours. The samples prepared with 0, 5, 10 and 15 wt.% of BRH are named as BRH 00, BRH 05, BRH 10 and BRH 15 respectively.

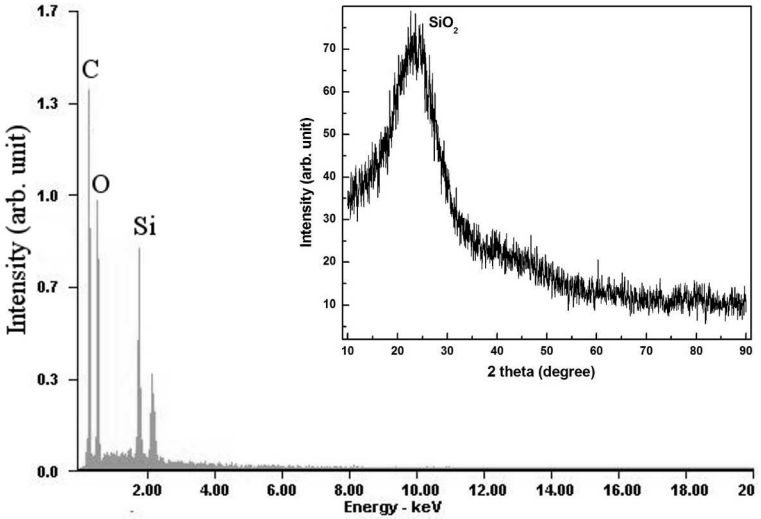

Figure 5.13: EDS spectrum of the BRH powder used for the addition. Inset shows the XRD pattern of the same.

5.3.1 Results: Superconducting properties

The field dependence of J_C calculated from magnetization loops at 5 K is illustrated in figure 5.14. J_C jumps abruptly at low fields ($\sim$ 1 T) due to the flux jump. The BRH added MgB_2 samples show enhanced J_C vales at higher applied fields, compared to the pure MgB_2. Of all the added samples the 5 wt.% BRH added sample gives the best performance and the level of J_C enhancement in high magnetic fields is very similar to that of the J_C increase exhibited by nano SiC addition. For the undoped sample J_C drops rapidly in the presence of magnetic field but for BRH added samples J_C values at higher fields increase by more than an order of magnitude. For example the J_C for 5 wt.% added sample increases by a factor of 40 at 5 K and 8 T as compared to the undoped sample. For the 15 wt.% BRH added sample $J_C(H)$ is higher only for fields above 6 T, and below 6 T the sample showed low J_C values compared to the sample BRH 00. This is due to the higher amount of impurities and cosequent reduced grain connectivity of the sample, as explained later in the coming sections of this chapter.

ZFC magnetization measurements for the samples in an external field of 20 Oe is shown if figure 5.15 and the measured values of T_C are tabulated

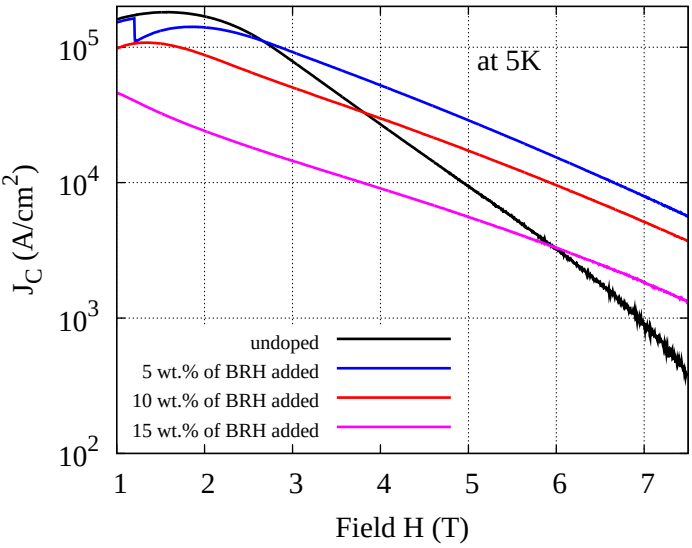

Figure 5.14: $J_C(H)$ curves of BRH added samples.

in table 5.5. It is observed that the undoped sample has a T_C of 38.51 K $\pm$ 0.01 K, which decreases systematically with increase in dopant level and the minimum T_C obtained for heavily added (15 wt.%) sample is 35.88 K. This is due to C substitution at boron sites which is consistent with the observed results on variation of *a* parameter. The superconducting transition width for a 10% to 90% drop (ΔT_C) is found to be increasing with increasing BRH addition (table 5.5).

Table 5.5: Superconducting properties of BRH added samples.

Sample	T_C	ΔT_C	J_C at 5 K (A/cm^2)		H_{irr} at 5 K
	(K)	(K)	3 T ($\times 10^4$)	6 T ($\times 10^3$)	(T)
BRH 00	38.51	0.45	7.9	3.2	7.9
BRH 05	37.71	0.52	9.2	15.3	10.3
BRH 10	36.54	1.71	5.1	9.5	10.2
BRH 15	35.88	3.64	1.5	3.3	11.0

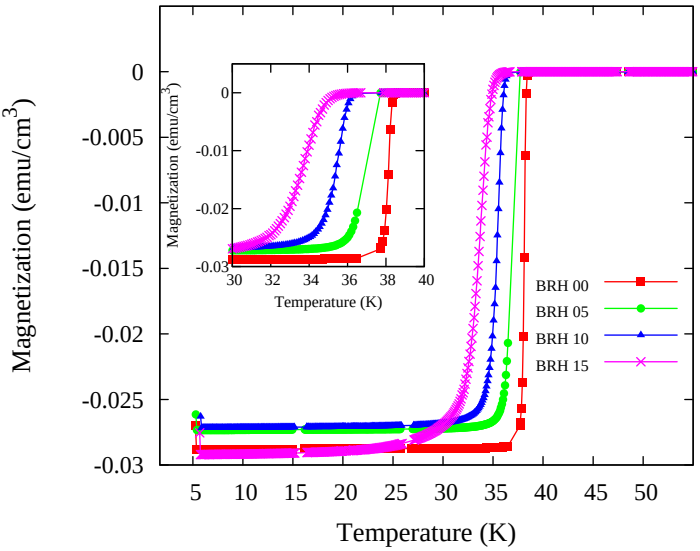

Figure 5.15: M-T plots of BRH added samples.

5.3.2 Results: Structural properties

Figure 5.16 shows the XRD patterns of MgB_2 samples with different levels of BRH addition. The undoped sample consists of mainly MgB_2 phase with a trace of MgO whereas peaks of secondary phases such as Mg_2Si, Mg_2C_3 and MgO are observed in the added samples. Quantitative phase analysis of the samples was done from XRD data and corresponding volume percentage of MgB_2, Mg_2Si, Mg_2C_3 and MgO are tabulated in table 5.6. On increasing the BRH doping level, the relative amounts of non superconducting phases such as Mg_2Si, Mg_2C_3 and MgO are found to be increasing. One aspect here to notice is the significant increase of MgO phase as a result of the BRH addition. This is due to the additional oxygen available in the BRH to react with Mg. X-ray analysis of BRH shows a broadened peak of amorphous silica (figure 5.13 inset). From the above results, it is clear that in the added samples SiO_2 and C contained in BRH reacted with Mg to form Mg_2Si and Mg_2C_3 respectively and the remaining oxygen reacted with Mg to form MgO.

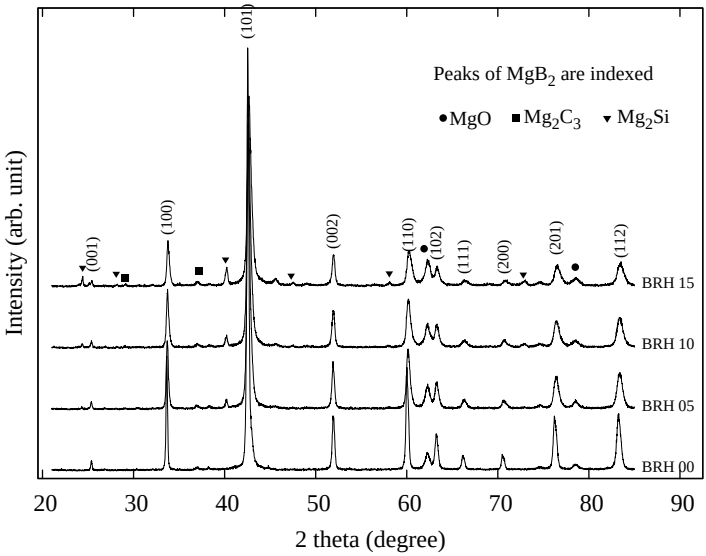

Figure 5.16: Powder XRD patterns of BRH added samples.

Table 5.6: Volume percentages of different phases observed in BRH added samples.

	Volume percentage of (%)			
Sample	MgB_2	MgO	Mg_2Si	Mg_2C_3
BRH 00	96.0	4.0	0	0
BRH 05	92.5	5.5	2.4	0.6
BRH 10	88.5	6.0	4.7	3.8
BRH 15	80.2	7.8	9.6	2.4

The lattice parameters *a* and *c* of the hexagonal MgB_2 have been calculated and their variations with respect to BRH doping level are shown in figure 5.17. There is a systematic decrease of *a* axis with increase in the dopant level. Value of *c* axis remains almost unchanged by the BRH addition. The systematic shrinkage of *a* with increasing BRH doping is caused by carbon substitution for boron and is explained in the preceding sections.

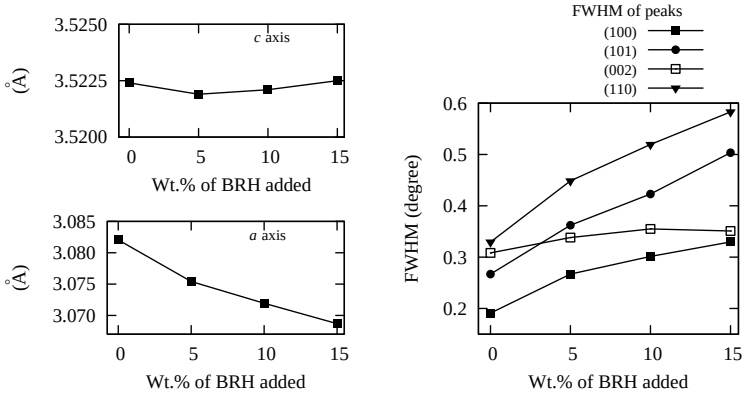

Figure 5.17: Lattice parameters and FWHM of BRH added samples.

Figure 5.17 also shows the full width at half maximum (FWHM) of (100), (101), (002) and (110) peaks of the samples. It is seen that the values of the FWHM sharply vary from pure to added samples except for (002) peak. Because (100) and (110) planes reflect the nature of in-plane honeycomb boron lattice, the broadening of these peaks suggests the occurrence of some distortion in the lattice due to C substitution at B sites. This result is consistent with the earlier reports in which the FWHM of these peaks has a positive correlation with the irreversible field (H_{irr}) of MgB_2, ie H_{irr} increases with increasing FWHM [125, 189].

The microstructure of the samples was significantly affected by the BRH addition. Figure 5.18 shows the SEI SEM images of the fractured surfaces of the samples. The sample BRH 00 shows hexagonal faceted grains of average size about 1 μm, typical of MgB_2 grains. The sample BRH 05 also shows a similar microstructure with faceted grains. The samples BRH 10 and BRH 15 shows some distinct change in microstructure. These samples have a considerable area of impurity like regions and less connected grains. Figure figure 5.19 shows a high resolution TEM image and the corresponding EDS of 5 wt.% BRH added sample. In the TEM image, uniformly distributed nanoinclusions (10-20 nm) are clearly visible within the grain. EDX analysis revealed that the grain contains Mg, B, C, Si and O in accordance with the Mg_2Si, Mg_2C_3 and MgO phases observed in the XRD results. the Cu lines observed in the EDS is from the sample grid. These intragrain nanosized inclusions and the crystal defects created by C

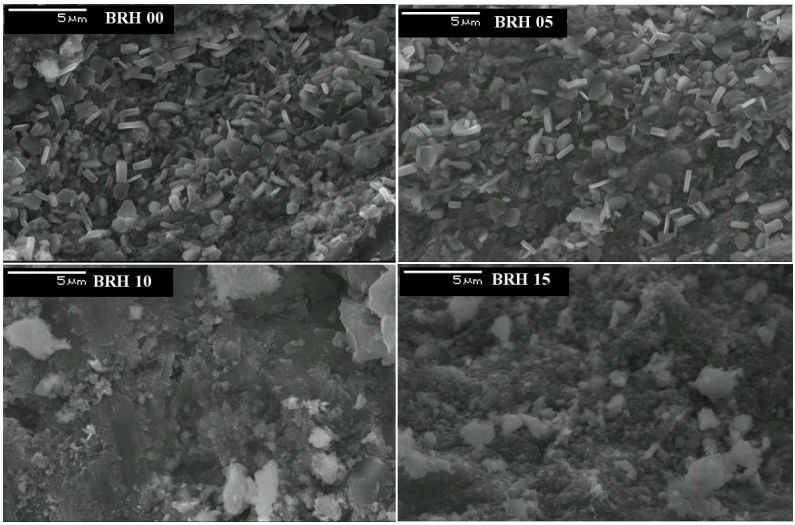

Figure 5.18: SEI SEM of BRH added samples.

substitution serve as strong pinning centers to improve flux pinning.

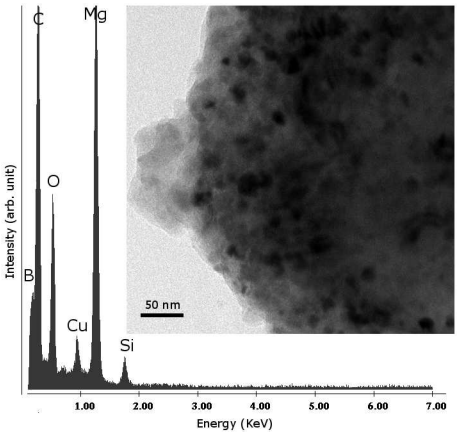

Figure 5.19: EDS and TEM image of BRH 05 (5 wt.% of BRH added) sample.

5.3.3 Discussion of the results

The results (Lattice parameters, FWHM and T_C) show considerable amount carbon substitution at the boron site, as expected. Significant enhancement of $J_C(H)$ is observed, especially at higher applied fields, for the BRH added samples. The enhancement due to BRH addition is comparable to that observed for nano SiC added samples. The enhancement of $J_C(H)$ in the BRH added samples can be understood as a result of the carbon substitution and due to the flux pinning at nano scale intra-grain inclusions). The higher wt.% BRH added samples contain a lot of impurity phases and this is the reason for their low $J_C(H)$ performance.

5.3.4 Conclusion of the addition

Burned rice husk, containing fine amorphous silica and carbon is explored as an additive for effective carbon substitution for enhancing the $J_C(H)$ of MgB_2. The BRH addition resulted in significant C substitution as expected and consequently improved the high filed J_C of MgB_2 significantly. The observed enhancement of $J_C(H)$ due to the BRH addition is found to be comparable to that of nano SiC addition. Hence BRH is found to be an effective and cheap additive for enhancing the $J_C(H)$ of MgB_2 superconductor.

5.4 Effect of combined addition of nano TiC with nano SiC

According to Dou *et al* [130–132] the additives in MgB_2 can be categorized into four groups. The first group includes additives like nano SiC and carbohydrates which can have both reaction with Mg/B and C substitution. The second group includes materials such as nano C, CNT , and B_4C which can have C substitution without any reaction. The third group includes materials such as Si, Zr, Ti, RE oxides and silicides which can react with Mg/B without any C substitution, and the fourth group includes materials such as BN, MgO, which do not have any reaction with Mg/B nor any C substitution. From the first group to fourth group the enhancement of $J_C(H)$ decreases gradually.

Both SiC and TiC are highly thermally stable compounds. When added into the Mg + B system, SiC easily reacts with Mg and releases free C at

a temperature as low as 600-650 ^{0}C, which subsequently substitutes for B in MgB_2 [131, 132, 190]. But TiC has no reaction with Mg/B for temperatures $\leq$850 ^{0}C and the C substitution is comparably small [190]. Even at higher temperatures in Mg + B system it reacts with B to form TiB_2, rather than with Mg as in the case of SiC. Moreover Ti is found to be a grain refiner in MgB_2 [137, 191, 192]. Thus in MgB_2 both these carbides work differently, have different reactivity with Mg/B and have different extent of C substitution. Hence it is interesting not only to compare the doping effect of SiC and TiC separately but also to find their combined effect in MgB_2. It is found that the $J_C(H)$ behaviour is highly enhanced for the codoped samples compared to the undoped as well as the mono added samples. The crystalline and microstructural features of the materials were investigated to correlate with the $J_C(H)$ performance.

Table 5.7: Sample details : nano SiC and nano TiC addition.

Sample	wt.% of nano particles added	
Name	nano SiC	nano TiC
MBST 00	0	0
MBST 50	5	0
MBST 05	0	5
MBST 2.5	2.5	2.5
MBST 55	5	5

The undoped, monodoped and codoped samples were prepared by *in situ* powder-in-sealed-tube (PIST) method, using Mg (-325 mesh, 99.8%), amorphous B (-325 mesh, 99%), nano TiC ($<$ 80 nm, 98%) and nano SiC ($<$ 100 nm, 97.5%) as starting powders. The samples were heat treated at 850 °C for 2 hours and details of the samples prepared and sample names are listed in table 5.7.

5.4.1 Results: Crystalline properties

Figure 5.20 shows the powder XRD patterns of the samples. MgB_2 is the main phase, with a trace amount of MgO, observed in all the samples. Boron rich phases such as MgB_4, MgB_7 are not observed in any of the samples. Samples added with SiC showed considerable amount of Mg_2Si and minor quantities of unreacted SiC. For the TiC doping no reacted phase is observed and the TiC as such is observed as unreacted. The formation of

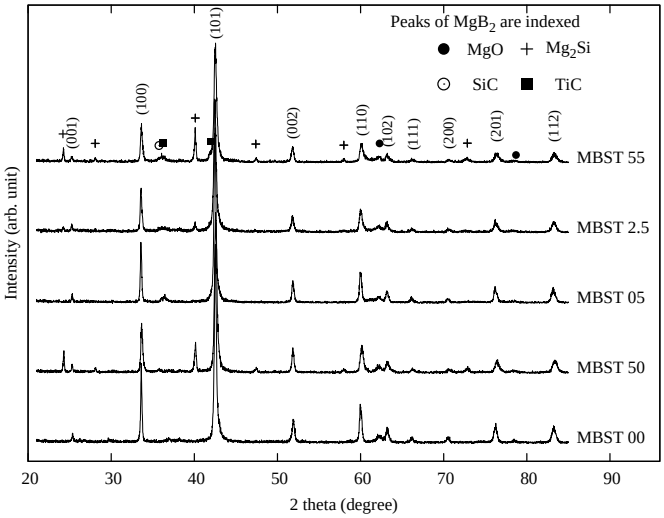

Figure 5.20: Powder XRD patterns of the nano SiC and nano TiC added samples.

Mg_2Si in SiC added samples indicates the dissociation of the SiC and the reaction of Si with Mg at the synthesis temperature. In fact this decomposition of SiC and the formation of Mg_2Si phase are reported in almost all the SiC doping studies. SiC starts to react with Mg at a temperature as low as 600 °C [131–133, 190]. Besides the SiC doping, the Mg_2Si is found to form for most of the Si based additives, such as Si, silicides, silicon oil etc on MgB_2 [193–195]. As stated early, we observed no decomposition of TiC and associated reaction of TiC with Mg/B at our synthesis temperature (850 °C/2h). The detailed study of reactivity of various submicron sized carbides on MgB_2 bulks by A.Yamamoto *et al* [190, 196] shows that TiC does not react with Mg/B upto 850 °C, but C substitution at B site and formation of small amount of TiB_2 phase are found at 950 °C.

The volume percentage of different phases formed in the samples is assessed from the integrated Xray peak intensities and is tabulated in table 5.8. The undoped sample has the best phase purity and the highest MgB_2 volume fraction (98.3 %). The addition of SiC causes more secondary phases, thus reduces the MgB_2 fraction, than the TiC addition. Minor fractions of MgO are observed in all the samples which are almost same in all cases. The MgO formation may be due to the entrapped air before the end

Table 5.8: Structural properties of the samples: Phase analysis.

Sample	Vol.% of different phases (%)					Relative intensity		Density
	MgB_2	MgO	Mg_2Si	SiC	TiC	$\frac{\Sigma(hk0)}{\Sigma(hkl)}$	$\frac{\Sigma(00l)}{\Sigma(hkl)}$	(g/cm^3)
MBST 00	98.3	1.7	0	0	0	0.306	0.078	1.39
MBST 50	79.0	1.9	18.3	0.8	0	0.251	0.095	1.46
MBST 05	96.6	1.8	0	0	1.6	0.274	0.076	1.41
MBST 2.5	90.2	1.7	6.6	0	1.5	0.254	0.086	1.55
MBST 55	72.1	1.8	21.6	0.9	3.5	0.247	0.095	1.50

sealing of the tubes. The ratio of total intensity of *(hk0)* planes and *(00l)* planes to the total intensity of all the peaks (defined as the relative intensity of *(hk0)* and *(00l)* planes) for the samples is shown in table 5.8. The relative intensity of *(hk0)* planes is slightly reduced and that of *(00l)* planes slightly increased as a result of doping. In the monodoped samples SiC cause more changes in the relative intensity values, than the TiC. The geometrical density, determined by measuring the mass and dimensions of the samples, is also given in table 5.8. The undoped sample has the lowest density of 1.39 g/cm^3, nearly 50% of the theoretical density of MgB_2. Among the samples the codoped sample MBST 2.5 show the highest density of 1.55 g/cm^3.

The crystalline properties of the samples such as lattice parameters, unit cell volume and lattice strains are evaluated using the powder XRD data and are tabulated in table 5.9. The doping - both mono and codoping changed the crystalline features of MgB_2 significantly. The lattice parameters *a* and *c* show systematic variations with the nature and amount of the additives. The changes in lattice parameters with respect to the undoped sample (Δa and Δc) are more for SiC doping than the TiC doping. The lattice parameter *a* decreases significantly with the SiC doping, while it slightly increases with TiC doping, compared to the undoped one. Among the samples, the mono SiC added sample show the lowest value for *a* axis. For the codoped samples, since SiC has a large impact on *a*, the *a* decreased and its decrease is more in MBST 55 than in MBST 2.5. For the *c* axis both the SiC and TiC caused slight increase compared to the undoped one. Here also as in the case of *a* axis, the variation is more in the SiC doping.

The unit cell volume slightly increases with TiC and slightly decreases with SiC doping. The ratio $\frac{c}{a}$, can be used as a measure of lattice distortion, which doesn't show any variation with the TiC doping, but increases with SiC doping.

Table 5.9: Structural properties of the samples: Lattice parameters.

Sample	Lattice parameters and cell volume				Carbon content *
	a (Å)	*c* (Å)	(*c*/*a*)	V ($Å^3$)	(*x* in $MgB_{2-x}C_x$)
MBST 00	3.084	3.518	1.141	28.976	-
MBST 50	3.073	3.524	1.147	28.976	.030
MBST 05	3.086	3.521	1.141	29.039	-
MBST 2.5	3.083	3.524	1.147	28.982	.005
MBST 55	3.080	3.527	1.147	28.976	.010

* The C content in the added samples is estimated based on the reports of RHT Wilke *et al* [197] and Takenobu *et al* [198], and the averaged data is given.

The Full Width at Half Maximum (FWHM) of selected peaks of the samples are shown in figure 5.21. The data shows a clear and systematic trend with doping. The FWHM of the *(00l)* planes has hardly any effect by both the additives, either for mono or codoping. But the FWHM of *(hk0)* and *(hkl)* planes are affected by the doping: *(hk0)* is the most affected plane. As in the case of lattice parameters, here also SiC is mainly responsible for the changes in FWHM values. The FWHM of *(hk0)* significantly increases with SiC doping, which is in accordance with most of the works reported on the doping studies of SiC or C or other C based additives and is due to the C substitution at B sites.

In the hexagonal structure *p*6/*mmm*, Mg atoms occupy the 1a site (0,0,0) and the B atoms at the 2d site ($\frac{1}{3},\frac{2}{3},\frac{1}{2}$). The reported works demonstrate that C atoms preferentially occupy at the 2d site [69, 185]. This results in the contraction of inplane lattice, since the covalent radii of C is lower than that of B and the availability one extra electron. The lattice strains consequent to the C substitution at B site is also responsible for the increased FWHM of the SiC added samples. In the case of TiC the observed behavior doesn't correlate with the C substitution results. The next possibility is of Ti substitution. But it is known that Ti doesn't occupy the atomic positions (site) in the MgB_2 crystal structure [191, 192]. Even for the Ti added samples Ti either remained as unreacted or reacted with B to form TiB_2 or TiB_4 [191, 192]. So the possibility of Ti going into the lattice structure in our case is remote. Hence, the observed slight variations in the lattice parameters as well as FWHM of TiC added samples may be from the lattice distortions caused by the inclusions of nanoparticles of TiC within the MgB_2 grains, rather than a substitution.

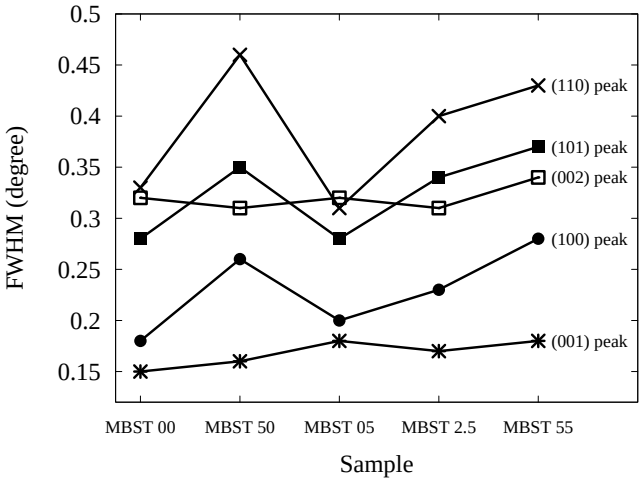

Figure 5.21: FWHM values of selected peaks of the nano SiC and nano TiC added samples.

All the structural features of the samples evaluated above, including phase analysis, relative intensity, lattice parameters and FWHM analysis strongly suggest that the added SiC caused a considerable C substitution at the B site. The SiC caused Mg_2Si formation also. Meanwhile the TiC remained as unreacted and doesn't cause any substitution in the MgB_2 system. Based on the literature reports of variation of *a* axis with C substitution level (x in $MgB_{2-x}C_x$) we have estimated the C substitution level in our samples and is listed in table 5.9. The literature data we have used were on polycrystalline samples taken from R. H. T. Wilke *et al* [197] and Takenobu *et al* [198]. The average values of estimated carbon contents are x around 0.03, 0.005 and 0.01 for the MBST 50, MBST 2.5 and MBST 55 samples respectively.

5.4.2 Results: Microstructural properties

The microstructural properties of the samples were investigated using SEM, TEM and EDS analysis. Figure 5.22 shows the SEM images of the fractured surfaces of the samples which show a distinct microstructural change as a result of the doping. The undoped sample shows randomly oriented hexagonal MgB_2 grains with average size of 1-2 μm. The undoped sam-

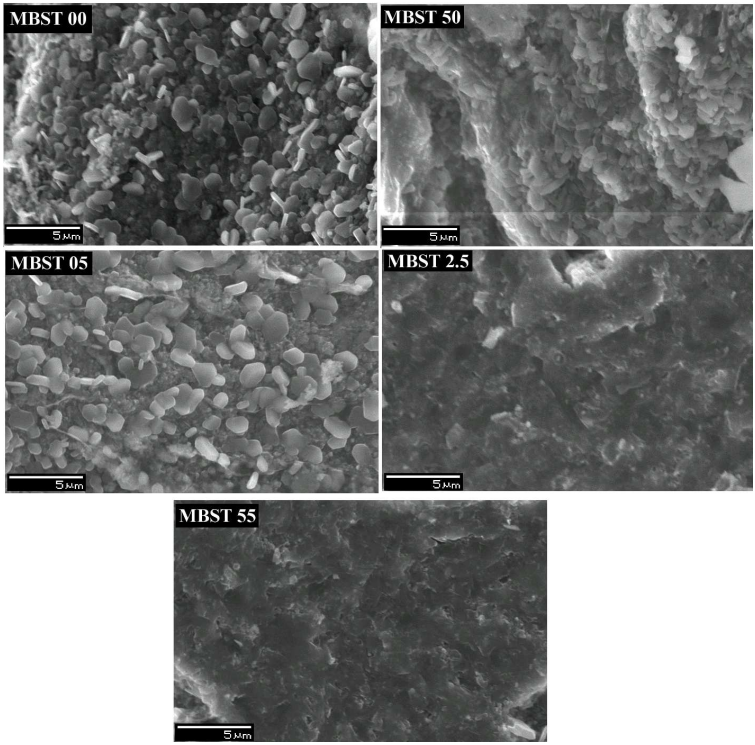

Figure 5.22: SEM images of fractured surfaces of the nano SiC and nano TiC added samples.

ple has grains with considerably sharp grain boundaries, while most of the added samples do not have this feature. The mono SiC added sample (MBST 50) shows a microstructure slightly different from that of undoped sample. The TiC added sample (MBST 05) shows a microstructure similar to that of the undoped sample. The codoped samples show a similar microstructure, distinctly different from that of the above samples. These samples show compacted, more homogeneous microstructure with less defined grain boundaries. This densified microstructure of the codoped sample is in agreement with the higher calculated geometrical density for these samples.

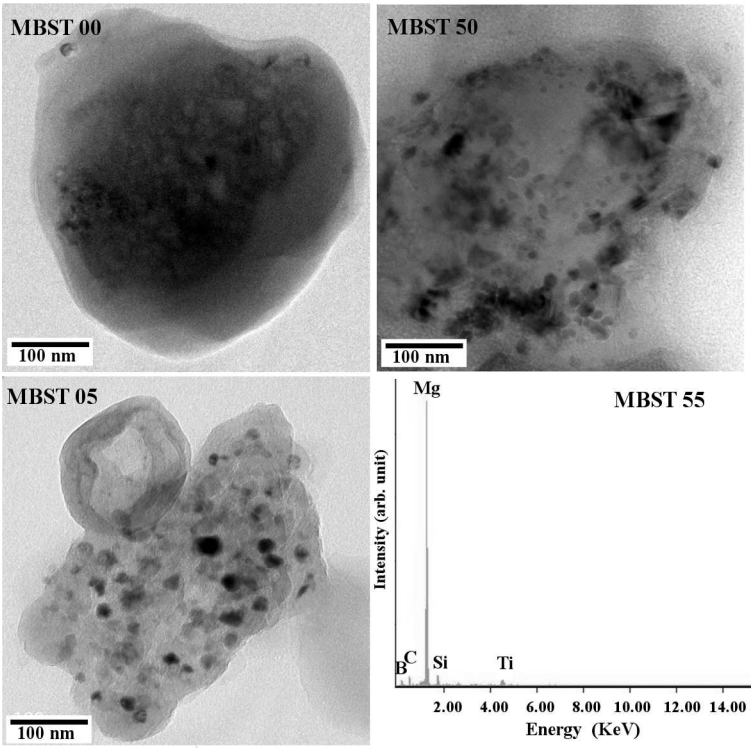

Figure 5.23: TEM images and EDS pattern of selected samples.

Figure 5.23 shows the TEM images of the samples MBST 00, MBST 50 and MBST 05 under identical magnification and the EDS pattern of MBST 55. The images of single grains show microstructural changes due to doping. The image of undoped grain is found to be free of any inclusions. Both the SiC and TiC added samples clearly show nano sized intragrain inclusions. The inclusions of TiC doping are more homogeneous than in SiC doping in which some clustering and agglomeration are observed. In both cases, the average size of the inclusions is around 10 nm. This value is quite comparable with the coherence length of MgB_2, and hence these inclusions can act as strong flux pinning centers. The last picture in the figure shows the frame (area) EDS spectrum of the grain in MBST 55 as a typical example. This picture shows the presence of elements Si, Ti, C and O besides Mg and B.

5.4.3 Results: Superconducting properties

Figure 5.24 shows the ZFC magnetization curves for the samples, taken at 100 Oe. The inset of the figure shows the region close to the superconducting transition. The undoped sample shows a superconducting transition at 38.44 K. T_C of the added samples is reduced and the reduction is more for MBST 55. The values of T_C and ΔT_C (defined as the difference of the temperatures corresponding to the 90% and 10% of the maximum shielding signal) are given in table 5.10. For the monodoping SiC reduces the T_C more than the TiC does. This is expected due to the C substitution at B site. In MgB_2 the B plane is responsible for the superconductivity. The substitution of C at B site reduces the hole concentration and causes changes in phonon modes. The reduced density of states and weakened electron phonon coupling are the reasons for T_C reduction in the SiC added sample. The TiC mono added sample also shows slightly reduced T_C (37.85 K). Since no C substitution takes place here the T_C reduction may be due to the lattice strains caused by the nanometer sized TiC inclusions in the MgB_2, as lattice strains can also cause slight T_C reduction in MgB_2 [199]. The T_C of codoped samples are lower to that of mono added samples and the T_C is minimum for MBST 55 (37.09 K), the heaviest codoped sample. This is due to the combined effect of both SiC and TiC additives: ie C substitution and lattice strains. The width of transition, ΔT_C is minimum for the undoped sample. The value of ΔT_C is higher for MBST 50 and comparatively low for MBST 05. In the codoped sample ΔT_C is highest for MBST 55. The ΔT_C depends on the sample homogenity, crystallinity etc. The higher ΔT_C of MBST 50 is again the result of C substitution, which reduces the inplane (B plane) crystallinity.

Table 5.10: Superconducting properties of the samples - I.

Sample	T_C (K)	ΔT_C (K)	J_C ($\times 10^3$ A/cm^2) at	
			5 K, 8 T	15 K, 7 T
MBST 00	38.44	1.08	0.17	$<$0.01
MBST 50	37.43	1.85	3.77	0.52
MBST 05	37.85	1.44	1.32	0.25
MBST 2.5	37.22	1.47	4.90	0.80
MBST 55	37.09	1.73	4.20	0.68

The magnetic field dependence of critical current density of the samples ($J_C(H)$) at 5 K and 15 K are deduced from the isothermal magnetic hysteris

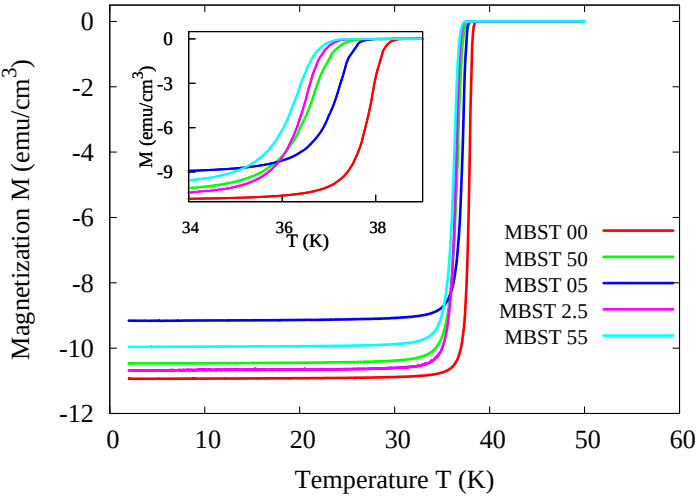

Figure 5.24: ZFC curves of the nano SiC and nano TiC added samples, taken at 100 Oe.

(M-H) measurements. Thermomagnetic flux jumps are observed below 1 T for all samples at 5 K and 15 K. The flux jump is more at 5 K. The variation of J_C of the samples with field is plotted in figure 5.25. At lower fields the estimation of $J_C(H)$ may not be accurate due to flux jumps. The $J_C(H)$ is significantly enhanced for all the added samples both at 5 K and 15 K compared to the undoped sample, for the entire field of study. For the monodoped samples SiC doping shows much improvement in high field J_C, compared with the TiC doping. However the codoped sample shows the best $J_C(H)$ performance at higher fields both at 5 K and 15 K. The codoped sample MBST 2.5 shows highly enhanced J_C values for the entire field of study, both at 5 K and 15 K. The another codoped sample MBST 55 also shows enhanced J_C values for the entire fields, but at low fields (below 3-4 T) its $J_C(H)$ is comparable or slightly lower to that of MBST 50. Besides the drastic enhancement of $J_C(H)$ at high fields for most of the added samples, either monodoped or codoped, the low field J_C [$J_C(H)$, $H \rightarrow 0$] is better compared to that of undoped sample. This is very important, since for most of the reported works on the enhancement of high field J_C of MgB_2 exhibit poor low field $J_C(H)$ performance. The better low field J_C of the added samples indicates that the grain connectivity is not disturbed

by the doping.

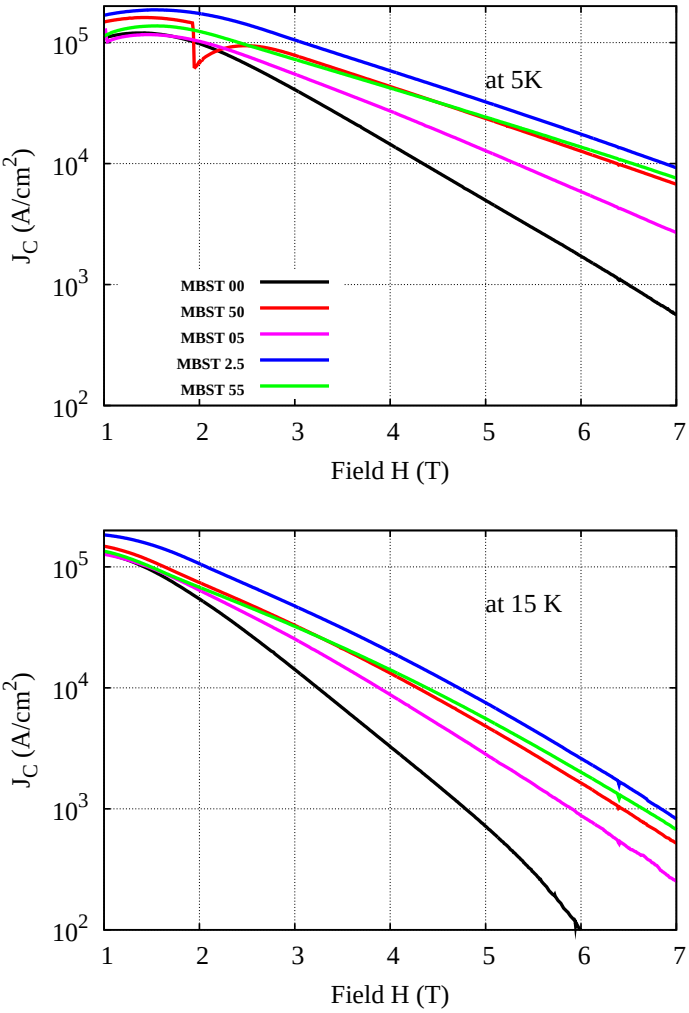

Figure 5.25: $J_C(H)$ curves of the nano SiC and nano TiC added samples.

The value of critical current density of the samples at selected fields and temperatures is tabulated in the table 5.10. At 5 K and 4 T the J_C values are 1.44 $\times 10^4$ A/cm^2, 4.34 $\times 10^4$ A/cm^2, 2.72 $\times 10^4$ A/cm^2, 5.67 $\times 10^4$ A/cm^2 and 4.29 $\times 10^4$ A/cm^2 for MBST 00, MBST 50, MBST 05, MBST 2.5 and MBST 55. At 5 K and 8 T the J_C values are 0.17 $\times 10^3$ A/cm^2 for the undoped sample, 3.77 $\times 10^3$ A/cm^2, enhanced by a factor of 22 for SiC monodoped sample and 4.90 $\times 10^3$ A/cm^2, enhanced by a factor of 29 for MBST 2.5, the codoped sample. At 15 K and 7 T the added samples MBST 50, MBST 05, MBST 2.5 and MBST 55 have J_C values enhanced by a factor of nearly 60, 30, 100 and 76 times, compared to the undoped sample. Thus for the best codoped sample a significant enhancement of J_C by two orders of magnitude is achieved, at higher temperatures and higher fields (15 K, $>$ 7 T). In general, the sample (MBST 2.5) has $J_C(H)$ enhanced by 1.5-2.0 times, compared the mono SiC doping (MBST 50) and by 2.0-4.0 times, compared the mono TiC doping (MBST 05). The values of the irreversibility field H_{irr} of the samples at 5 and 15 K are determined by the linear extrapolation to zero for the high field low J_C segments of the Kramer curves and is tabulated in table 5.10. The values of H_{irr} once again reflects the strong enhancement of the superconducting properties as a result of doping. As in the case of $J_C(H)$ the improvement of H_{irr} is higher for codoped samples, both at 5 K and 15 K.

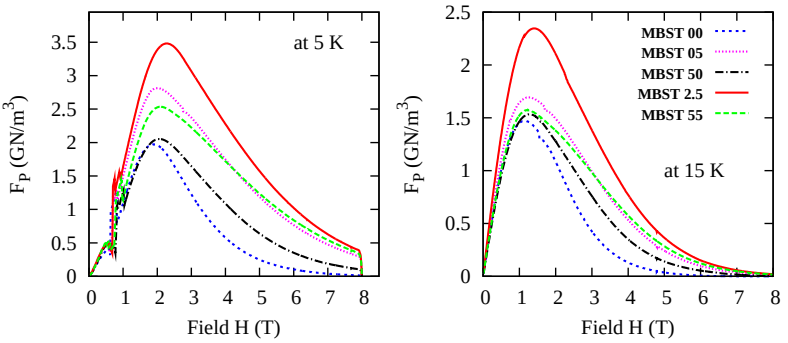

Figure 5.26: Field dependence of flux pinning force density of the nano SiC and nano TiC added samples.

Figure 5.26 shows the bulk flux pinning force density of the samples as a function of the applied field. The flux pinning force density of the

added samples are significantly enhanced and the enhancement is more in the codoped sample. Since the flux jumps shows significant marks on the shape of the curves at 15 K, the curves are plotted after refining the $J_C(H)$ data between 1 and 2 T. The curves show significantly improved flux pinning force density in the added samples, both at 5 and 15 K. Maximum value of F_P (F_{Pmax}) is 3.48 GN/m^3 and 2.35 GN/m^3 for the best sample (MBST 2.5) at 5 and 15 K, while these values are 1.97 GN/m^3 and 1.47 GN/m^3 for the undoped sample. Also the field at which F_{Pmax} occurs (H_{peak}) is shifted to higher fields in the added samples. The values of F_{Pmax} and H_{peak} for the samples are tabulated in table 5.11. These results clearly show the considerable improvement in the flux pinning of the system as a result of doping.

Table 5.11: Superconducting properties of the samples - II.

Sample	H_{irr} (T) at		F_{Pmax} (GN/m^3) at		H_{peak} (T) at	
	5 K	15 K	5 K	15 K	5 K	15 K
MBST 00	8.8	6.3	1.97	1.47	1.92	1.14
MBST 50	10.9	8.4	2.81	1.69	2.00	1.26
MBST 05	10.1	7.2	2.05	1.53	2.07	1.25
MBST 2.5	10.9	8.7	3.48	2.35	2.27	1.41
MBST 55	11.1	8.7	2.54	1.57	2.10	1.22

5.4.4 Discussion of the results

The main result of the present work is the significant enhancement in the $J_C(H)$ performance of MgB_2 superconductor as a result of codoping of nano TiC with nano SiC for the entire range of field studied. Among the additives the nano SiC resulted in considerable C substitution at the B site and formation of reacted secondary phase Mg_2Si in the matrix. In the case of nano TiC doping the TiC remained unreacted as such and caused no substitutions. Considering the phase purity and crystallinity, the undoped sample is found to be the best. Also it has the highest T_C among the samples. But it has the lowest flux pinning force and the lowest $J_C(H)$ performance. Thus the observed enhancement of flux pinning and in-field J_C of the added samples cannot be due to any improvements in phase purity or crystallinity.

The $J_C(H)$ of MgB_2 is controlled by both intragranular and intergranular properties. The main intragranular (or intrinsic) factors affecting the

$J_C(H)$ of MgB_2 are upper critical field (H_{C2}), flux pinning strength, and to some extend the anisotropy of superconductivity. Grain connectivity, which controls the efficiency of superconducting current to transport from grain to grain is the main intergrain (extrinsic) factor. Among these various factors, the enhancement of H_{C2} and improvement of flux pinning by homogeneously distributed pinning centers are most important. The H_{C2} of MgB_2 is strongly depended on σ and π band scattering rates (both inter and intra scattering), and the value of H_{C2} in MgB_2 enhances significantly upon tuning of the scattering rates [200, 201]. For the improvement of flux pinning homogeneously distributed normal particles of suitable size must be introduced in MgB_2.

The bulk polycrystalline MgB_2 samples prepared without any externally introduced (pristine sample) pinning centers will be moderately pinned by the grain boundaries. In general, the introduction of additives in MgB_2 can have the following effects.
(1) increase the H_{C2} and H_{irr} by lattice substitutions (which alter the band scattering rates).
(2) increase the density and strength of flux pinning centers by homogeneous inclusions (either reacted or unreacted impurities).
The enhancement of $J_C(H)$ in MgB_2 by SiC doping is explained by the dual reaction model [131, 132]. Based on this model the C substitution at B site results strong H_{C2} enhancement due to band scattering modifications (effect 1 described above) and causes the improvement in $J_C(H)$. Further improvement is provided by the flux pinning of unreacted nanoscale SiC and the reacted secondary phase Mg_2Si, as described in effect 2. There can be unreacted B left as a result of the C substitution and consumption of Mg for the formation of Mg_2Si. So far no serious attention is given to this issue in SiC added case. If the unreacted B causes some non stoichiometry, it will also cause H_{C2} enhancement as described elsewhere [94]. Detailed analysis on SiC added MgB_2 samples shows evidences for the formation of secondary phases containing Mg, Si, B, O, C elements. The presence of amorphous BO_x phases is also considered [202, 203]. These phases are considered to act as additional flux pinning centers. However these phases can limit the superconducting volume fraction and can reduce the grain connectivity if located at the grain boundaries rather residing inside the grains.

In the TiC added samples no substitution is observed. So the effect 1 will be negligible in the sample, and this may be the reason for relatively

small improvement of $J_C(H)$ in MBST 05 compared with MBST 50. The unreacted residual TiC in nanoscale can act as strong flux pinning centers, as described in effect 2. The TEM image of MBST 05 shows fine homogeneously distributed nanometer sized inclusions, also favors this argument. Thus for the enhancement of $J_C(H)$ the major contribution in SiC is effect 1 and in TiC is effect 2. On the other hand, for effect 1 SiC is a better dopant and effect 2 TiC is better. Here the nano SiC acted as a group-I dopant, ie as C source and reactive dopant and TiC acted as a group-IV dopant, ie nonreactive and non C source. In the codoped samples both the effects of SiC and TiC may be active, and this is the reason for its better performance compared with the undoped and monodoped samples. Besides the improvement of H_{C2} and flux pinning, grain connectivity may also be better for the added samples. The codoped samples have denser and compacted microstructure compared with the undoped sample. The low field J_C of the samples is not deteriorated by doping, and the codoped samples have high $J_C(H)$ values in spite of large amounts of garbages.

5.4.5 Conclusion of the addition study

The effects of two carbides - SiC and TiC in nano particle form, on the structural and superconducting properties of MgB_2 are studied. The behaviour of these additives in the Mg + B system is compared and the codoping of these two materials in the system is also explored with respect to the crystalline, microstructural and superconducting properties. It is found that both these additives have different reactivity and hence different crystalline and microstructural influences on MgB_2. The superconducting properties of added MgB_2 also differ for the two additives. SiC caused considerable amount of C substitution at B site and formed nano size intragrain inclusions of Mg_2Si. While TiC remains unreacted and does not induce any substitution. Considering the $J_C(H)$ performance, for monodoping SiC is better than TiC. But codoping of TiC with SiC is found to be much more effective for the enhancement of $J_C(H)$ of MgB_2 than the mono doping of any one of these additives. Thus it may be fruitful to explore the effects of codoping of impurities of differing nature to the MgB_2 system to get far better $J_C(H)$ performance achieved so far by any one type of additives.

5.5 Effect of substituting type (carbon based: BRH) and reacting type (REO: nano Ho_2O_3) additives

From the above study, codoping of materials with different chemical and physical nature is found to be very effective for enhancing the high-field J_C of MgB_2. Here codoping of burned rice husk (BRH) together with a REO on the $J_C(H)$ of MgB_2 is studied. The preliminary investigation showed that addition of BRH can cause significant C substitution at B site at around 850 °C. Nano Ho_2O_3 is chosen as the REO for codoping with BRH, since it causes the formation of HoB_4, which is magnetic in nature.

The undoped, monodoped and codoped samples were prepared by *in situ* powder-in-sealed-tube (PIST) method, using Mg (-325 mesh, 99.8%), amorphous B (-325 mesh, 99%), nano Ho_2O_3 ($<$ 60 nm, 99.5%) and burned rice husk as starting powders. All the samples were heat treated in air at 850 °C for 2 hours. The wt % of additives added and sample names are given in table 5.12.

Table 5.12: Sample details : BRH and nano Ho_2O_3 addition.

Sample Name	wt.% of nano particles added	
	BRH	nano Ho_2O_3
S 00	0	0
S 50	5	0
S 05	0	5
S 52	5	2.5
S 55	5	5

5.5.1 Results: Superconducting properties

Figure 5.27 shows the field dependence of magnetic J_C [$J_C(H)$] of the samples at 5 K, deduced from M-H data. The $J_C(H)$ is enhanced for all the added samples compared to the undoped one. The improvement in $J_C(H)$ in Ho_2O_3 alone added sample is only moderate compared to the undoped sample. But the BRH doping shows strong improvement in high field J_C, compared to the Ho_2O_3 doping. The level of J_C enhancement by BRH addition in high magnetic fields is very similar to that exhibited by nano SiC, nano C and/or other carbon based additives. The codoped samples S

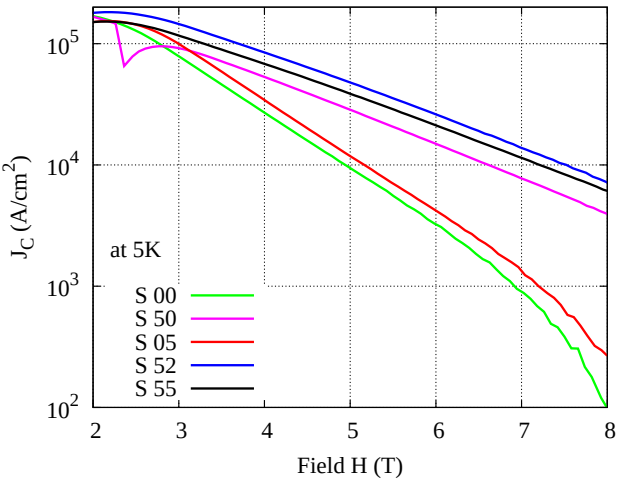

Figure 5.27: $J_C(H)$ curves of BRH and nano Ho_2O_3 added samples.

52 and S 55 show still higher $J_C(H)$ values than the BRH added sample of which S 52 showed the best $J_C(H)$ performance through out the entire field of study.

As shown in the table 5.13, at 4 T the value of J_C is 2.7×10^4 Acm^{-2}, 5.3×10^4 Acm^{-2}, 3.4×10^4 Acm^{-2}, 8.4×10^4 Acm^{-2} and 6.8×10^4 Acm^{-2} for the samples S 00, S 50, S 05, S 52 and S 55 respectively. At 8 T, samples S 50, S 05, S 52 and S 55 have J_C values enhanced by a factor of 40.8, 2.6, 74.5 and 62.8, compared to the undoped sample. The values of the irreversibility field H_{irr} of the samples are determined by the linear extrapolation to zero for the high field low J_C segments of the Kramer curves and is tabulated in table 5.13. As in the case of $J_C(H)$ the improvement of H_{irr} is highest for codoped samples. Figure 5.28 shows the bulk flux pinning force density of the samples as a function of the applied field. At higher fields, the flux pinning force density of the added samples is significantly enhanced and the enhancement is highest in the codoped sample. At 5 K and 4 T the value of F_P are 1.1, 2.1, 1.4, 3.4 and 2.7 GN/m^3 for S 00, S 50, S 05, S 52 and S 55, and the values are tabulated in table 5.13.

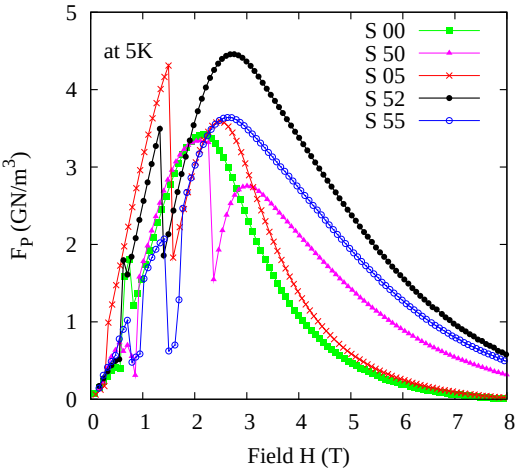

Figure 5.28: Field dependence of flux pinning force density for BRH and nano Ho_2O_3 added samples.

Table 5.13: Superconducting properties of the samples. J_C, H_{irr} and F_P values are at 5 K

	T_C	ΔT_C	J_C (A/cm^2) at		H_{irr}	F_P at 4 T
sample	(K)	(K)	4 T ($\times 10^4$)	7 T ($\times 10^3$)	(T)	(GN/m^3)
S 00	38.5	0.4	2.7	0.9	8.4	1.1
S 50	38.0	0.9	5.3	7.7	10.2	2.1
S 05	38.4	0.5	3.4	1.3	8.65	1.4
S 52	37.6	1.2	8.4	13.8	11.2	3.4
S 55	37.5	1.1	6.8	11.4	11.1	2.7

ZFC magnetization curves for the samples, taken at 20 Oe are shown in figure 5.29. The undoped sample shows a superconducting transition at 38.5 K, with a ΔT_C of 0.4 K. For the Ho_2O_3 addition the T_C and ΔT_C are almost same as those of the undoped sample, indicating that the Ho ion is not substituted into the Mg/B sites. Generally most of the RE ions (especially Ho) do not substitute at the Mg/B site, due to their large ionic radii compared to Mg and/or B. The T_C of the BRH added sample (S 50) is reduced by 0.5 K. This reduction is due to the C substitution, however the observed reduction is smaller compared to other C based doping studies

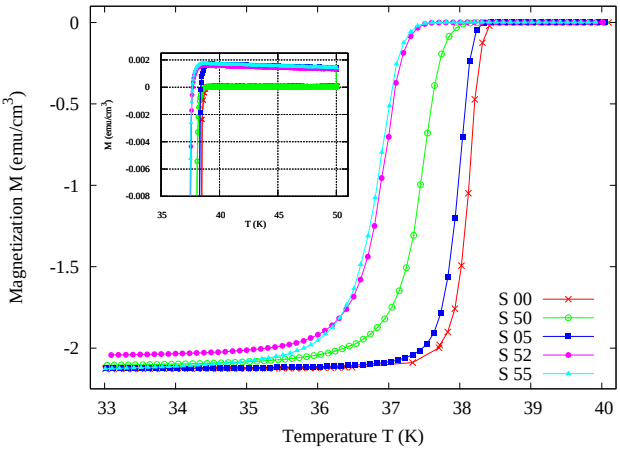

Figure 5.29: ZFC M-T plots of BRH and nano Ho_2O_3 added samples, taken at 20 Oe field.

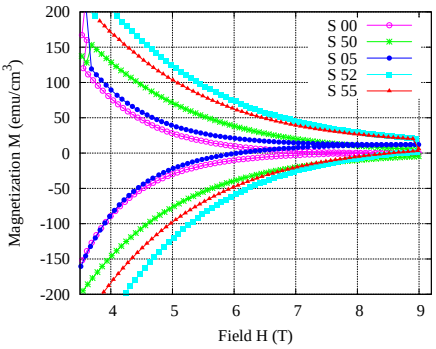

Figure 5.30: Section of M-H plots of BRH and nano Ho_2O_3 added samples.

[69]. In the codoped samples the value of T_C is further reduced, may be due to the presence of higher amounts of non-superconducting secondary phases.

The value of ΔT_C is higher for BRH addition and comparatively low for Ho_2O_3 addition. In the codoped samples ΔT_C is still higher. The ΔT_C depends on the sample homogenity, crystallinity etc. The higher ΔT_C of S

50 is again the result of C substitution, which reduces the inplane (B plane) crystallinity.

Inset of the figure 5.29 shows the ZFC magnetization curves enlarged near the transition region. Samples added with Ho_2O_3 show a considerable positive magnetic moment ($M > 0$) in the normal state. This is expected as the Ho_2O_3 samples have the reacted phase HoB_4, which has a strong magnetic moment. The magnetic behavior of HoB_4 is observed as a superposed paramagnetic background in the magnetization hysteresis loops of S 05, S 52 and S 55 samples (figure 5.30) also.

5.5.2 Results: Structural properties

Figure 5.31 shows the powder XRD patterns of the samples. MgB_2 is the main phase, with a trace amount of MgO, observed in all the samples. Significant amount of HoB_4 is observed in samples added with Ho_2O_3 and slight amounts of Mg_2C_3 and Mg_2Si are observed in BRH added samples. No Ho_2O_3 or other Ho containing phase is observed in the Ho_2O_3 added samples. As stated earlier BRH contains amorphous silica and C, available for reaction. It seems that Si and C contained in the BRH reacted with Mg to form the Mg_2Si and Mg_2C_3 phases. It is reported that Mg_2Si forms in most of the Si based additives, such as nano-SiC, Si, silicides, silicon oil etc on MgB_2 [193–195] and has a significant role in improving the flux pinning. Formation of Mg_2C_3 is also reported in carbon based doping studies [140, 204]. No detectable amount of SiO_2 is observed in the BRH added samples. The presence of HoB_4 indicates that some of the added Ho_2O_3 decomposed and reacted with B at the heat treated temperature as reported earlier in the case of other REO doping [146–149]. In the codoped samples HoB_4, Mg_2Si and Mg_2C_3 are observed as secondary phases, besides MgO. No additional reacted phases are observed as a result of codoping.

The volume percentage of MgB_2 and MgO phases formed in the samples is assessed from the integrated Xray peak intensities and is tabulated in table 5.14. The undoped sample has the best phase purity and the highest MgB_2 volume fraction. Volume percentage of MgO is minimum in the undoped sample and is maximum in highly codoped sample. Minor fractions of MgO observed in the undoped sample is due to the entrapped air before the end sealing of the tubes. The oxygen available in BRH and Ho_2O_3 is responsible for the increased amount of MgO in the added samples.

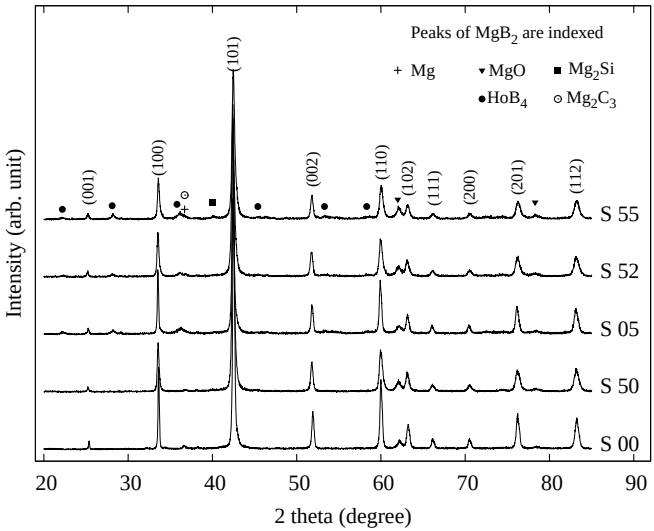

Figure 5.31: XRD patterns of BRH and nano Ho_2O_3 added samples.

Table 5.14: Crystalline properties of the samples

	Vol. of (%)		Lattice parameters			Carbon[1]	grain	strain[2]
Sample	MgB_2	MgO	*a* (Å)	*c* (Å)	*c/a*	content	size	(%)
S 00	97.3	1.6	3.084	3.525	1.143	-	210	0.80
S 50	95.7	3.1	3.077	3.526	1.146	0.021	140	1.1
S 05	93.7	2.3	3.086	3.522	1.141	-	180	0.8
S 52	93.2	3.6	3.080	3.525	1.144	0.013	90	0.9
S 55	88.2	4.4	3.080	3.529	1.146	0.013	60	0.9

[1] x in $MgB_{2-x}C_x$, estimated based on the data of RHT Wilke *et al* [197] and Takenobu *et al* [198].
[2] Lattice strain of (*hk0*) plane is determined from the slop of Williamson-Hall plot (Figure 5.33).

The *a* and *c* lattice parameters, calculated from the XRD data, for a hexagonal crystal structure, is given in table 5.14. The value of *a* decreases considerably and *c* increases slightly with the BRH addition. This is in agreement with other works on carbon based doping and is due to the substitution of C at the B site and is explained elsewhere [69, 205]. For the Ho_2O_3 addition *a* shows slight increase and *c* remains almost the same, compared to the undoped sample. Here also the observed result is in accordance with other REO additions. For the REO doping it is believed that

RE will not occupy the lattice site of either Mg or B and hence the observed very small change in the lattice parameters may be due to the strain induced by the nano particles, rather than a substitutional effect or structural change. In the codoped samples *a* decreases and *c* increases compared to the undoped one. Here the C substitution at B site (by BRH doping) is the significant factor for the lattice parameter changes. The ratio $\frac{c}{a}$, a measure of lattice distortion, increases with BRH doping, but remains almost unchanged with Ho_2O_3 doping.

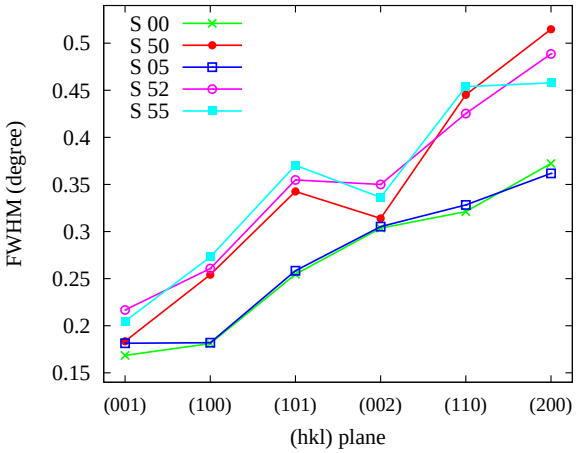

Figure 5.32: FWHM of selected peaks of BRH and nano Ho_2O_3 added samples.

The Full Width at Half Maximum (FWHM) of selected peaks of the samples are shown in figure 5.32. The data shows a clear and systematic trend with doping. The sample added with Ho_2O_3 alone shows same FWHM values as that of the undoped sample, while the sample added with BRH shows considerably different FWHM values. The FWHM of Ho_2O_3 added samples once again confirms that the RE ions are not entered into the lattice sites in MgB_2. The FWHM of the *(00l)* planes has hardly any effect by the doping, either for mono or codoping. But the FWHM of *(hk0)* and *(hkl)* planes are affected by the doping: *(hk0)* is the most affected. The FWHM of *(hk0)* significantly increases with BRH doping, which is due to the C substitution at B sites.

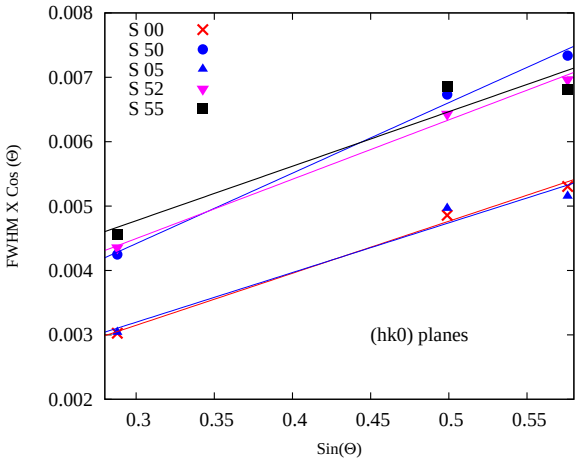

Figure 5.33: Williamson-Hall plots of (hk0) planes of the samples. Points shows data points and lines are linear fits to the data points.

Figure 5.33 shows the Williamson-Hall plots of the *(hk0)* planes of the samples. Using the plots, lattice strain is estimated from the slope and the crystallite size from the *y* intercept. The estimated lattice strain values for *(hk0)* planes for the samples are given in table 5.14. The samples added with BRH have a considerably higher strain value. The sample added with nano Ho_2O_3 alone (S 05) has slightly lower strain value compared to that of the pure sample. For the *(00l)* planes, both BRH and nano Ho_2O_3 addition shows slight reduction in the lattice strain. The particle size (table 5.14) decreases significantly with the addition. The undoped sample has an average particle size of 210 nm, while the samples S 50 and S 05 have particle sizes of 140 nm and 180 nm respectively. For S 52 and S 55 the particle size are still reduced to 90 nm and 60 nm. Thus from the FWHM analysis it is clear that significant in-plane lattice strain occurs by BRH addition. Also both BRH and Ho_2O_3 addition causes considerable decrease of MgB_2 grain size.

The SEI SEM images of the fractured surface of the samples (figure 5.34) show distinct and systematic microstructural change as a result of doping. The undoped sample (S 00) shows randomly oriented faceted hexagonal MgB_2 grains with average size of 1-2 μm. Some of the grains in

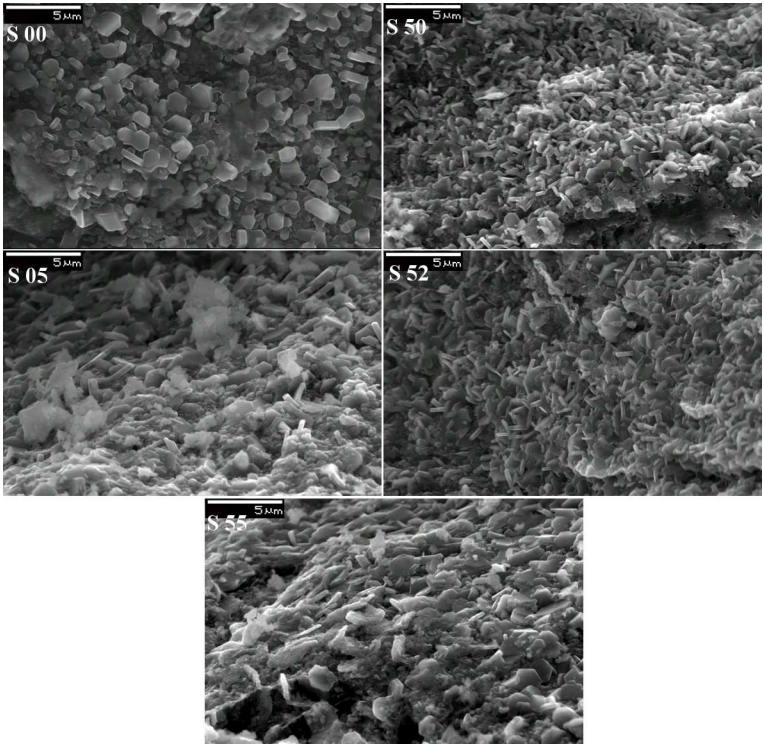

Figure 5.34: SEI SEM of BRH and nano Ho_2O_3 added samples.

the sample showed sharp grain boundaries, while most of the grains show melt like grain boundaries/connections. The BRH added sample (S 50) has uniformly distributed flaky grains with much smaller size than those in S 00. The small size of the grains of S 50 is in agreement with its observed higher FWHM values. Ho_2O_3 added sample (S 05) shows a mictrostructure significantly different from those of the above two samples. Some amorphous like (less crystallized) regions (pockets) are seen in the matrix of this sample. For the codoped samples, the microstructure of S 52 is more like sample S 50, while sample S 55 is more like S 05.

5.5.3 Discussion of the results

The $J_C(H)$ of MgB_2 is improved by the doping of nano Ho_2O_3 and BRH in mono and codoping conditions. The level of enhancement is more in BRH and less in Ho_2O_3 addition for monodoped samples. The codoped samples have significantly enhanced $J_C(H)$ values compared to the undoped and monodoped samples. In the case of bulk MgB_2 superconductor, the in-field critical current density is controlled by parameters like phase purity, crystallinity, grain connectivity, flux pinning etc [84]. From the XRD and SEM results it is very clear that the undoped sample has better phase purity and crystallinity and homogeneity. the undoped sample sample has higher T_C and low ΔT_C values also. So the observed enhancement in flux pinning and the $J_C(H)$ of the added samples cannot be attributed to a better phase purity, crystallinity and/or homogeneity.

Considering the nano Ho_2O_3 alone added sample (S 05), the added Ho_2O_3 reacted with B and formed HoB_4 phase as impurity. The lattice parameters, FWHM as well as T_C and ΔT_C values of the nano Ho_2O_3 added sample remains almost comparable to that of the undoped sample, indicating that Ho is not entered into the lattice site of either Mg or B. In this sample the pinning is mainly provided by the reacted impurity phase HoB_4. The strength of pinning force exerted on the flux lines by these pinners may be weak and hence the observed moderate improvement in flux pinning and moderate increase in $J_C(H)$ in the sample S 05. In other words the main reason for the $J_C(H)$ improvement in Ho_2O_3 added sample is pinning alone. For the BRH added sample there is clear evidence of C substitution at the B site and this is the main reason for the strong enhancement in $J_C(H)$ performance. The reaction induced secondary phases such as Mg_2Si and Mg_2C_3 can contribute to further pinning. For the codoped samples both these effects of BRH and Ho_2O_3 are simultaneously active, i.e., a combination of 'substitution' + 'pinning'. The BRH addition improves H_{C2} and the magnetic HoB_4 particles provide strong pinning to the vortex lines, together with the considerable reduction in the grain size by addition, leads to the strong improvement of $J_C(H)$ in the codoped samples.

5.5.4 Conclusion of the addition study

The superconducting properties of added MgB_2 differ for the two additives. BRH caused considerable amount of C substitution at B site and formed Mg_2Si and Mg_2C_3. Ho_2O_3 decomposed and reacted with B to form HoB_4.

Table 5.15: Influence of different categories of additives on MgB_2.

Additive	Enhancement of $J_C(H)$	Main reason for $J_C(H)$ enhancement
Nano REO	marginal	Pinning by reaction induced impurities (REB_4, MgO etc)
Nano TiC	moderate	Pinning by unreacted nano TiC inclusions
Nano SiC	Significant	Carbon substitution and pinning by reaction induced inclusions (Mg_2Si, SiC)
BRH	**Significant**	Carbon substitution and pinning by reaction induced inclusions (Mg_2Si, Mg_2C_3)

No Ho is substituted at either Mg or B site. Considering the $J_C(H)$ performance, for monodoping, Ho_2O_3 improved the $J_C(H)$ moderately, but BRH improved the $J_C(H)$ strongly. Codoping of Ho_2O_3 with BRH is found to be much more effective for the enhancement of $J_C(H)$ of MgB_2 than the mono doping of any one of these additives. The substitution of C at B site by BRH and the formation of magnetic particles of HoB_4 by Ho_2O_3 are the reasons for the strong improvement of $J_C(H)$ in the added samples.

5.6 Summary of the chemical additions

Summarizing the chapter, the effect of different categories of additives on the in-field in-field critical current density of MgB_2 superconductor is studied and the in-field critical current density is significantly enhanced by selective additives. Table 5.15 summarizes the influence of different categories of dopants on MgB_2.

Figure 5.35 shows a comparison of $J_C(H)$ performance of different addition studies carried out in the present work. The undoped MgB_2 has a very low J_C value of 100-1000 A/cm^2 for fields > 7 T at 5 K. By the selective chemical addition the value of J_C is enhanced to 5×10^3-2×10^4 A/cm^2 for the same fields and temperature. So that the $J_C(H)$ enhanced by nearly 50 times compared to the pure MgB_2. Burned rice husk, a novel additive is introduced into MgB_2, which improved the in-field critical current density of the material strongly and the improvement is at par with most of the best additives/dopants reported so far. Further, codoping studies of different type of materials suitable for substitution/substitution+reaction/reaction are explored and found to be much

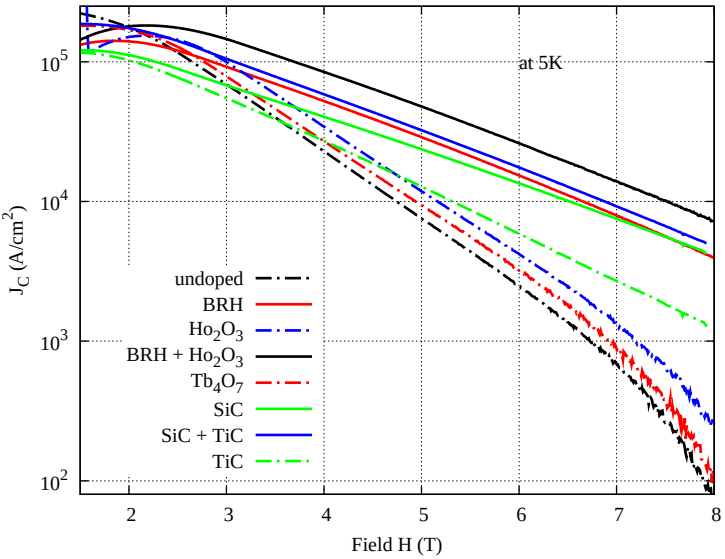

Figure 5.35: Comparison of $J_C(H)$ performance of MgB_2 due to different chemical addition. Except BRH, all other additives are commercially available nano materials. The data shown are for addition of 5 wt.% except for codoping where the addition level were 2.5 wt.% for TiC, SiC, Ho_2O_3 and 5 wt.% for BRH.

more effective than monodoping. At 5 K and 8 T, the sample added with 5 wt.% of BRH and 2.5 wt.% nano Ho_2O_3 has a J_C of 0.8×10^4 A/cm^2, enhanced by 100 times compared to that of the undoped sample. As a conclusion and future direction, it may be fruitful to explore the codoping of more materials with different nature to the MgB_2 system for better $J_C(H)$ performance.

Chapter 6

Summary and conclusions

6.1 Summary of the work

The objectives of the present work were to prepare good quality MgB_2 superconductor in bulk and wire/tape geometries, and to improve its in-field critical current density by suitable chemical additions.

Good quality MgB_2 bulk superconductor was successfully prepared by a simple *in situ* Powder-In-Sealed-Tube (PIST) method. In this method, Mg and B powders were filled in seamless stainless steel tubes and heat treated in atmospheric condition after sealing the ends. The method is simple and cost effective, since no vacuum or inert atmosphere is needed for the preparation. For the preparation of wires and tapes a systematic study on the chemical reactivity of various sheath materials such as Ag, Cu, Fe, Ni, SS and Ta with Mg/B was conducted. Among these Fe is found to be the most suitable material for the sheath. Fe sheathed MgB_2 wires and tapes were prepared by *in situ* Powder-In-Tube (PIT) technique in mono and multi filamentary geometries. Further, a novel electrical self heating method was introduced for the preparation of Fe sheathed MgB_2 wires and tapes.

The prepared MgB_2 in bulk, wire and tape forms were characterized for phase purity, crystalline and microstructural properties and superconducting properties. The measured superconducting properties such as T_C, ΔT_C, J_C and $J_C(H)$ are at par with the best quality samples reported worldwide.

Additives of different types were introduced into the MgB_2 system for improving the in-field critical current density. By selecting suitable combinations of additives a significant enhancement of the critical current density by 1-2 orders of magnitude were achieved for fields > 5 T, at 5 and 15 K.

Thus the objectives of the work have been achieved. Also most of the results and new findings of the research work included in the thesis are published in SCI journals.

6.2 Conclusions

The main conclusions of the present work are :

1. Standardized a simple and inexpensive method, PIST, for the preparation of good quality MgB_2 bulk superconductors. Typical PIST samples have more than 98% of MgB_2 phase with traces of MgO as the only impurity. The method suppresses Mg loss and Mg oxidation and no vacuum or inert atmosphere is needed for the heat treatment. PIST MgB_2 has sharp superconducting transition with T_C around 38.5 K and ΔT_C <1 K. Critical current densities more than 10^5 A/cm^2 at 2 T and 5 K are achieved in typical PIST samples without any additives.

2. Chemical compatibility of commonly used sheath materials such as Ag, Cu, Fe, Ni, SS and Ta with Mg/B at the reaction temperature (600-950 °C) is studied. Among these materials Fe, an inexpensive and easily available material is found to be the most suitable choice for the preparation of *in situ* MgB_2 wires and tapes. Ag, Cu and Ni react with Mg and form impurity phases and reduce the J_C drastically.

3. MgB_2 wires and tapes in mono and multifilamentary geometries were prepared by the PIT method. For multifilamentary conductors Fe is used as the barrier (sheath surrounding MgB_2), Cu is used for thermal stabilization and Ni is used as the outer sheath. Ni is selected as the outer sheath since is more resistant to oxidation and more environmentally stable. High thermal and electrical conductivity preferred the choice of Cu as the stabilizer. The prepared MgB_2 conductors have critical temperature in the range 38-39 K. High transport critical current densities in the range 10^4-10^5 A/cm^2 at 25-30 K and self-field have been achieved in the wires and tapes.

4. It is demonstrated that MgB_2 wires and tapes with good superconducting properties can be prepared by a novel cost effective electrical self-heating method.

5. Different categories of additives were introduced into the MgB_2 for improving its in-field critical current density. The additives include nano rare earth oxides (REO), nano carbides (SiC and TiC) and burned rice husk (BRH).

   - Rare earth oxides react with B to form the respective rare earth boride phase (REB_4) without any lattice substitutions in MgB_2. The enhancement of $J_C(H)$ by REO addition is only marginal, typically 1-2 times.
   - TiC remains unreacted without any lattice substitutions. TiC causes a moderate improvement of 2-5 times in $J_C(H)$ values at high fields.
   - SiC dissociates and the Si reacts with Mg and forms Mg_2Si. The C released from the SiC substitutes at the B site. As a result, SiC causes significant enhancement of $J_C(H)$ values at high fields. BRH, a natural material, also results significant enhancements in $J_C(H)$ values of MgB_2. Compared to the undoped sample, nano SiC and BRH added samples have 10-70 times higher $J_C(H)$ values at higher applied fields.

6. Burned rice husk (BRH), an inexpensive and easy available natural material is found to be effective in enhancing the in-field critical current density of MgB_2 significantly. The enhancement is comparable to most of the best known additives reported. Thus BRH seems to be a good replacement for the costly nano SiC.

7. Combined addition of both substitution and inclusion type materials produce much more $J_C(H)$ enhancement than any one type can produce. Two sets of combined additions were studied : first with nano SiC + nano TiC and second with BRH + nano REO (Ho_2O_3). In both cases samples added with the two additives showed best $J_C(H)$ values compared to samples added with one of the additives. The sample added with 5 wt.% of BRH and 2.5 wt.% of nano Ho_2O_3 have a $J_C(H)$ of 0.8×10^4 A/cm^2, nearly 100 times that of the undoped sample (0.8×10^2 A/cm^2), at 8 T and 5 K.

6.3 Future directions

The present research work reports development of different methods to prepare good quality MgB_2 superconductor in various forms with improved superconducting properties. However, there are many issues to be addressed before taking these products for practical applications. For the wires and tapes, the heat treatment temperature, duration, starting composition, starting packing density and rolling parameters etc are yet to be precisely optimized and a thorough optimization study is essential for maximizing the current carrying capacity of the conductors. The presented transport current characteristics of the wires and tapes were done only on short length samples of length ≤ 11 cm. Whole length transport characteristics in coil form of long conductors are needed for practical applications.

The current transfer problem in multifilamentary conductors has to be minimized and more research work is needed to solve the issue. Another important area that requires considerable applied research is on the thermal stability of the multifilamentary composites. In the present work the prepared multifilamentary conductors have only $\sim 10\%$ of MgB_2 area fraction and $\sim 8\%$ of Cu area. The rest of the composite have materials with low thermal and electrical conductivities. The distribution and size (relative cross sectional area) of MgB_2, Cu, Fe and Ni must be optimized for improving the thermal stability of the composite.

Regarding the $J_C(H)$ improvement, the results presented in the thesis shows significant enhancement by the BRH addition. The raw rice husk contains some organic volatiles, carbon and silica mostly in amorphous form. For the addition purpose this raw rice husk is burned at 300 °C for 1 hour. No chemical or other thermal treatment is done on the raw rice husk in the present study. Heat treatment of the raw rice husk at different temperatures and duration and or chemical treatment of the raw rice husk can be explored for maximizing C and Si and minimizing O_2 and also for finding the optimum levels of C substitution for the best $J_C(H)$ behavior. Regarding the new additives Carbides and Borides may be of worth full for investigation. Exploring new inexpensive natural materials also must be continued. Exploration of selective additives in the codoping condition must be fruitful for further improvement of the $J_C(H)$ of MgB_2 superconductor.

References

[1] H. K. Onnes, *Leiden Commun.* 124 (1911) 1226.

[2] W. Meissner, R. Oschenfeld, *Naturwiss* 21 (1933) 787.

[3] J. R. Schrieffer, M. Tinkham, *Rev. Mod. Phys.* 71 (1999) S313.

[4] A. A. Abrikosov, *Rev. Mod. Phys.* 76 (2004) 975.

[5] E. Altshuler, T. H. Johansen, *Rev. Mod. Phys.* 76 (2004) 4715.

[6] C. P. Poole, H. A. Farach, R. J. Creswick (Eds.), Superconductivity, Academic Press, California (1995).

[7] P. J. Lee (Ed.), Engineering superconductivity, Wiley-Interscience, John Wiley & Sons, Inc. (2001) Vol. 391.

[8] T. H. Geballe, *Science* 293 (2001) 223.

[9] P. Phillips, *Nature* 406 (2000) 687.

[10] R. Hott, R. Kleiner, T. Wolf, G. Zwicknagl, Frontiers in Superconducting Materials, (Editor:A. V. Narlikar) Springer-Verlag Berlin Heidelberg, 2005.

[11] C. Buzea, K. Robbie, *Supercond. Sci. Technol.* 18 (2005) R1.

[12] C. Buzea, T. Yamashita, *Supercond. Sci. Technol.* 14 (2001) R115.

[13] D. Jrome, A. Mazaud, M. Ribault, K. Bechgaard, *J. Phys. Lett.(Paris)* 41 (1980) L95.

[14] G. Saito, H. Yamochi, T. Nakamura, T. Komatsu, M. Nakashima, H. Mori, K. Oshima, *Physica B* 169 (1991) 372.

[15] M. L. Kulič, *cond-mat.arXiv:0508276v1*.

[16] X. Wang, S. R. Ghorbani, G. Peleckis, S. X. Dou, *Adv. Mater.* 21 (2009) 236.

[17] R. Z. An, L. Wei, Y. Jie, Y. Wei, S. X. Li, L. Z. Cai, C. G. Can, D. X. Li, S. L. Ling, Z. Fang, Z. Z. Xian, *Chin. Phys. Lett.* 25 (2008) 2215.

[18] J. G. Bednorz, K. A. Müller, *Z. Phys. B* 64 (1986) 189.

[19] M. K. Wu, J. R. Ashburn, C. J. Torng, P. H. Hor, R. L. Meng, L. Gao, Z. J. Huang, Y. Q. Wang, C. W. Chu, *Phys. Rev. Lett.* 58 (1987) 908.

[20] C. W. Chu, *Proc. Natl. Acad. Sci.(USA)* 84 (1987) 4681.

[21] J. Nagamatsu, N. Nakagawa, T. Muranaka, Y. Zenitani, J. Akimtsu, *Nature* 410 (2000) 63.

[22] M. V. Sadovskii, *cond-mat.arXiv:0812.0302v1*.

[23] H. W. Weijers, U. P. Trociewitz, K. Marken, M. Meinesz, H. Miao, J. Schwartz, *Supercond. Sci. Technol.* 17 (2004) 636.

[24] H. Padamsee, K. W. Shepard, R. Sundelin, *Nucl. Particle. Sci.* 43 (1993) 635.

[25] K. Watanabe, S. Awaji, M. Motokawa, *Physica B* 329-333 (2003) 1487.

[26] M. Motokawa, K. Watanabe, S. Awaji, *Current Applied Physics* 3 (2003) 367.

[27] L. V. Potanina, A. K. Shikov, G. P. Vedernikov, A. E. Vorobieva, V. I. Pantsyrnyi, I. N. Gubkin,

A. G. Sylaev, E. I. Plashkin, E. A. Dergunova, S. V. Soudjev, *Physica C* 386 (2003) 390.

[28] E. Salpietro, *Supercond. Sci. Technol.* 19 (2006) S84.

[29] H. J. Kim, K. C. Seong, J. W. Cho, J. H. Bae, K. D. Sim, K. W. Ryu, B. Y. Seok, S. H. Kim, *Cryogenics* 46 (2006) 367.

[30] A. P. Malozemoff, J. Maguire, B. Gamble, S. Kalsi, *IEEE Trans. Appl. Supercond.* 11 (2002) 778.

[31] D. Larbalestier, A. Gurevich, D. M. Feldmann, A. Polyanskii, *Nature* 414 (2001) 368.

[32] Y. Eltsev, S. Lee, K. Nakao, N. Chikumoto, S. Tajima, N. Koshizuka, M. Murakami, *Phys. Rev. B* 65 (2002) 140501.

[33] M. Eisterer, M. Zehetmayer, H. W. Weber, *Phys. Rev. Lett.* 90 (2003) 247002.

[34] O. F. de Lima, R. A. Ribeiro, M. A. Avila, C. A. Cardoso, A. A. Coelho, *Phys. Rev. Lett.* 86 (2001) 5974.

[35] D. K. Finnemore, J. E. Ostenson, S. L. Bud'ko, G. Lapertot, P. C. Canfield, *Phys. Rev. Lett.* 86 (2001) 2420.

[36] H. Takahashi1, K. Igawa1, K. Arii1, Y. Kamihara, M. Hirano, H. Hosono, *Nature* 453 (2008) 376.

[37] F. Hunte, J. Jaroszynski, A. Gurevich, D. C. Larbalestier, R. Jin, A. S. Sefat, M. A. McGuire, B. C. Sales, D. K. Christen, D. Mandrus, *Nature* 453 (2008) 903.

[38] D. Dochev, A. B. Pavolotsky, V. Belitsky, H. Olofsson, *Journal of Physics: Conference Series* 97 (2008) 012072.

[39] V. Ferrando, P. Orgiani, A. V. Pogrebnyakov, J. Chen, Q. Li, J. M. Redwing, X. X. Xi, J. E. Giencke, C. B. Eom, Q. R. Feng, J. B. Betts, C. H. Mielke, *Appl. Phys. Lett.* 87 (2005) 252509.

[40] P. M. Grant, *Industr. Physicist* 7 (2001) 22.

[41] L. D. Cooley, A. K. Ghosh, R. M. Scanlan, *Supercond. Sci. Technol.* 18 (2005) R35.

[42] M. Tomsic, M. Rindfleish, J. Yue, K. McFadden, J. Phillips, M. D. Sumption, M. Bhatia, S. Bohnenstiehl, E. W. Collings, *Int. J. Appl. Ceram. Technol* 4 (2007) 250.

[43] M. Tomsic, M. Rindfleish, J. Yue, K. McFadden, D. Doll, J. Phillips, M. D. Sumption, M. Bhatia, S. Bohnenstiehl, E. W. Collings, *Physica C* 456 (2007) 203.

[44] V. Braccini, D. Nardelli, R. Penco, G. Grasso, *Physica C* 456 (2007) 209.

[45] H. Li, l. J. Du, M. Qiu, Y. W. Ma, L. Y. liao, *Physica C* 463 (2007) 1338.

[46] M. Razeti, S. Anguis, L. Bertora, D. Damiani, R. Marabotto, M. Modica, D. Nardelli, M. Perrella, M. Tassisto, *IEEE Trans. Appl. Supercond.* 18 (2008) 882.

[47] S. I. Schlachter, W. Goldacker, A. Frank, B. Ringsdorf, H. Orschulko, *Cryogenics* 46 (2006) 210.

[48] M. Majoros, L. Ye, A. M. Campbell, T. A. Coombs, A. V. Velichko, D. M. Astrill, P. Sargent, M. Haslett, M. D. Sumption, M. Husband, *IEEE Trans. Appl. Supercond.* 17 (2007) 1764.

[49] L. Ye, M. Majoros, A. M. Campbell, T. A. Coombs, S. Harrison, P. Sargent, M. Haslett, M. Husband, *IEEE Trans. Appl. Supercond.* 17 (2007) 2826.

[50] A. Brinkman, J. M. Rowell, *Physica C* 456 (2007) 188.

[51] M. E. Jones, R. E. Marsh, *J. Am. Chem. Soc.* 76 (1953) 870.

[52] V. Russell, R. Hirst, F. A. Kanada, A. J. King, *Acta Cryst.* 6 (1953) 870.

[53] L. Y. Markovskii, Y. D. Kondrashev, G. V. Kaputovskaya, *Zhur. Obsch. Khim.* 25 (1955) 433.

[54] S. Brutti, A. Ciccioli, G. Balducci, G. Gigli, P. Manfrinetti, A. Palenzona, *Appl. Phys. Lett.* 80 (2002) 2892.

[55] S. Brutti, M. Colapietro, G. Calducci, L. Barba, P. Manfrinetti, A. Palenzona, *Intermetallics* 10 (2002) 811.

[56] G. Balducci, S. Brutti, A. Ciccioli, G. Gigli, P. Manfrinetti, A. Palenzona, M. F. Butman, L. Kudin, *J. Physics Chem. Solids* 66 (2005) 292.

[57] Z. K. Liu, D. G. Schlom, Q. Li, l. l. li, *Appl. Phys. Lett.* 78 (2002) 3678.

[58] D. Tzeli, A. Mavridis, *J. Phys. Chem. A* 109 (2005) 10663.

[59] L. Ivanovskiĭ, *Physics of the Solid State* 45 (2003) 1829 and references therein.

[60] S. Jin, H. Mavoori, C. Bower, R. B. van Dover, *Nature* 411 (2001) 563.

[61] D. C. Larblestier, L. D. Cooley, M. O. Rikel, A. A. Polyanskii, J. Jiang, S. Patnaik, X. Y. Cai, D. M. Feldmann, A. Gurevich, A. A. Squitieri, M. T. Naus, C. B. Eom, E. E. Hellstrom, R. J. Cava, K. A. Regan, N. Rogado, M. A. Hayward, T. He, J. S. Slusky, P. Khalifah, K. Inumaru, M. Haas, *Nature* 410 (2001) 186.

[62] C. H. Jiang, T. Nakane, H. Kumakura, *Appl. Phys. Lett.* 87 (2005) 252505.

[63] Y. Feng, Y. Zhao, A. K. Pradhan, C. H. Cheng, J. K. F. Yau, L. Zhou, N. Koshizuka, M. Murakami, *J. Appl. Phys.* 92 (2002) 2614.

[64] S. Hata, T. Yoshidome, H. Sosiati, Y. Tomokiyo, N. Kuwano, A. Matsumoto, H. Kitaguchi, H. Kumakura, *Supercond. Sci. Technol.* 19 (2006) 161.

[65] M. Iavarone, G. Karapetrov, A. E. Koshelev, W. K. Kwok, G. W. Crabtree, W. N. Kang, E. M. Choi, H. J. Kim, S. I. Lee, *Supercond. Sci. Technol.* 17 (2004) S106.

[66] H. J. Choi, D. Roundy, H. Sun, M. L. Cohen, S. G. Louie, *Nature* 418 (2002) 758.

[67] D. G. Hinks, H. Claus, J. D. Jorgensen, *Nature* 411 (2001) 457.

[69] S. M. Kazakov, R. Puzniak, K. Rogacki, A. V. Mironov, N. D. Zhigadlo, J. Jun, C. Soltmann, B. Batlogg, J. Karpinski, *Phys. Rev. B* 71 (2005) 024533.

[68] J. S. Slusky, N. Rogado, K. A. Regan, M. A. Hayward, P. Khalifah, T. He, K. Inumaru, S. M. Lourerio, M. K. Haas, H. W. Zandbergen, R. J. Cava, *Nature* 410 (2001) 343.

[70] W. Mickelson, J. Cumings, W. Q. Han, A. Zettl, *Phys. Rev. B* 65 (2002) 052505.

[71] P. C. Canfield, D. K. Finnemore, S. L. Bud'ko, J. E. Ostenson, G. Lapertot, C. E. Cunningham, C. Petrovic, *Phys. Rev. Lett.* 86 (2001) 2423.

[72] M. N. Kunchur, S. I. Lee, W. N. Kang, *Phys. Rev. B* 68 (2003) 064516.

[73] W. Goldacker, S. I. Schlachter, B. Obst, B. Liu, J. Reiner, S. Zimmer, *Supercond. Sci. Technol.* 17 (2004) S363.

[74] S. Soltanian, X. L. Wang, I. Kusevic, E. Babic, A. H. Li, M. J. Qin, J. Horvat, H. K. Liu, E. W. Collings, E. Lee, M. D. Sumption, S. X. Dou, *Physica C* 361 (2001) 84.

[75] M. D. Sumption, M. Bhatia, X. Wu, M. Rindfleisch, M. Tomsic, E. W. Collings, *Supercond. Sci. Technol.* 18 (2005) 730.

[76] Y. Takano, H. Takeya, H. Fujii, H. Kumakura, T. Hatano, K. Togano, H. Kito, H. Ihara, *Appl. Phys. Lett.* 78 (2001) 2914.

[77] S. L. Li, H. H. Wen, Z. W. Zhao, Y. M. Ni, Z. A. Ren, G. C. Che, H. P. Yang, Z. Y. Liu, Z. X. Zhao, *Phys. Rev. B* 64 (2001) 094522.

[78] S. L. Bud'ko, C. Petrovic, G. Lapertot, C. E. Cunningham, P. C. Canfield, M. H. Jung, A. H. Lacerda, *Phys. Rev. B* 63 (2001) 220503.

[79] M. D. Sumption, M. Bhatia, M. Rindfleisch, M. Tomsic, S. Soltanian, S. X. Dou, E. W. Collings, *Appl. Phys. Lett.* 86 (2005) 092507.

[80] K. Vinod, N. Varghese, U. Syamaprasad, *Supercond. Sci. Technol.* 20 (2007) R31.

[81] S. X. Dou, A. V. Pan, M. J. Qin, T. Silver, Frontiers in Superconducting Materials, (Editor:A. V. Narlikar) Springer, 2005.

[82] V. Braccini, A. Gurevich, J. E. Giencke, M. C. Jewell, C. B. Eom, D. C. Larbalestier, A. Pogrebnyakov, Y. Cui, B. T. Liu, Y. F. Hu, J. M. Redwing, Q. Li, X. X. Xi, R. K. Singh, R. Gandikota, J. Kim, B. Wilkens, N. Newman, J. Rowell, B. Moeckly, V. Ferrando, C. Tarantini, D. Marr, M. Putti, C. Ferdeghini, R. Vaglio, E. Haanappel, *Phys. Rev. B* 71 (2005) 012504.

[84] E. W. Collings, M. D. Sumption, M. Bhatia, M. A. Susner, S. D. Bohnenstiehl, *Supercond. Sci. Technol.* 21 (2008) 103001.

[83] J. Jiang, B. J. Senkowicz, D. C. Larbalestier, E. E. Hellstrom, *Supercond. Sci. Technol.* 19 (2006) L33.

[85] M. Eisterer, *Supercond. Sci. Technol.* 20 (2007) R47.

[86] T. Matsushita, M. Kiuchi, A. Yamamoto, J. Shimoyama, K. Kishio, *Supercond. Sci. Technol.* 21 (2008) 015008.

[94] S. K. Chen, A. Serquis, G. Serrano, K. A. Yates, M. G. Blamire, D. Guthrie, J. Cooper, H. Wang, S. Margadonna, J. L. MacManus-Driscoll, *Adv. Funct. Mater.* 18 (2008) 113.

[87] H. Yamada, M. Hirakawa, H. Kumakura, A. Matsumoto, H. Kitaguchi, *Appl. Phys. Lett.* 84 (2004) 1728.

[88] H. Kumakura, H. Kitaguchi, A. Matsumoto, H. Hatakeyama, *Appl. Phys. Lett.* 84 (2004) 18.

[89] S. K. Chen, Z. Lockman, M. Wei, B. A. Glowacki, J. L. MacManus-Driscoll, *Appl. Phys. Lett.* 86 (2007) 242501.

[90] Y. F. Lu, J. S. Li, S. K. Chen, G. Yan, M. H. Pu, C. S. Li, P. I. Zhang, *Physica C* 467 (2007) 38.

[91] B. J. Senkowicz, R. P. Moyet, R. J. Mungall, J. Hedstrom, O. N. C. Uwakwch, E. E. Hellstrom, D. C. Larbalestier, *Supercond. Sci. Technol.* 19 (2006) 1173.

[92] X. Xu, J. H. Kim, W. K. Yeoh, Y. Zhang, S. X. Dou, *Supercond. Sci. Technol.* 19 (2006) L47.

[93] D. G. Hinks, J. D. Jorgensen, H. Zheng, S. Short, *Physica C* 382 (2002) 166.

[95] T. Prikhna, W. Gawalek, Y. Savchuk, V. Moshchil, N. Sergienko, A. B. Surzhenko, M. Wendt, S. Dub, V. Melnikov, C. Schmidt, P. Nagorny, *Physica C* 386 (2003) 565.

[96] T. Prikhna, W. Gawalek, Y. Savchuk, N. Sergienko, V. Moshchil, S. Dub, V. Sverdum, L. Kovalev, V. Penkin, M. Zeisberger, M. Wendt, G. Fuchs, T. Habisreuther, D. Litzkendorf, P. Nagorny, V. Melnikov, *Physica C* 460 (2007) 595.

[97] X. L. Wang, S. Soltanian, M. James, M. J. Qin, J. Horvat, Q. W. Yao, H. K. Liu, S. X. Dou, *Physica C* 408 (2004) 63.

[98] N. A. Frederick, S. Li, M. B. Mapple, V. F. Nesterenko, S. S. Indrakanti, *Physica C* 363 (2001) 1.

[99] A. N. Ling, C. Chen, X. Li, Q. R. Feng, *Front. Phys. China* 1 (2007) 81.

[100] M. Maeda, Y. Zhao, S. X. Dou, Y. Nakayama, T. Kawakami, H. Kobayashi, Y. Kubota, *Supercond. Sci. Technol.* 21 (2008) 032004.

[101] G. Giunchi, G. Ripamonti, T. Cavallin, E. Bassani, *Cryogenics* 46 (2006) 237.

[102] C. E. Cunningham, C. Petrovic, G. Lapertot, S. L. Bud'ko, F. Laabs, W. Straszheim, D. K. Finnemore, P. C. Canfield, *Physica C* 353 (2001) 5.

[103] J. D. DeFouw, D. C. Dunand, *Appl. Phys. Lett.* 83 (2003) 120.

[104] C. B. Eom, M. K. Lee, J. H. Choi, L. J. Belenky, X. Song, L. D. Cooley, M. T. Naus, S. Patnaik, J. Jiang, M. Rikel, A. Polyanskii, A. Gurevich, X. Y. Cai, S. D. Bu, S. E. Babcock, E. E. Hellstrom, D. C. Larbalestier, N. Rogado, K. A. Regan, M. A. Hayward, T. He, J. S. Slusky, K. Inumaru, M. K. Haas, R. J. Cava, *Nature* 411 (2001) 558.

[105] K. Komori, K. Kawagishi, Y. Takano, H. Fujii, S. Arisawa, H. Kumakura, M. Fukutomi, K. Togano, *Appl. Phys. Lett.* 81 (2002) 1047.

[106] H. Abe, K. Nishida, M. Imai, H. Kitazawa, K. Yoshii, *Appl. Phys. Lett.* 85 (2004) 6197.

[107] H. L. Suo, C. Beneduce, M. Dhallé, N. Musolino, J. Y. Genoud, R. Flükiger, *Appl. Phys. Lett.* 79 (2001) 3116.

[108] H. Kumakura, A. Matsumoto, H. Fujii, K. Togano, *Appl. Phys. Lett.* 79 (2001) 2435.

[109] G. Grasso, A. Malagoli, C. Ferdeghini, S. Roncallo, V. Braccini, A. S. Siri, M. R. Cimberle, *Appl. Phys. Lett.* 79 (2001) 230.

[110] A. Serquis, L. Civale, D. L. Hammon, J. Y. Coulter, X. Z. Liao, Y. T. Zhu, D. E. Peterson, F. M. Mueller, *Appl. Phys. Lett.* 82 (2003) 1754.

[111] H. Fang, S. Padmanabhan, Y. X. Zhou, K. Salama, *Appl. Phys. Lett.* 82 (2003) 4113.

[112] H. Fang, P. T. Putman, S. Padmanabhan, Y. X. Zhou, K. Salama, *Supercond. Sci. Technol.* 17 (2004) 717.

[113] B. A. Glowacki, M. Majoros, M. Vickers, J. E. Evetts, Y. Shi, I. Mcdougall, *Supercond. Sci. Technol.* 14 (2001) 193.

[114] A. K. Pradhan, S. B. Roy, P. Chaddah, C. Chen, B. M. Wanklyn, *Phys. Rev. B* 49 (1994) 12984.

[115] C. Meingast, D. C. Larbalestier, *J. Appl. Phys.* 66 (1989) 5971.

[116] C. Meingast, P. J. Lee, D. C. Larbalestier, *J. Appl. Phys.* 66 (1989) 5962.

[117] R. M. Scanlan, W. A. Fietz, E. F. Koch, *J. Appl. Phys.* 46 (1975) 2244.

[118] S. X. Dou, X. L. Wang, Y. C. Guo, Q. Y. Hu, P. Mikheenko, J. Horvat, M. Ionescu, H. K. Liu, *Supercond. Sci. Technol.* 10 (1997) A52.

[119] J. Shimoyama, *Supercond. Sci. Technol.* 13 (2000) 43.

[120] T. Matsushita, *Supercond. Sci. Technol.* 13 (2000) 730.

[121] Y. P. Sun, W. H. Song, B. Zhao, J. J. Du, H. H. Wen, Z. X. Zhao, H. C. Ku, *Appl. Phys. Lett.* 76 (2000) 3795.

[122] E. Martínez, P. Mikheenko, M. Martínez-López, A. Millán, A. Bevan, J. S. Abell, *Phys. Rev. B* 75 (2007) 134515.

[123] H. Kitaguchi, A. Matsumoto, H. Kumakura, T. Doi, H. Yamamoto, K. Saitoh, H. Sosiati, S. Hata, *Appl. Phys. Lett.* 85 (2004) 2842.

[124] X. Y. Song, S. E. Babcock, C. B. Eom, D. C. Larbalestier, R. Ka, R. J. Cava, S. L. Bud'ko, P. C. Canfield, D. K. Finnemore, *Supercond. Sci. Technol.* 15 (2002) 511.

[125] A. Yamamoto, J. Shimoyama, S. Ueda, Y. Kastura, I. Iwayama, S. Horii, K. Kishio, *Appl. Phys. Lett.* 86 (2005) 212505.

[126] S. Li, T. White, K. Laursen, T. T. Tan, C. Q. Sun, Z. L. Dong, Y. Li, S. H. Zho, J. Horvat, S. X. Dou, *Appl. Phys. Lett.* 83 (2005) 314.

[127] Y. Bugoslavsky, L. F. Cohen, G. K. Perkins, M. Polichetti, T. J. Tate, R. Gwilliam, A. D. Caplin, *Nature* 411 (2001) 561.

[128] A. Martinelli, C. Tarantini, E. Lehmann, P. Manfrinetti, A. Palenzona, I. Pallechi, M. Putti, C. Ferdeghini, *Supercond. Sci. Technol.* 21 (2008) 012001.

[129] I. Pallechi, C. Tarantini, H. U. Aebersold, V. Braccini, C. Fanciulli, C. Ferdeghini, F. Gatti, E. Lehmann, P. Manfrinetti, D. Marré, A. Palenzona, A. S. Siri, M. Vignolo, M. Putti, *Phys. Rev. B* 71 (2005) 212507.

[133] K. Vinod, R. G. A. Kumar, U. Syamaprasad, *Supercond. Sci. Technol.* 20 (2007) R1.

[130] S. X. Dou, S. Soltanian, W. K. Yeoh, Y. Zhang, *IEEE Trans. Appl. Supercond.* 15 (2005) 3219.

[131] S. X. Dou, O. Sherbakova, W. K. Yeoh, J. K. Kim, S. Soltanian, X. L. Wang, C. Senatore, R. Flükiger, M. Dhallé, O. Husnjak, E. Babic, *Phys. Rev. Lett.* 98 (2007) 097002.

[132] W. K. Yeoh, S. X. Dou, *Physica C* 456 (2007) 170.

[134] M. Bhatia, M. D. Sumption, E. W. Collings, *IEEE Trans. Appl. Supercond.* 15 (2005) 3204.

[135] Y. Feng, Y. Zhao, A. K. Pradhan, C. H. Cheng, J. K. F. Yau, L. Zhou, N. Koshizuka, M. Murakami, *Appl. Phys. Lett.* 92 (2002) 2614.

[136] Y. Zhao, Y. Feng, C. H. Cheng, L. Zhou, Y. Wu, T. Machi, Y. Fudamoto, N. Koshizuka, M. Murakami, *Appl. Phys. Lett.* 79 (2001) 1154.

[137] T. M. Shen, G. Li, C. H. Cheng, Y. Zhao, *Supercond. Sci. Technol.* 19 (2006) 1190.

[138] S. X. Dou, S. Soltanian, Y. Zhao, E. Getin, Z. Chen, O. Shcherbakova, J. Horvat, *Supercond. Sci. Technol.* 18 (2005) 710.

[140] Y. Ma, X. Zhang, G. Nishijima, K. Watanabe, S. Awaji, X. Bai, *Appl. Phys. Lett.* 88 (2006) 072502.

[139] M. Hermann, W. Haessler, C. Rodig, W. Gruner, B. Holzapfel, L. Schultz, *Appl. Phys. Lett.* 91 (2007) 082507.

[142] S. X. Dou, S. Soltanian, J. Horvat, X. L. Wang, S. H. Zhou, M. Ionescu, H. K. Liu, P. Munroe, M. Tomsic, *Appl. Phys. Lett.* 81 (2002) 3419.

[141] S. X. Dou, A. V. Pan, S. H. Zhou, M. Ionescu, X. L. Wang, J. Horvat, H. K. Liu, P. R. Munroe, *J. Appl. Phys.* 94 (2003) 1850.

[143] S. X. Dou, A. V. Pan, S. H. Zhou, M. Ionescu, H. K. Liu, P. R. Munroe, *Supercond. Sci. Technol.* 15 (2002) 1.

[144] A. Matsumoto, H. Kumakura, H. Kitaguchi, B. J. Senkowicz, M. C. Jewell, E. E. Hellstrom, Y. Zhu, P. M. Voyles, D. C. Larbalestier, *Appl. Phys. Lett.* 89 (2005) 132508.

[145] S. Zhou, A. V. Pan, D. Wexler, S. X. Dou, *Adv. Mater.* 19 (2007) 1373.

[148] S. K. Chen, M. Wei, J. L. MacManus-Driscoll, *Appl. Phys. Lett.* 88 (2006) 192512.

[146] C. Cheng, Y. Zhao, *Appl. Phys. Lett.* 89 (2006) 252501.

[149] X. F. Pan, T. M. Shen, G. Li, C. H. Cheng, Y. Zhao, *Phys. Status Solidi (a)* 204 (2007) 1555.

[147] J. Wang, Y. Bugoslavsky, A. Berenov, L. Cowey, A. D. Caplin, L. F. Cohen, J. L. MacManus-Driscoll, L. D. Cooley, X. Song, D. C. Larbalestier, *Phys. Status Solidi (a)* 81 (2002) 2026.

[150] T. H. Johansen, M. Baziljevich, D. V. Shantsev, P. E. Goa, Y. M. Galperin, W. N. Kang, H. J. Kim, E. M. Choi, M. S. Kim, S. I. Lee, *Europhys. Lett.* 59 (2002) 599.

[151] D. V. Shantsev, A. V. Bobyl, Y. M. Galperin, T. H. Johansen, S. I. Lee, *Phys. Rev. B* 72 (2005) 024541.

[152] I. Felner, V. P. S. Awana, M. Mudgel, H. Kishan, *J. Appl. Phys.* 101 (2007) 09101.

[153] S. K. Chen, K. A. Yates, M. G. Blamire, J. L. MacManus-Driscoll, *Supercond. Sci. Technol.* 18 (2005) 1473.

[154] F. Wu, Y. F. Lu, G. Yan, J. S. Li, Y. Feng, H. P. Tang, S. K. Chen, H. L. Xu, C. S. Li, P. X. Zhang, *Supercond. Sci. Technol.* 19 (2006) 1215.

[155] X. Xu, M. J. Qin, K. Konstantinov, D. I. Santos, W. K. Yeoh, J. H. Kim, S. X. Dou, *Supercond. Sci. Technol.* 19 (2006) 466.

[156] W. Häßler, B. Birajdar, W. Gruner, M. Herrmann, O. Perner, C. Rodig, M. Schubert, B. Holzapfel, O. Eibl, L. Schultz, *Supercond. Sci. Technol.* 19 (2006) 512.

[157] D. Wang, Y. Ma, Z. Yu, Z. Gao, X. Zhang, K. W, E. Mossang, *Supercond. Sci. Technol.* 20 (2007) 574.

[158] J. S. Rhyee, C. A. Kim, B. K. Cho, J. T. Kim, *Appl. Phys. Lett.* 80 (2002) 4407.

[159] Q. Z. Shi, Y. C. Liu, Q. Zhao, Z. Q. Ma, *J. Alloys Compd.* 458 (2008) 553.

[160] S. C. Yan, G. Yan, C. F. Liu, Y. F. Liu, L. Zhou, *J. Alloys Compd.* 437 (2007) 298.

[161] Y. C. Liu, Q. Z. Shi, Q. Zhao, Z. Q. Ma, *J. Mater. Sci: Mater. Electron.* 18 (2007) 855.

[162] C. Cui, D. Liu, Y. Shen, J. Sun, F. Meng, R. Wang, S. Liu, A. L. Greer, S. Chen, B. A. Glowacki, *Acta Mater.* 52 (2004) 5757.

[163] E. Martínez, L. A. Angurel, R. Navarro, *Supercond. Sci. Technol.* 15 (2002) 1043.

[164] S. Zhou, A. V. Pan, M. Ionescu, H. Liu, S. X. Dou, *Supercond. Sci. Technol.* 15 (2002) 236.

[165] W. Häßler, C. Rodig, C. Fischer, B. Holzapfel, O. Perner, J. Eckert, K. Nenkov, G. Fuchs, *Supercond. Sci. Technol.* 16 (2003) 281.

[166] C. R. M. Grovener, L. Goodsir, C. J. Salter, P. Kováč, I. Hušek, *Supercond. Sci. Technol.* 17 (2004) 479.

[167] P. Fabbricatore, M. Greco, R. Musenich, P. Kováč, I. Husek, F. Gomory, *Supercond. Sci. Technol.* 16 (2003) 364.

[168] Y. Feng, G. Yan, Y. Zhao, X. J. Wu, A. K. Pradhan, X. Zhang, C. F. Liu, X. H. Liu, L. Zhou, *Supercond. Sci. Technol.* 16 (2003) 682.

[169] E. Bellingeri, A. Malagoli, M. Modica, V. Braccini, A. S. Siri, G. Grasso, *Supercond. Sci. Technol.* 16 (2003) 276.

[170] A. Stenvall, I. Hiltunen, A. Korpela, J. Lehtonen, R. Mikkonen, J. Viljamaa, G. Grasso, *Supercond. Sci. Technol.* 20 (2007) 386.

[171] H. Kitaguchi, H. Kumakura, *Supercond. Sci. Technol.* 18 (2005) S284.

[172] W. Goldacker, S. I. Schlachter, B. Liu, B. Obst, E. Klimenko, *Physica C* 401 (2003) 80.

[173] R. Musenich, P. Fabbricatore, S. Farinon, C. Ferdeghini, G. Grasso, M. Greco, A. Malagoli, R. Marabotto, M. Modica, D. Nardelli, A. S. Siri, M. Tassisto, A. Tumino, *IEEE Trans. Appl. Supercond.* 15 (2005) 1452.

[174] P. Kováč, I. Hušek, T. Melišek, E. Martínez, M. Dhallé, *Supercond. Sci. Technol.* 19 (2006) 1076.

[175] B. Seeber (Ed.), Handbook of Applied Superconductivity, Vol. 1, Institute of Physics Publishing, Bristol and Philadelphia, (1998).

[176] J. W. Ekin, *J. Appl. Phys.* 49 (1978) 3406.

[177] J. W. Ekin, A. Clark, J. C. Ho, *J. Appl. Phys.* 49 (1978) 3410.

[178] T. Holúbek, P. Kováč, T. Melišek, *Supercond. Sci. Technol.* 18 (2005) 1218.

[179] T. Holúbek, M. Dhallé, P. Kováč, *Supercond. Sci. Technol.* 20 (2007) 123.

[180] A. Stenvall, A. Korpela, J. Lehtonen, R. Mikkonen, *Supercond. Sci. Technol.* 20 (2007) 92.

[181] M. Angst, S. L. Bud'ko, R. H. T. Wilke, P. C. Canfield, *Phys. Rev. B* 71 (2005) 144512.

[182] A. F. Goncharov, V. V. Struzhkin, *Physica C* 385 (2003) 117.

[183] P. Kováč, I. Hušek, J. C. Grivel, W. Pachla, V. Strbík, R. Diduszko, J. Homeyer, N. H. Andersen, *Supercond. Sci. Technol.* 17 (2004) L41.

[184] C. H. Jiang, H. Hatakeyama, H. Kumakura, *Physica C* 423 (2005) 45.

[185] Z. H. Cheng, B. G. Shen, J. Zhang, S. Y. Zhang, T. Y. Zhao, H. W. Zhao, *J. Appl. Phys.* 91 (2002) 7125.

[186] I. G. Markovska, L. A. Lyubchev, *J. Thermal Analysis and Calorimetry.* 89 (2007) 809.

[187] B. B. Nayak, B. Mohanty, S. K. Singh, *J. Am. Ceram. Soc.* 79 (1996) 1197.

[188] P. K. Mishra, B. B. Nayak, B. Mohanty, *J. Am. Ceram. Soc.* 78 (1996) 2381.

[189] Y. Zhao, Y. Feng, T. M. Shen, G. Li, Y. Yang, C. H. Cheng, *J. Appl. Phys.* 100 (2006) 123902.

[190] A. Yamamoto, J. Shimoyama, S. Ueda, S. Horii, K. Kishio, *Physica C* 445-448 (2006) 801.

[191] S. Haigh, P. Kováč, T. A. Prikhna, Y. M. Savchuk, M. R. Kilburn, C. Salter, J. Hutchison, C. Grovenor, *Supercond. Sci. Technol.* 18 (2005) 1190.

[192] Y. Zhao, D. X. Huang, Y. Feng, C. H. Cheng, T. Machi, N. Koshizuka, M. Murakami, *Appl. Phys. Lett.* 80 (2002) 1640.

[193] X. L. Wang, S. H. Zhou, M. J. Qin, P. R. Munroe, S. Soltanian, H. K. Liu, S. X. Dou, *Physica C* 385 (2003) 463.

[194] Y. Ma, X. Zhang, A. Xu, X. Li, L. Xiao, G. Nishijima, S. Awaji, K. Watanabe, Y. Jiao, L. Xiao, X. Bai, K. Wu, H. Wen, *Supercond. Sci. Technol.* 19 (2006) 133.

[195] X. L. Wang, Z. X. Cheng, S. X. Dou, *Appl. Phys. Lett.* 90 (2007) 042501.

[196] A. Yamamoto, J. Shimoyama, I. Iwayama, Y. Katsura, S. Horii, K. Kishio, *Physica C* 463-465 (2007) 807.

[197] R. H. T. Wilke, S. L. Bud'ko, P. C. Canfield, D. K. Finnemore, R. J. Suplinskas, S. T. Hannahs, *Phys. Rev. Lett.* 92 (2004) 217003.

[198] T. Takenobu, T. Ito, D. H. Chi, K. Prassides, Y. Iwasa, *Phys. Rev. B* 64 (2001) 134513.

[199] A. Serquis, Y. T. Zhu, E. J. Peterson, J. Y. Coulter, D. E. Peterson, F. M. Mueller, *Appl. Phys. Lett.* 79 (2001) 4399.

[200] A. Gurevich, *Phys. Rev. B* 67 (2003) 184515.

[201] A. Gurevich, S. Patnaik, V. Braccini, K. H. Kim, C. Mielke, X. Song, L. D. Cooley, S. D. Bu, D. M. Kim, J. H. Choi, L. J. Belenky, J. Giencke, M. K. Lee, W. Tian, X. Q. Pan, A. Siri, E. E. Hellstrom, C. B. Eom, D. C. Larbalestier, *Supercond. Sci. Technol.* 17 (2004) 278.

[202] S. X. Dou, V. Braccini, S. Soltanian, R. Klie, Y. Zhu, S. Li, X. L. Wang, D. Larbalestier, *J. Appl. Phys.* 96 (2004) 7549.

[203] Y. Zhu, A. Matsumoto, B. J. Senkowicz, H. Kumakura, H. Kitaguchi, M. C. Jewell, E. E. Hellstrom, D. C. Larbalestier, P. M. Voyles, *J. Appl. Phys.* 102 (2007) 013913.

[204] X. Zhang, Y. Ma, Z. Gao, D. Wang, S. Awaji, G. Nishijima, K. Watanabe, *IEEE Trans. Appl. Supercond.* 17 (2007) 2915.

[205] K. Vinod, N. Varghese, S. B. Roy, U. Syamaprasad, *Supercond. Sci. Technol.* 22 (2009) 055009.